Signatures of accretion disks around coalescing black hole binaries

Andrea Derdzinski

Submitted in partial fulfillment of the
requirements for the degree
of Doctor of Philosophy
in the Graduate School of Arts and Sciences

COLUMBIA UNIVERSITY

2020

ABSTRACT

Signatures of accretion disks around coalescing black hole binaries

Andrea Derdzinski

This Dissertation is focused on the evolution of massive black hole binaries embedded in gaseous accretion disks. Mergers of massive black holes across a range of mass ratios are powerful sources of gravitational waves (GWs) detectable by the future space-based detector, the Laser Interferometer Space Antenna (LISA). In many cases these sources may reside in Active Galactic Nuclei, in which they are embedded in a dense accretion disk. Interactions with surrounding gas can affect their orbital evolution, leaving signatures in both GWs and in electromagnetic emission.

First, we present two-dimensional hydrodynamical simulations of accretion disks with embedded intermediate mass ratio inspirals. We demonstrate that torques from the gas disk can affect a coalescing BH, producing deviations in the GW signal. Whether or not the gas slows down or speeds up the inspiral, and whether the resultant deviation is detectable, is dependent on the system mass ratio, the disk parameters, and the evolutionary stage of the binary. With a suite of simulations varying these characteristics, we elucidate the sensitivity of the gas imprint and its detectability to mass ratio, disk viscosity, and Mach number. Since the characteristic imprint on the GW signal is strongly dependent on disk parameters, a LISA detection of a gas-embedded inspiral would probe the physics of AGN disks and migration.

Finally, we explore an electromagnetic signature of a circumbinary disk produced in

response to a massive black hole binary merger. With hydrodynamical simulations that resolve the vertical structure of a circumbinary disk, we show that the change in potential produced during the final coalescence of a binary can perturb the surrounding material, producing shocks above the disk midplane, and that this response depends on the disk temperature. This carries implications for the associated emission following the GW signal, which may produce non-thermal radiation that varies with disk properties.

Contents

List of Figures

List of Tables

ACKNOWLEDGMENTS

Graduate school is so much more than the academic experience of research, classes, and teaching. Perhaps because it coincided with transformative years in my early adulthood, these past five years have felt more like a broader experience of personal growth.

A critical aspect of graduate school is defining your unique contribution to a field, but at times it also includes learning the same fundamental concepts many times. Thank you to my advisor, Zoltán Haiman, for giving me the opportunity to work on such interesting projects, as well as your patience and willingness to explain everything from foundational concepts to big ideas. Thank you also to those that agreed to be members of my defense committee: Jules Halpern, Chiara Mingarelli, Brian Metzger, and Lorenzo Sironi. Each of you are role models for your intuition, productivity, and valuable contributions to your fields. Thank you for imparting knowledge and advice throughout the years.

Graduate school is finding a sense of belonging in academia. To this I owe many scientists that have been inspiring friends. Thank you to Sarah Pearson, for the walks, talks, and vulnerability, and for making our apartment a Home. Thank you to Drummond Fielding, for the reminders that astrophysicists can still want to memorize the names of trees, to Andrew Emerick, for giving me my first belay, to Dan D'Orazio, for the consolation that even hard-working academics can be found at summer bluegrass festivals. Thank you all for proving that being successful scientists does not exclude us from also being artists, carpenters, mountaineers, musicians, and day dreamers. Thank you Emily Sandford, Trey Jensen, Nicole Melso, Matt Wilde, Adrian Price-Whelan, Jillian Bellovary, Jeff Andrews, Maria Charisi, Alex Teachey, Adrian Lucy, Jose Manuel Zorrilla Matilla, Steven Mohammed, and so many others, for showing your humanity in a field that can be all too removed from it. All of you make me feel like I belong in this community.

These city years would not be complete without the multitude of connections outside of academia that provided nourishment and perspective, as well as a grounding reminder to not think "too much" about black holes. Thank you Tyler Young, for your compassion, support, and genuine positivity. It is impossible to summarize your impact in a single sentence. Thank you to Andrea Parlapiano, for your healing and unconditional friendship. To Diana Glattly, for bringing warmth and creativity to our Home. To my therapist, for helping me realize when moments of struggle were in fact due to my own innate ambition.

A part of graduate school is searching for distractions to clear your mind and discovering new challenges. Much of my sanity I owe to rock climbing, motorcycles, and powerlifting; in each of these hobbies I found not only an outlet but a supportive community of talented and inspiring individuals, that transformed a vast city into a Neighborhood. I am thankful also for my local bars, for creating sanctuaries where in a city of several million people, everybody knows your name, and everything NYC has to offer, from local businesses to historical landmarks—much of this work was written while drinking Variety coffee and staring at NY Public Library ceilings.

I owe a great deal to my family. Thank you to my parents, Anna and Kris, for a supportive childhood that fostered my interest in solving puzzles, and for providing me with the invaluable opportunity to go to college and pursue puzzle-solving as a career. To my brother, Mark Derdzinski, for when I thought physics might not be "for me," convincing me that it does in fact get more interesting at the advanced level. To my sister, Magdalena Halford, for always reminding me to notice the magic around us and within ourselves, and to John and their family, for always opening the door to a warm home and sanctuary to visit.

Graduate school is the long and slow discovery of realizing you know more than you think you do. Thank you to my undergraduate mentor, Enrico Ramirez-Ruiz, who treated me with the respect of a valued researcher when I felt I knew nothing, and to Jill Naiman,

for your mentorship and countless reminders that I am capable.

This Dissertation is the accumulation of work that involved many people. In each of you I have found inspiration and the ability to define a place for myself in this field. To each of you I owe a part of my success.

2019, New York City

Chapter 1

Introduction

1.1 Motivation

It is widely accepted that supermassive black holes (MBHs) in the mass range $10^5 - 10^{10} M_\odot$ permeate most of the visible universe, residing in the centers of most massive galaxies (Kormendy & Ho 2013). To grow to such extreme sizes, we expect that MBHs begin as 'seeds' in the early universe that subsequently grow by merger and gas accretion events (Inayoshi et al. 2019). The correlation between masses of MBHs and properties of their host galaxies suggests that MBH evolution is intimately tied with environmental interaction, and hence related to the processes governing galaxy evolution (Ferrarese & Ford 2005). Thus to understand the evolution of galaxies, it is important that we understand how their central components evolve (Hopkins et al. 2008; Fabian 2012).

Due to their high masses and sheer compactness, MBHs are remarkable sources of gravitational potential energy. When accreting gas, they become laboratories of astrophysical processes that ultimately produce some of the brightest emission in the Universe (Lynden-Bell 1978). Understanding their evolution not only provides us with a more complete picture

of the evolution of cosmic structures but allows us to probe astrophysical phenomena in their most brilliant regime.

As humans confined to this planet, we interpret the Universe through its messengers. Historically our primary tool for studying the sky has been electromagnetic radiation, as well as, more recently, neutrinos and cosmic rays. With observations across the entire electromagnetic spectrum we have made remarkable progress in building our understanding of MBH evolution, but much remains to be discovered.

This Dissertation began at the onset of a critical discovery−in 2015, we successfully detected a new Cosmic messenger, that of gravitational interaction. The Gravitational Wave (GW) era started with the detection of perturbations in spacetime produced from merging stellar-mass black holes using ground based interferometers (Abbott et al. 2016). Currently, detectors on Earth are measuring high-frequency ($10 - 10^4$ Hz) GWs from merging compact binaries in the nearby universe. Detection of nanohertz GWs is on the horizon with Pulsar timing methods (Burke-Spolaor et al. 2019), and future experiments are in planning stages to probe the intermediate frequency ranges. One of such experiments, the Laser Interferometer Space Antenna (LISA), will pave the way into the milliHertz GW sky (Amaro-Seoane et al. 2017). LISA will detect some of the loudest sources of gravitational waves from interacting MBHs, unveiling intricacies of MBH evolution through all stages of galaxy evolution. What LISA will detect, and how the astrophysical environments of these sources may either aide, hinder, or compliment these detections, is the primary motivation of this Dissertation.

1.2 Evidence for MBHs

MBHs were first proposed with the discovery of the first quasar, an ultra-luminous point-like source inferred to be several billion lightyears away (Schmidt 1963). Since then we have

come to accept that quasars are the most powerful subset of Active Galactic Nuclei (AGN), a term used to describe the central region of a galaxy when it is comparatively bright.

It is widely believed that AGN are powered by accretion of gas onto an MBH, as this explains several properties, including their extraordinary luminosities emitted from regions of presumably small size (inferred from the sources being "point-like," but also given rapid variability on the timescales of hours or weeks, e.g. Salpeter 1964; Rees 1984). There are many types of AGN classified observationally, but the most widely accepted theory for this diversity postulates that AGN are all essentially the same type of source, but observed at different viewing angles (see recent review by Giustini & Proga 2019).

In the nearby universe, we can infer the existence of MBHs via dynamics in galactic nuclei. The closest galactic nucleus we can study is that in our own galaxy, the Milky Way, where we have observations at multiple wavelengths with exquisite angular resolution (Ghez et al. 1998). Specifically, the orbital dynamics of stars in the central parsec of the nucleus provide a convincing case for a four-million solar mass compact object (Genzel et al. 2010). This region of the galaxy is also coincident with a radio source with near-IR and X-ray flares, which can be described as a variable accretion flow onto an MBH, although the luminosity is considerably weaker than is produced by the higher accretion rates which characterize quasars.

The current consensus is that nearby, quiescent MBHs are the descendants of quasars observed in the early universe (Lynden-Bell 1969; Soltan 1982; Yu & Tremaine 2002). This has led to the understanding that MBHs reside in the nuclei of at least several massive galaxies, that throughout their evolution experience periods of activity when gas is fed to the nucleus, and in the nearby universe they are usually in a quiescent, non-AGN state (Kormendy & Richstone 1995).

The most striking evidence to date of an active MBH comes from Very Long Baseline

Interferometry (VLBI) imaging of our neighboring galaxy M87, which successfully produced the first 'image' of an MBH in 2019 (Event Horizon Telescope Collaboration et al. 2019). This international endeavor, known as the Event Horizon Telescope, consisted of 8 radio observatories all over the globe forming a single interferometer to observe a single target, and was able to measure directly, for the first time, the event horizon of an MBH by imaging the lensing of radiation from hot gas in its vicinity.

1.3 MBHs encounter other MBHs

Models of hierarchical structure formation suggest that massive galaxies form by mergers of less massive progenitors (Volonteri et al. 2003; Mo et al. 2010). Given that nearly all galaxies undergo at least one major merger in their assembly, we expect most galaxies to host multiple MBHs at some point in their evolution (Sesana et al. 2017). If MBHs are truly ubiquitous, then the existence of MBH binaries or multiple MBH systems should not only be common, but play a critical role in galaxy evolution.

The existence of MBH binaries (MBHBs) was postulated several decades ago. Following a major galaxy merger, it is expected that the MBHs in the post-merger galaxy will migrate towards the nucleus eventually forming a bound binary (Begelman et al. 1980). Theoretical modeling supports the idea that MBHs travel from kilo-parsec to parsec scales via processes including dynamical friction, evolution in a triaxial potential, three-body interactions with stars and−in the case of gas-rich mergers−torques from accretion disks (Mayer 2013). Once they become bound into a binary, interactions with their environment and other MBHs from subsequent mergers can eventually drive the binary together until it is close enough for GW emission to take over (Bonetti et al. 2018; Ryu et al. 2018). However, many of the physical processes at work during this stage are uncertain. Between numerical and semi-numerical

studies, predictions of merger times vary from ∼Gyrs to greater than a Hubble time. Many open questions regarding MBHB evolution lie in uncertainties in the timescales of various stages and how they evolve with redshift (Mayer 2017).

Depending on how quickly MBHBs coalesce, we should in principle be able to observe such systems at various stages of orbital evolution. Several pairs of MBHs at kpc separations have been spatially resolved with direct imaging (e.g. Komossa 2003; Fu et al. 2015), and the closest system resolved with radio interferometers exists at a separation of 7.3 pc (Rodriguez et al. 2006). Constraining the population of even more compact (sub-parsec) MBHBs is challenging because such binaries are unresolvable with current telescopes. Even with Very Long Baseline Interferometry, such as that used to image the MBH in M87, we can only spatially resolve binaries in the nearby universe (D'Orazio & Loeb 2018a). Evidence for tight binaries is therefore only indirect, via long-term photometric or spectroscopic monitoring.

Theoretical modeling suggests that modulated EM emission could be produced around a binary in a variety of ways. Hydrodynamical simulations show that a binary embedded in a disk will carve a quasi-circular central cavity, and streams flowing into this cavity will modulate the accretion rate onto each of the BHs (Hayasaki et al. 2007; MacFadyen & Milosavljević 2008; D'Orazio et al. 2013; Farris et al. 2014; Tang et al. 2018). Moreover, emission from an accreting BH companion can be Doppler boosted as the BH travels at near relativistic speeds around a more massive primary MBH (D'Orazio et al. 2015). Assuming the accretion rate variability onto each BH is translated to electromagnetic emission, sub-parsec binaries could exhibit periodic emission with periods of months to years, and should be present in current time-domain surveys (Haiman et al. 2009; Kelley et al. 2019). Such ideas have lead to a number of systematic searches for periodic quasar emission in large surveys, resulting in several dozen binary candidates (Graham et al. 2015; Charisi et al. 2016, 2018; Liu et al. 2019; Hu et al. 2019).

MBHBs may also be identified spectroscopically, by measuring radial velocity drifts in broad emission lines that trace the binary motion. Such searches have identified several dozen candidates and, similar to the photometric surveys, detection of MBHBs is limited due to the inadequate temporal baseline of the observations. Additionally, in both cases intrinsic variability of the source can complicate or mimic binary signatures.

Galactic mergers offer a convenient mechanism for re-fueling the centers of galaxies with gas, feeding quasar activity (e.g. Hernquist 1989). This is observed in numerical simulations of galaxy mergers, during which gas clouds in the pre-merger galaxies sink to the newly formed galactic nucleus (Barnes & Hernquist 1992; Mayer et al. 2007). In this sense, we should expect the formation of MBH binaries and the refueling of AGN to both take part in the same merger event. To fully understand the impact of a MBH on its host galaxy, we must understand the evolution of multiple MBH systems. Via critical interactions with stars and gas, the environment plays a critical role in determining the binary's fate, and details of this interaction may result in consequences for the host galaxy (Kazantzidis et al. 2005), such as enhanced AGN activity (Liu et al. 2012) or starbursts (Taniguchi & Wada 1996).

This Dissertation is centered upon the intersection of two concepts: (i) MBHs throughout their evolution experience periods of accretion, during which gas flows into the MBH in a configuration that is poorly understood; and (ii) at the same time MBHs inevitably interact with other BHs (massive or not). The overlap in these processes presents a tantalizing opportunity: perhaps observations of one aspect can inform the other. As we discuss, environmental effects can have consequences for the detectable signatures of MBHs, and we will soon have the opportunity to probe these interactions *directly* via GWs.

1.4 MBH binaries as Gravitational Wave emitters

First we define a few characteristics of gravitational waves, before introducing characteristics of GW radiation in the context of MBH binaries.

The properties of gravitational radiation can be derived from a multipolar expansion of the mass energy distribution. This is analogous to electromagnetism, in which EM radiation arises from the time variation in the dipole moment of the charge distribution. In the case of gravitational field, however, the dipole moment corresponds to the center of mass of the system, which − due to momentum conservation − does not change. For this reason, gravitational radiation is to leading order generated by a time-varying quadrupole moment, with correction terms that can arise from subsequent higher order moments.

This result is telling of which systems we can expect to generate GWs. In monopolar systems of perfect spherical symmetry, no gravitational radiation is emitted. Similarly, a system that is rotating with perfect axisymmetry will also not produce gravitational radiation. The best cases for GW emission arise from sources that experience substantial acceleration in their quadrupole moments: these can arise from, for example, asymmetric stellar explosions, non-axisymmetric rotating stars, or binaries. Binary systems in particular have relatively large accelerating quadrupole moments, making them promising sources of detectable GWs.

For most purposes in this work, we consider gravitational radiation produced during the inspiral[1] stage of binaries that are quasi-circular[2] and non-spinning. In the inspiral regime, the binary is sufficiently separated such that each constituent can be considered as a point mass. In such cases we can describe the gravitational radiation with the leading quadrupole

[1]The wave description becomes more complicated when the separation between the masses becomes sufficiently small, i.e. at the point of "merging."

[2]Meaning zero eccentricity, except for the adiabatic decrease in separation. Eccentricity can certainly be important for MBHBs−it can significantly affect the binary evolution and corresponding waveform, adding multiple frequency harmonics−but we neglect it here and leave it to future work.

term (Peters 1964). GWs track the large-scale motion of the binary, which is dominated by its orbital motion. The fundamental GW frequency for a binary on a circular orbit is twice the orbital frequency,

$$f_{\rm GW} = \frac{1}{\pi}\left(\frac{GM}{r^3}\right)^{1/2} \tag{1.1}$$

where G is the gravitational constant, M is the total binary mass and r is the semi-major axis.

A useful quantity in describing the evolution of a binary is its chirp mass, defined as

$$M_c \equiv \frac{(M_1 M_2)^{3/5}}{(M_1 + M_2)^{1/5}} \tag{1.2}$$

where $M_1 \geq M_2$ are the primary and secondary masses, respectively. To lowest order, the evolution of a binary due to GW emission is determined uniquely by the chirp mass:

$$\dot{f} = \frac{96}{5}\pi^{8/3}\left(\frac{GM_c}{c^3}\right)^{5/3} f_{\rm GW}^{11/3} \tag{1.3}$$

For this reason, in GW analysis, it is easier to measure the chirp mass (from measurements of f and $\dot{f}$) rather than each constituent mass separately (Cutler & Flanagan 1994). This function also shows that the inspiral is a strong function of frequency: the inspiral rate is very slow at large separations, but increases rapidly at higher frequencies. The resultant signal is often referred to as a 'chirp' as both the amplitude (see below) and frequency increase to higher values.

A GW is formally defined as a perturbation in the spacetime metric that consists of two polarization states, $h_+(t)$ and $h_\times(t)$. A detector measures the linear combination of the two polarizations, referred to as the strain amplitude $h(t)$, that depends on the inclination of the orbit relative to the line of sight and on the orientation of the detector(s). Often when

estimating the detectability of hypothetical sources one can use the sky- and polarization-averaged strain. Conveniently expressed in the Fourier domain, $\tilde{h}_+(f)$ and $\tilde{h}_\times(f)$ are functions that depend on the source distance, orientation, phase evolution, and chirp mass. For reference we provide the averaged strain amplitude of a binary at a co-moving distance $r(z)$ at redshift z as

$$h = \frac{8\pi^{2/3}}{10^{1/2}} \frac{G^{5/3} M_c^{5/3}}{c^4 r(z)} f_r^{2/3}, \tag{1.4}$$

where $f_r \equiv f_{\rm GW}(1+z)$ is the GW frequency in the binary rest frame (see, e.g. Colpi & Sesana 2017). Note that if GWs are produced at cosmological distances, the observed frequency and chirp mass will be redshifted with respect to the source frame as $f_{\rm obs} = f_r/(1+z)$ and $\mathcal{M}_c = M_c(1+z)$, respectively. With the quadrupole approximation alone, a generic binary waveform is invariant under the change to $f_{\rm obs}$ and $\mathcal{M}_c$, and thus does not carry any information on the source redshift. The possibility exists to measure the distance to the source, making GWs a cosmological 'standard sirens,' but to do so one must break the degeneracy between these parameters by including post-Newtonian corrections to the waveform.

Considering that we can only 'observe' a GW source for a finite duration, a useful quantity for characterizing an observable signal is the *characteristic* strain $h_c = h\sqrt{n}$, where n is the characteristic number of cycles the source spends in the relevant frequency band, estimated by $n \simeq f^2/\dot{f}$ (see, e.g. Sesana et al. 2005). h_c is a dimensionless factor that takes into account the effect of integrating a signal over many orbits, the number of which depends on the observation time τ. For sources that emit at continuous frequencies during a total observation, the total number of cycles emitted is simply $n = f\tau$, and h_c accumulates to higher values for observations of either longer duration or higher frequency sources. This corresponds to, for example, the earlier stages of MBHBs that are far enough from each other such that the GW inspiral does not accelerate significantly during an observation. As the

binary evolves, however, the emitted power will chirp to higher frequencies during the observation, spanning less orbits at each particular frequency ($n < f\tau$). When compared to an equivalently dimensionless sensitivity curve, h_c becomes a useful estimator for detectability, as we will further discuss in Chapters 2 and 3.

The maximum GW frequency a binary can emit is reached at its closest separation. For a BH, this occurs close to the radius of the innermost stable circular orbit (ISCO), which in the approximation of a point mass orbiting a non-spinning BH is given by

$$r_{\rm ISCO} = 3r_{\rm S} = 6\frac{GM}{c^2} \tag{1.5}$$

where we have defined the Schwarzschild radius $r_{\rm S}$. Equation 1.5 makes apparent that more massive BHs have a larger characteristic size due to the scaling of $r_{\rm ISCO}$ with M. Thus more massive BH binaries merge as intrinsically low-frequency sources compared to stellar-mass BH binaries. Additionally, we see from Eq. 1.3 and Eq. 1.4 that binaries with more extreme mass ratios coalesce more slowly (emitting weaker GWs relative to an equal mass ratio binary of the same total mass) thereby executing more orbits at each frequency. This has consequences for how sources evolve in different frequency bands.

The frequencies at which we can probe close MBH systems will range from the nanoHertz to the milliHertz regime, depending on the binary mass and separation. In the following sections we describe two experiments that are currently underway or in the planning stages that aim to detect such low-frequency GWs.

1.4.1 Pulsar Timing and the nanohertz GW sky

The method of pulsar timing consists of monitoring an array of millisecond pulsars[3] in our own Galaxy to observe correlated shifts in the arrival time of pulses due to the passage of GWs through the region of space between Earth and the pulsars. Due to the remarkable timing precision of these pulsars, this essentially creates a Galactic scale interferometer (Hellings & Downs 1983; Mingarelli 2019; Burke-Spolaor et al. 2019). Accumulated observations over periods of years to decades allow PTAs to probe GWs in the nanoHertz frequency regime. The dominant contribution at these frequencies is expected to arise from MBH binaries at sub-parsec separations.

GWs have not yet been observed by PTAs, but recent results reported by various PTA collaborations already place significant constraints on the evolution of MBHBs (Shannon et al. 2015; Hazboun et al. 2019), ruling out some of the simplest evolutionary models in which the binaries only inspiral due to GW emission. These results suggest that, given the number of MBHBs expected to exist based on structure formation models, these systems tend to either stall at larger separations, never entering the nanohertz GW regime, or they are more efficiently accelerated down to sub-parsec separations by some mechanism(s), therefore spending less time within the particular frequency range. Such mechanisms can involve interactions with gas and/or stars that steal angular momentum from the binary or drive eccentricity (Kocsis & Sesana 2011; Kelley et al. 2017), or evolution in sufficiently triaxial potentials (Vasiliev et al. 2015). Current limits on the background suggest that environmental interaction plays a role in the evolution of MBH binaries.

These experiments have been taking data for the last several years, by several collaborations around the globe (i.e. Parkes PTA, Shannon et al. 2015; NANOGrav, Arzoumanian

[3]Pulsars are rapidly spinning neutron stars which emit beamed radio emission in a regular, predictable, pattern.

et al. 2018; and European PTA, Babak et al. 2016). Together, the various collaborations form the International Pulsar Timing Array (IPTA, Verbiest et al. 2016). The IPTA is likely to detect the background from the ensemble of massive MBH binaries within the next decade (Shannon et al. 2015; Taylor et al. 2016), and the precise shape of the spectrum will be rich with information about the MBHB population and the extent of environmental interaction.

In addition to the detection of a stochastic background, PTAs should also detect individual sources from nearby massive MBHBs within the next $10-20$ years (Rosado et al. 2015; Mingarelli et al. 2017; Kelley et al. 2018). These will arise as continuous frequency sources in the PTA band at periods of months to years.

1.4.2 MilliHertz GWs with the Laser Interferometer Space Antenna (LISA)

A future experiment, and the primary motivation of this Dissertation , is the Laser Interferometer Space Antenna, a space-based GW detector. This is a joint ESA/NASA mission with plans to launch by 2034.[4]

LISA will be sensitive to the milliHertz frequency range $10^{-4} \lesssim \mathrm{Hz} \lesssim 10^{-1}$. In this window lie close binary systems at a range of scales. The nearest sources include compact binaries of both white dwarfs (Nelemans et al. 2001) and neutron stars (Lau et al. 2019) in our own galaxy. One of the primary targets of LISA sources is coalescing MBH binaries with component masses ($M_{\rm BH} \sim 10^4 - 10^7 M_\odot$), a range not detectable by PTAs or LIGO. These will arguably be the loudest sources in the milliHertz band, and with LISA's sensitivity they can be detectable up to $z \sim 20$. The technology required to support such a mission (i.e. the ability to control noise and fly a test mass on a geodesic) was tested with the LISA

[4] www.lisamission.org

Pathfinder mission in 2016 (Armano et al. 2017), during which it exceeded expectations.[5] With such sensitivity, LISA will hear MBHs mergers in the early universe, probing MBH seed formation and subsequent growth.

In addition to MBHB mergers, LISA will be sensitive enough to detect the coalescence of smaller BHs into MBHs. These events are termed Extreme and Intermediate mass ratio inspirals (E/IMRIs). In principle EMRIs can occur at a range of mass ratios, but the ones of interest to LISA include primary MBHs with masses $10^6 - 10^7 M_\odot$ and secondary BHs with mass ratios $10^{-3} - 10^{-6}$ (Yunes 2009). Such events can occur as stellar-mass BHs[6] residing in galactic nuclei coalesce into the central MBH, often via three-body interactions that result in high eccentricity. Current rates of EMRIs are predicted to be at least a few per year, although estimates vary by a few orders of magnitude depending on uncertainties in populations and dynamics in galactic nuclei (Babak et al. 2017; Amaro-Seoane 2018).

Rates for intermediate mass ratio mergers are even less certain as they rely on the involvement of intermediate-mass BHs (IMBHs), in the mass range $10^2 - 10^5 M_\odot$, the existence of which is suggested, but not strictly proven (Greene et al. 2019). Models of stellar dynamical processes in galactic nuclei predict event rates of a few to tens of mergers per year (Amaro-Seoane et al. 2007; Miller 2009). However, there are reasons for this event rate to be higher based on recent work that suggests the ability of an accretion disk to promote the formation of IMBHs (see Section 1.5). In principle, stellar-mass BHs can also merge with IMBHs, and these also comprise IMRIs detectable by LISA. In the present work we only consider the "massive" IMRIs whose primary component is an MBH.

For reference, we show the LISA sensitivity curve and the characteristic strain of a few example sources in Figure 1.1, adopted from Amaro-Seoane et al. (2017). The characteristic

[5] LISA can achieve 10^{-20} strain resolution by measuring displacements of the order of a picometer (Slutsky & LISA Pathfinder Collaboration 2018).

[6] also compact objects, such as neutron stars

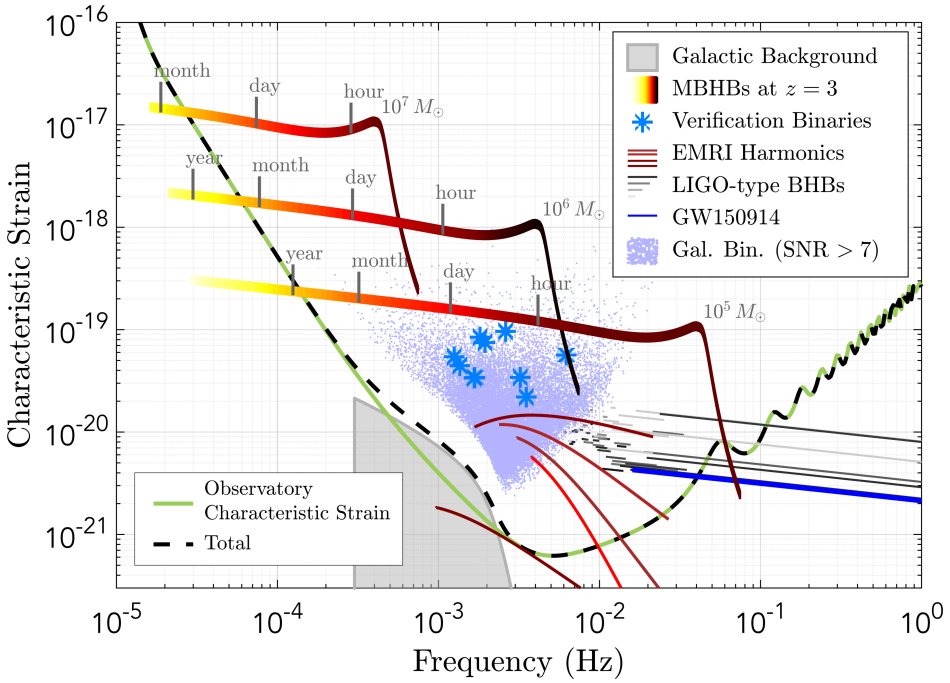

Figure 1.1: The LISA sensitivity curve versus GW frequency (in green) plotted with the characteristic strain of possible sources. Figure adapted from the LISA mission proposal, Amaro-Seoane et al. (2017). Of particular interest is the evolutionary track of MBHB mergers (thick yellow to red lines), which are expected to be significantly loud sources. EMRIs (thin red lines), when eccentric, will emit GWs at multiple harmonic frequencies.

strain is plotted over a corresponding dimensionless sensitivity curve. With this convention the area between the strain and sensitivity is proportional to the total signal to noise ratio, highlighting that coalescing MBHBs will be particularly loud sources.[7] Depending on their mass (and mass ratio) they can exist in the LISA band for weeks to years.

[7]Note that the sky-averaged strain can sometimes be misleading as there is often significant variation in the sensitivity with sky location (Robson et al. 2019).

1.5 Gas around LISA sources

A large fraction of MBH mergers, particularly those expected to be LISA targets, are expected to occur in gas rich environments (Mayer 2013).

In the dense accretion disks expected in AGN, gas can influence the properties of a binary system prior to merger in a variety of ways. It allows for accretion of mass, momentum, and angular momentum, and can exert gravitational torques (often referred to as migration torques in the protoplanetary disk field) that will accelerate or hinder the binary inspiral.

Gas also provides an independent formation pathway for GW sources: star formation in AGN disks can produce embedded compact remnants (Levin 2007) that subsequently accrete, merge, and migrate (Bellovary et al. 2016) before coalescing into the central MBH. Most EMRI rate estimates focus on the events expected to occur in dry nuclei, which would result from highly eccentric encounters between stars in the nucleus. An additional population of gas-embedded E/IMRIs must also be considered, however, and initial estimates of the rates of this subset are around $10^{-4}\,\mathrm{yr}^{-1}$ per AGN, in which case accretion of compact objects in the disk would account for a substantial fraction of the growth of MBHs (Dittmann & Miller 2019).

Gas plays a critical role in MBHB evolution and on the population of MBHBs, and its influence on a MBH system at various stages can have important consequences for what LISA will detect. To understand how such interactions take place, we must turn to accretion disk physics.

1.5.1 Accretion power

Here we briefly review key concepts related to gaseous accretion which we refer to throughout the remainder of this Dissertation.

In addition to their large masses, the sheer compactness of MBHs makes them sources of gravitational potential energy. When gas is present falling towards an MBH, it is precisely the conversion of this gravitational energy into heat (via some "anomalous viscosity"[8]) that makes MBHs the central engines of luminous quasars (Lynden-Bell 1978). Despite several decades of observing AGN[9] and considerable effort to interpret observations from a theoretical standpoint, there are still several uncertainties regarding the accretion process. This is not surprising given that it involves complex fluid dynamics and magnetohydrodynamics, radiative processes, and relativistic processes, which are challenging to model simultaneously.

Gas inflowing into a galactic nucleus can cool radiatively, settling into a geometrically-thin disk (Dotti et al. 2007). This gas needs to lose angular momentum in order to be accreted onto the MBH. Such a process is usually attributed to viscous forces. Several models have been developed which make different assumptions about the configuration of the disk and the mechanism of angular momentum transport. We review the most commonly used disk model below, as it informs some of the initial conditions used in our numerical modeling.

The seminal model of accretion via a geometrically thin, viscous disk was outlined by Shakura & Sunyaev (1973). Irrespective of the physical cause of viscosity, the authors parameterized the effective viscous torque with a dimensionless parameter $\alpha < 1$. The "α-disk" model proposes that the kinematic viscosity is given by the quantity

$$\nu = \alpha c_s h \tag{1.6}$$

where c_s is the sound speed, h is the disk vertical scale-height. If one imagines that viscosity arises from turbulence, at maximum the size of turbulent eddies cannot be greater than h,

[8]Rather than (or in addition to) a microscopic viscosity, accretion requires a stronger viscosity to describe the inflow rates observed in accreting systems, which is likely mediated by some form of turbulence.

[9]as well as accreting binary systems in the Milky Way, which can also be used to constrain accretion disk models.

and their velocity would be limited by c_s (if turbulence was super-sonic, it would rapidly dissipate its energy into shocks). Typical models of disks utilize $\alpha \sim 0.01 - 0.1$, but this depends on the physical regime of interest (King et al. 2007).

This model does not describe a mechanism that generates viscosity, which could be attributed to magnetic forces such as the magneto-rotational instability (Balbus & Hawley 1991) or gravitational instabilities (Lin & Pringle 1987). There are several related thin-disk models in the literature that improve on the standard α-disk model, incorporating corrections due to general relativity (Novikov & Thorne 1973) or disk winds (Slone & Netzer 2012), to name a couple.

The Shakura-Sunyaev model has been utilized widely in the literature for interpreting accreting systems in which the gas is able to radiate its heat efficiently. In the opposite limit that radiative cooling is *in*efficient, the solution for the disk structure becomes radically different. Several models attempt to produce characteristics of such systems and range from slim disks (Abramowicz et al. 1988) to advection-dominated accretion flows (ADAFs, Narayan & Yi 1994). One way of constraining disk accretion observationally is to predict the AGN continuum emission and compare it to observed spectra. In some cases (particularly the optical/UV emission) data support the notion of thin, optically thick accretion disks (e.g. Malkan 1983), but the expected shape of the continuum does not always agree (Shang et al. 2005) and models are ultimately too simple to predict detailed characteristics of the spectrum (Koratkar & Blaes 1999).

The idea that accretion requires the inflow of mass and inherently generates the outflow of radiation leads to a limit found by equating these two forces. Historically defined in the context of massive stars (homogenous, spherically symmetric, and in hydrostatic equilibrium), the Eddington limit arises from the maximum luminosity beyond which radiation pressure will overcome the gravitational forces holding the star together. Assuming that the material

is fully ionized and radiation forces occur via Thompson scattering on free electrons, the Eddington luminosity becomes

$$L_{\rm Edd} = 4\pi G M \mu_e m_p c/\sigma_T, \tag{1.7}$$

where G is the gravitational constant, μ_e is the mean molecular weight per electron, m_p is the proton mass, c is the speed of light, σ_T is the Thompson cross section, and M is the mass of the star (Frank et al. 2002).

In the case of accretion disks, the luminosity of a central object is derived from the rate of matter inflow, by the conversion $L = \epsilon \dot{M} c^2$, with ϵ being the radiative efficiency, which measures how efficiently rest-mass energy of accreted material is converted into radiation. If accretion is truly Eddington limited, then the rate of mass inflow is proportional to the MBH mass.[10] For this reason an AGN luminosity is often quoted in terms of the Eddington accretion rate $\dot{M}_{\rm Edd} \equiv L_{\rm Edd}/\epsilon c^2$. From a comparison of the optical quasar luminosity function to the remnant MBH mass function, it is estimated that $\epsilon \sim 0.1$ (Yu & Tremaine 2002).

1.5.2 Numerical hydrodynamics

In general, deriving accretion models such as the Shakura-Sunyaev disk entails starting with the equations that describe fluid dynamics and making approximations such that they become solvable. This is the basic approach of hydrodynamics, which aims to describe the behavior of fluids treated as a continuous medium. Rather than dealing with the interacting particles at a microscopic level, fluids are described by well-defined macroscopic properties: density, pressure, bulk velocity, and internal energy, the evolution of which can be described by a set of partial differential equations. In astrophysical hydrodynamics we are generally

[10] Note, however, that there are various models that allow for mass inflow at super-Eddington rates (e.g. Begelman 1979; Inayoshi et al. 2016).

dealing with compressible flows of gas (or plasma, when highly ionized) in extreme conditions. In the context of accretion disks, these flows are subject to powerful gravitational forces. The basic equations that describe the evolution of a compressible, inviscid flow in the presence of a gravitational field are comprised of conservation laws:

$$\frac{\partial \rho}{\partial t} + \nabla \cdot \rho \mathbf{v} = 0 \qquad \text{(mass conservation)} \tag{1.8}$$

$$\frac{\partial \rho \mathbf{v}}{\partial t} + \nabla \cdot \rho \mathbf{v}\mathbf{v} + \nabla p = \rho \mathbf{g} \qquad \text{(momentum conservation)} \tag{1.9}$$

$$\frac{\partial \rho E}{\partial t} + \nabla \cdot (\rho E + p)\mathbf{v} = \rho \mathbf{v} \cdot \mathbf{g} \qquad \text{(energy conservation)} \tag{1.10}$$

where t is the time coordinate, ρ is the fluid density, $\mathbf{v}$ is the velocity, p is the pressure, $\mathbf{g}$ is the gravitational acceleration, and E is the sum of the internal energy ϵ and the kinetic energy per unit mass, $E = \epsilon + \frac{1}{2}|\mathbf{v}|^2$. These equations, referred to as Euler's equations, describe the conservation of mass, momentum, and energy, respectively.

Note that additional terms appear in these equations for non-ideal fluids, i.e. when viscosity or conductivity enter the picture. For example, in accretion disks, shear stresses can transfer momentum. This arises as viscous terms in the momentum equation, and Eq 1.9 becomes the Navier-Stokes equation,

$$\frac{\partial \rho \mathbf{v}}{\partial t} + \nabla \cdot \rho \mathbf{v}\mathbf{v} + \nabla p = \rho \mathbf{g} + \mu \nabla^2 v + \frac{1}{3}\mu \nabla (\nabla \cdot v) \tag{1.11}$$

where μ is the dynamic viscosity. Similarly, source terms arise in the energy equation that can correspond to viscous dissipation, conduction, or heating when present (see e.g. Shu (1992)).

Additionally, one can assign an equation of state (EOS) of the fluid to describe the nature of the gas, which attempts to summarize all microscopic interactions into a simple relation

(e.g., $p(\rho)$). In the simplest case, one can use the ideal gas law, for which

$$p \propto \rho^{\gamma} \tag{1.12}$$

where γ is the ratio of specific heats, referred to as the adiabatic index. For an isothermal gas, $\gamma = 1$ and $p \propto \rho$. It is important to note that prescribing an EOS carries assumptions about the thermal properties of a fluid. Throughout this Dissertation, we adopt accretion disk models that are locally isothermal, meaning the temperature profile is held to a pre-assigned value. This implicitly assumes that there exists some process that keeps the fluid temperature constant, or, equivalently, that the gas can radiatively cool efficiently. This can be a reasonable approximation if the cooling rate of the gas is a steep function of temperature. But in the case that radiation cannot effectively escape, a different EOS (i.e. adiabatic) may be appropriate. In general, isothermal and adiabatic prescriptions are considered simplified limiting cases, and resolving the true behavior of the gas requires a treatment of radiative cooling and radiative transfer across the region of interest.

The Euler equations combined with an EOS comprise a full set of equations, providing the tools to describe the behavior of a fluid. However, due to the coupled nature of these equations, obtaining an analytical solution is not trivial and often requires making extensive assumptions (e.g. geometrical assumptions such as axisymmetry, or steady state solutions with $\partial t = 0$). In the case of multidimensional flows in complex astrophysical systems, such as a gas disk embedded in a time-dependent binary potential, analytic solutions are no longer possible, and instead it is more tractable to employ numerical schemes. There are several methods for solving the fluid equations numerically − each is an approximation to the true solution, and may have advantages or disadvantages depending on the problem of interest.

Historically the two leading approaches to simulating a fluid flow are divided by the frame

of reference. The first method, and the one adapted in some calculations presented in this Dissertation, is the Eulerian framework, which involves determining approximate solutions the fluid equations in a static coordinate system. In this method a fluid configuration is defined across a spatially discretized volume comprised of 'cells,' each with assigned fluid parameters. The evolution of each parameter and corresponding flux through adjacent cells is then calculated based on the conservation laws. In general, the accuracy of the solution will be limited by the available resolution. Some codes offer the possibility of "adaptive mesh refinement" (AMR), allowing the grid resolution to change with the complexity of the fluid flow. In Chapter 4, we adopt one such method for simulating a slice of an accretion disk, using the parallelized grid-based simulation code FLASH (Fryxell et al. 2000). FLASH solves the fluid equations by using a piecewise parabolic representation of the variables to interpolate between the cells, making it accurate to 2nd order in space and time. This is particularly ideal for capturing dynamical instabilities and resolving sharp shock fronts, as contact discontinuities are dealt with by its very nature.

Alternatively, one can solve the fluid equations in a Lagrangian framework, in which the fluid is described by a set of fluid 'particles' (discretizing the fluid into mass elements, rather than volume elements). This type of approach is adopted in the Smoothed Particle Hydrodynamics method (SPH, Springel (2010)), in which the gas properties on each particle are calculated by averaging over its nearest neighbors. This approach does not require choosing a pre-defined spatial grid, making it ideal for dynamical problems that entail a large volume (e.g. problems involving gravitational collapse, such as cosmological structure formation). Lagrangian methods by construction are Galilean invariant, meaning they have the ability to conserve linear and angular momentum perfectly. The conservation of momentum is independent of the geometry of the problem, whereas in grid-based codes this can only be achieved if the flow is aligned with the grid. However, SPH methods are not as well suited

for resolving contact discontinuities or steep density gradients (Bod 2007).

Increasingly popular is the development of 'moving-mesh' codes, that are essentially Eulerian-Lagrangian hybrids. In this method, the fluid equations are solved on a mesh that is dynamic: generated at each time step around a population of Lagrangian particles which follow the fluid flow. Moving-mesh codes conserve quantities almost as well as SPH methods, and can also capture shocks and contact discontinuities as well as grid codes. In Chapters 2 and 3, we take advantage of this technique by using the code DISCO (Duffell 2016), which is specifically tailored to solve problems associated with supersonic accretion disks. In DISCO, the computational domain is discretized into zones that are cylindrical wedges with a user-defined azimuthal velocity. Zones can move with the bulk motion of the flow in a shearing Keplerian configuration, making the scheme effectively azimuthally Lagrangian and significantly reducing advection errors associated with supersonic orbital motion.

1.5.3 Gas disks around MBH binaries

In the presence of a binary, accretion disk dynamics becomes highly nonlinear, and we turn to simulations to understand how binary-disk evolution takes place.

In the general picture, a binary exerts torques on surrounding gas, carving a cavity in the center of the disk. Circumbinary disk evolution has been explored in several hydrodynamical simulations (e.g. MacFadyen & Milosavljević 2008; Farris et al. 2014; D'Orazio et al. 2013; Muñoz et al. 2018; Shi et al. 2012), which independently show the formation of a central cavity, mini-disks around each component of the binary, streams flowing from the edge of the cavity towards and among the minidisks, and even non-axisymmetric 'lumps' that precess around the cavity and modulate the inflow of gas. Most of the inflowing gas is accreted by the secondary BH, leading to the prediction of modulated accretion rates for binary-disk

systems. Simulations also show that even when the binary is coalescing on a timescale faster than the viscous time, gas will follow the BHs all the way to merger (Farris et al. 2015a; Tang et al. 2018).

The traditional expectation has been that torques from the disk will remove angular momentum from the binary, causing it to merge. Recent simulations that resolve gas dynamics around each binary component with high resolution, however, find that gas near the BHs exerts a *positive* (i.e. outward) torque on the binary, forcing us to revisit our understanding of MBHB evolution (Tang et al. 2017; Muñoz et al. 2018; Duffell et al. 2019a; Moody et al. 2019).

1.5.4 Embedded BHs and migration

For binaries with small to extreme mass ratios ($q \lesssim 10^{-2}$), gas disk dynamics around a binary enters a different regime. In this case the dynamics is analogous to planets embedded in protoplanetary disks, a field that inspired much of this work. In the context of planet migration, several models and theoretical frameworks have been developed in an attempt to explain the variety of orbital configurations of exoplanet systems (see Baruteau et al. 2014a for a review). While the physical scales, temperature and density regimes, and timescales vary between protoplanetary and AGN disks, much of the underlying physics is comparable.

An embedded satellite (be it a black hole, a planet, or any compact object with non-zero mass) placed in a disk will perturb the disk, producing non-axisymmetric density waves. These non-axisymmetric perturbations interact with the perturber's orbit, leading to an exchange of angular momentum that will increase or decrease its orbital separation. This process is referred to as migration.

There are different regimes of migration depending on the mass of the satellite and characteristics of the disk in which it is embedded (Ward 1997). If the satellite mass is

sufficiently low such that it does not significantly alter the disk structure, it is referred to as Type I migration. In this case the satellite excites density waves in the disk (Goldreich & Tremaine 1980). The resulting torque on its orbit can be solved with linearized disk equations, and has been confirmed in numerical simulations by Tanaka et al. (2002) that verify an analytical formula for the migration rate in isothermal disks. However, more recent simulations show that the migration rate is sensitive to the equation of state of the gas (Paardekooper & Mellema 2006) and so this linear approximation is not always valid.

For more massive satellites, or mass ratios closer to unity, the picture becomes yet more complex. A massive enough perturber will significantly deplete the gas density in its orbit. This results in an annular 'gap' in the disk, which can contain streams of gas flowing across the secondary's orbit on horseshoe orbits (Lubow et al. 1999). In this regime, referred to as Type II migration, the disk evolution is highly nonlinear and the concomitant migration rate is difficult to predict. In most cases it is typically inferred to be much slower than the Type I migration rate, but even a slight change of satellite mass or disk parameters can cause the migration to change direction entirely (Duffell 2015b; Kanagawa et al. 2018).

The challenge with modeling these systems is that (i) the global disk must be resolved to capture the non-axisymmetric perturbations that are responsible for gas flowing across the gap, in addition to (ii) resolving the gas flow on scales close to the satellite in order to accurately measure the torque, and (iii) thousands of orbits must be followed to achieve a quasi-steady state so as to avoid measuring transient phenomena. Thus, in the case of MBH binaries, models of inspirals at $10 - 100$ Schwarzschild radii of the primary MBH ($r_{\rm S}(M_1)$) need to be resolved to scales down to $< 10 r_{\rm S}(M_2)$ of the secondary BH for several dynamical times. This can be computationally expensive for systems of extreme mass ratios where the secondary's event horizon is orders of magnitude smaller than the primary's.

For reference, we show snapshots of various binary-disk simulations in Figure 1.2, ob-

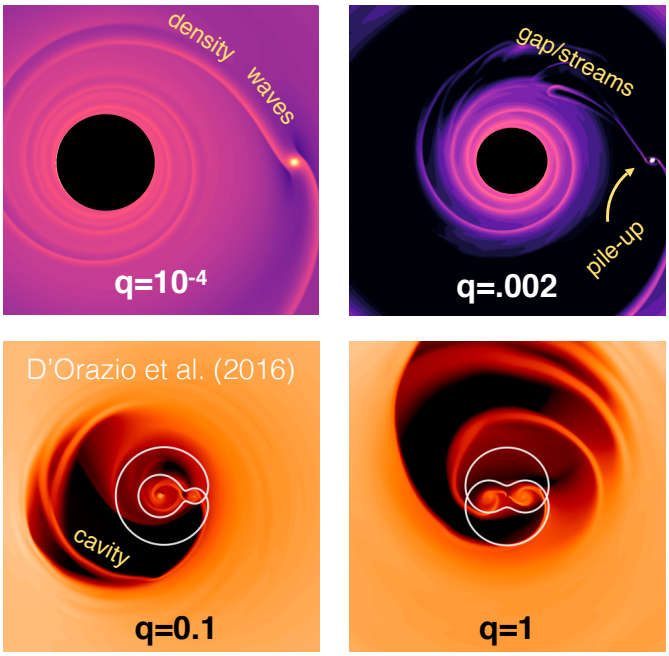

Figure 1.2: Snapshots of gas surface density from various two-dimensional simulations of point masses embedded in isothermal, viscous accretion disks. In the top panels the primary MBH is excised from the domain, focusing on the gas dynamics in response to an embedded intermediate mass ratio satellite. The bottom panels resolve accretion flow around both binary components. These are adapted from Figure 9 of D'Orazio et al. (2016) (with permission from the authors). Depending on the binary mass ratio, the disk will form density waves, gaps, or a circumbinary cavity. In all cases gas flows near the BHs.

tained with the moving-mesh hydrodynamics code DISCO (Duffell 2016). The top panels are for intermediate mass ratio binaries, where the primary MBH is excised from the simulation domain. Increasing the satellite mass by an order of magnitude brings the disk response into a highly nonlinear regime with gaps, streams, and a significant pile-up around the satellite. The bottom panels, borrowed from simulations by D'Orazio et al. (2016), contain both binary components in the near-equal and equal mass regime, where the gas forms a lop-sided cavity.

When scaled to MBH binaries in AGN disks, this nonlinear gas response can have inter-

esting consequences for their orbital properties and evolution. As we will show in Chapters 2 and 3, details in binary-disk interaction can have implications not only for what LISA will detect but for how its GW signals may be altered.

1.6 Multi-messenger Astrophysics opportunities with LISA

GWs will provide a wealth of information on their own that is unavailable electromagnetically, but even more physics can be done when the GWs are combined with electromagnetic (EM) signatures (Tamanini 2016; Baker et al. 2019). This field is referred to as Multi-Messenger Astrophysics (MMA), which includes coincident or correlated detections of GWs, EM radiation, and / or neutrinos and cosmic rays. Synergies between these observations provide opportunities for testing theoretical models, testing general relativity, and constraining cosmological parameters.

The most exciting opportunity for MMA in the context of MBH binaries can be done with those that will fall in the LISA band. Since BH mergers are associated with galaxy mergers, they are perfect candidates for events with the possibility of EM emission that will also be loud in GWs. While localization with LISA is good ($\lesssim$ 10s of deg^2, ultimately improving to O(deg^2) as the as the source chirps, see Lang & Hughes 2008; Kocsis et al. 2007; Klein et al. 2016), it is insufficient to identify a unique host galaxy. An associated EM counterpart can provide a localization and the redshift of the source, allowing us to probe the MBH merger rate over cosmic history.

EM counterparts to LISA sources can be separated into two categories with respect to their timing relative to the GW emission. This includes *pre-cursor* signatures, which occur as the binary is coalescing in the LISA band, and *post-merger* signatures which occur sometime

after coalescence.

Precursor signatures are predicted from models of binary accretion in the regime where the binary is dominated by GWs. Simulations predict variable accretion signatures that can be coherent with the binary period and hence the GW phase (Tang et al. 2018). These 'EM chirps' (Haiman 2017), coincident with GW emission, can be used to localize the source as it evolves through the LISA band.

Post-cursor signatures focus on the response of the environment immediately after a binary merger. In the final stages of coalescence the binary is essentially replaced by a new central MBH with a different mass, spin, and velocity, which can perturb the surrounding medium. Such post-merger flares have been modeled in several works (Lippai et al. 2008; Corrales et al. 2010; Rossi et al. 2010; Rosotti et al. 2012). In Chapter 4 of this Dissertation , we discuss this response in more detail, and how its emission may be different than proposed by previous works due to the possibility of non-thermal emission.

1.7 This Dissertation

This Dissertation is motivated by future GW detections by both PTAs and LISA, which will provide a previously inaccessible view of MBHBs in the coming decade. The future of GW astronomy is rich with opportunity, but interpreting future detections will require a careful understanding of the physical processes that come into play during various stages of the binaries evolution to coalescence.

Overall the role of gas is complex: MBHBs can exist within a range of masses, mass ratios, spins, and orientations, and the impact of gas in each of these regimes has significant consequences for their orbital evolution. Nuances in binary-disk interaction warrant careful investigation because they have critical implications for what LISA and PTAs will detect.

Simulations are a remarkable tool for studying astrophysical phenomena that we cannot directly observe and for predicting and interpreting what future instruments may detect. Simple numerical models that elucidate key physical processes in a clear manner are the primary tool of this work.

In Chapter 2, we investigate the evolution of an intermediate mass ratio inspiral in an accretion disk, focusing on the torques exerted by the gas onto the secondary BH, and demonstrating when this produces a detectable GW waveform deviation. In Chapter 3, we extend on this work with a parameter study that shows the sensitivity of gas torques to small changes in the binary mass ratio and disk viscosity and temperature, and attempt to describe the evolution of gas torque during a GW inspiral for a range of systems. In Chapter 4, we move to electromagnetic counterparts: simulating perturbations produced in a disk following a MBHB merger, we show the sensitivity of the disk response to disk parameters, and lay out the case for non-thermal emission. We conclude in Chapter 5 and briefly discuss future work as extensions of this Dissertation .

Chapter 2

Probing gas disk physics with LISA: simulations of an intermediate mass ratio inspiral in an accretion disk

2.1 Introduction

LISA is currently planned to launch by 2034 and is expected to herald the era of space-based interferometry with the detection of gravitational waves (GWs) at wavelengths larger than the Earth. With an interferometer arm-length of 2.5 million km, LISA will probe the mHz GW sky with the primary goal of detecting merging supermassive black holes (SMBHs) throughout cosmic history. While the loudest sources in the LISA frequency band include merging SMBHs with component masses $M_{\rm BH} \sim 10^4 - 10^7 M_\odot$ up to a redshift $z \sim 20$, LISA will also be sensitive to less massive compact objects coalescing with SMBHs. These events are referred to as intermediate mass ratio inspirals (IMRIs; $q \equiv M_2/M_1 \approx 10^{-3} - 10^{-4}$) or

This section contains text from an article originally published as Derdzinski et al. (2019) in Monthly Notices of the Royal Astronomical Society, Volume 486, Issue 2, p.2754-2765

extreme mass ratio inspirals (EMRIs; $q \lesssim 10^{-4}$, detectable up to $z \sim 4$, Amaro-Seoane et al. 2017).

Unlike stellar-mass BH mergers which are presumed to occur in vacuum (although see Perna et al. 2016; Janiuk et al. 2017; Bartos et al. 2017; McKernan et al. 2017; Stone et al. 2017; D'Orazio & Loeb 2018b), many LISA events may occur in gaseous environments in galactic nuclei. Only $\sim 1\%$ of galaxies host active galactic nuclei (AGN), in which the central SMBH is accreting at nearly the Eddington rate from a thin, cold accretion disc, but there is plenty of evidence that AGN are triggered by galactic mergers (e.g. Kauffmann & Haehnelt 2000; Hopkins et al. 2008; Goulding et al. 2018 and references therein). In particular, the merger of two massive galaxies results in a supply of gas that flows into the nucleus of the post-merger remnant (Dotti et al. 2012; Barnes & Hernquist 1996), providing a gas-rich environment for BH accretion. a As a result, a large fraction of SMBH mergers are expected to occur in a gaseous environment (see, e.g. Mayer 2013 for a review).

If a coalescing compact BH binary encounters a sufficient amount of gas, it will experience a gravitational torque that can act to either accelerate or hinder a GW-driven inspiral. The presence of gas also provides the opportunity for BHs to accrete, which in turn will affect their mass, spin, and momentum. This raises an important question: could gas change the orbital evolution of a binary sufficiently strongly such that the corresponding changes in the GW waveform become measurable? If it does, the GW signal would not only provide information about the source parameters, but it also would carry a characteristic signature of the environment in which the source originated.

Thus far the impact of gaseous forces on GW signals has been addressed only via semi-analytical toy models (Kocsis et al. 2011; Yunes et al. 2011; Barausse et al. 2014, 2015c). The overall conclusion from these studies is that gas has a negligible impact for SMBH binaries in the LISA band, except for systems with extreme mass ratios ($q \ll 1$). Environmental

influences become important for sources with less massive companions, where GWs are weaker and gas effects are comparatively stronger. Semi-analytical estimates by Kocsis et al. 2011 focused on EMRIs and found that a dense, near-Eddington gas disk can speed up the inspiral to an extent observable by LISA.

GW sources with $q \ll 1$ include a range of possible SMBH component masses, but in the present study we focus on IMRIs that will fall in the mHz GW band. The two relevant cases in this regime include the mergers of massive stellar remnant BHs ($M_{\rm BH} \sim 10 - 100 M_\odot$) with IMBHs ($M_{\rm BH} \sim 10^{4-5} M_\odot$), or $10^{3-4} M_\odot$ IMBHs coalescing into $10^{6-7} M_\odot$ SMBHs. For our detectability estimates we adopt the specific case of a $q = 10^{-3}$ mass-ratio binary with a primary BH mass of $M_1 = 10^6 M_\odot$.

IMRI rate estimates predict a few to tens of mergers per year in the universe (Amaro-Seoane et al. 2007; Miller 2009). These estimates are based on stellar dynamical processes in galactic nuclei, and only a small fraction of these events would be expected to occur in a gaseous environment. However, IMRIs could also occur in AGN disks via several additional evolutionary pathways, either from compact objects in the galactic nucleus whose orbits are dragged into the plane of the disk by repeatedly crossing the disk (e.g. Ivanov et al. 1999; McKernan et al. 2012; Kennedy et al. 2016 and references therein), or from compact remnants that are formed in the disk in the first place (e.g. Goodman & Tan 2004; Levin 2007; McKernan et al. 2014; see also Stone et al. 2017). Subsequent accretion and mergers of these remnants can lead to IMBHS embedded in AGN disks (e.g. Bellovary et al. 2016; Yi et al. 2018). Similarly to near equal-mass SMBH mergers, E/IMRIs may preferentially occur in AGN disks.

The previous studies mentioned above estimate the gas impact on E/IMRIs in near-Eddington accretion disks with semi-analytical models of the so-called migration torque. For IMRIs in particular, these migration torques are based on the viscous torque and are

estimated for a non-inspiraling perturber on a fixed circular orbit. However, a rapidly inspiraling, GW-driven perturber modifies the disk structure differently from a non-migrating perturber. As a result, the torques for a moving perturber differ in both strength and sign from the torques for a perturber on a fixed orbit (Duffell et al. 2014), and should also evolve differently during the inspiral.

Motivated by the above, in this paper we perform high–resolution two–dimensional (2D) hydrodynamical simulations, and we directly measure the torques exerted on an IMBH embedded in the accretion disk of a central SMBH. We use the moving-mesh grid code DISCO (Duffell 2016), model the IMBH as a sink particle, and assume its orbit follows a GW-driven inspiral. The disk is assumed to have a locally isothermal equation of state and to obey a standard α-prescription for its viscosity. We calculate the impact of the disk torques throughout the coalescence, and predict the corresponding modification to the GW waveform seen by LISA. We also compute the signal-to-noise ratio (SNR) of the detectability of these modifications.

Focusing on the intermediate mass-ratio regime has two advantages compared to EMRIs. First, the inspiral is more rapid, allowing us to simulate a large portion of the inspiral as it traces out a broad range of orbital separations and frequencies. Second, the system is easier to resolve numerically, allowing us to follow the system for as many as $\approx 10,000$ binary orbits.

Our primary goal is to estimate the detectability of the gas imprint on an IMRI with the currently proposed LISA configuration (Klein et al. 2016). The torques scale linearly with the mass of the AGN disk involved, and also depend on other disk properties, such as temperature and viscosity. Therefore, a measurement of a gas imprint on the inspiral waveform should probe the properties of the accretion disk in which the source resides.

This paper is organized as follows. In § 2.2, we summarize previous work on migration

torques in more detail. In § 2.3, we describe our simulation setup, and in § 2.4 we present our results, focusing on the torque measurements. In § 2.5 we use the measured torques to compute the modifications of the GW signal and estimate their detectability with LISA. In § 2.6, we discuss our results, along with some caveats, and finally in § 2.7 we summarize our conclusions and the implications of this work.

2.2 Previous work on migration torques for GW sources

Early estimates of the impact of a gas disk on the gravitational waveforms of a compact object (CO) spiraling into a SMBH appear in Chakrabarti (1996) and Narayan (2000). These studies focused on the angular momentum exchange between the CO and the disk due to accretion and hydrodynamical drag in disk models at different radiative efficiencies. Levin (2007) considered, additionally, the impact of torques from density waves excited in a thin accretion disk (Goldreich & Tremaine 1980), often called "Type I torques" in the context of extrasolar planets (see below). The impact of a broader range of environmental effects on EMRI gravitational waveforms has been enumerated in Yunes et al. (2011) and Barausse et al. (2015a).

These studies found that the effect of gas is generally very weak and undetectable for LISA sources.[1] The exceptions are systems with a small ratio, for which the gas torques due to the tidal deformation of the disk (so-called migration torques) can produce detectable deviations to the GW torque. Such disk torques are more extensively studied in the context of protoplanetary disks and planet migration, including numerous two- and three-dimensional hydrodynamical simulations (see a review by, e.g. Baruteau et al. 2014b).

[1]It is worth noting that gas disks could be much more important, and produce order-unity effects, for the more massive, sub-parsec separation $\sim 10^9$ $M_\odot$ SMBH binaries at nano-Hz frequencies, detectable by pulsar timing arrays (Kocsis & Sesana 2011; Tanaka et al. 2012; Sesana et al. 2012).

In the protoplanetary disk context, migration is described by two limiting cases (Type I and Type II; Ward 1997). Type I torques on low mass-ratio planet systems ($q < 10^{-4}$) are well understood, in the sense that they can be described by a linear perturbation theory (Goldreich & Tremaine 1980), which is successfully reproduced in numerical studies (e.g. Tanaka et al. 2002). However, these torques can be sensitive to disk thermodynamics (Paardekooper & Mellema 2006). Type II migration concerns more massive planets that can carve gaps in their disks (for intermediate masses $q > 10^{-3}$, with the precise value depending on the disk viscosity and temperature). In this regime the torques become nonlinear, so there is no analytical solution for the migration rate. Often, semi-analytical estimates are based on the viscous torque, but hydrodynamical simulations show that migration in this regime can deviate significantly from the viscous rate (Edgar 2007; Crida & Morbidelli 2007; Duffell et al. 2014; Robert et al. 2018). For intermediate mass perturbers in particular, the torque develops a nonlinear component that is remarkably sensitive to disk parameters such as the viscosity, Mach number, and density gradient (Duffell 2015b).

In the context of binaries embedded in AGN disks, Yunes et al. (2011) and Kocsis et al. (2011) computed modified waveforms, using semi-analytical formulae of the above planetary migration torques, for both extreme and intermediate-mass perturbers. Kocsis et al. (2011), in particular, showed that the gas-induced drift in the accumulated GW phase can exceed a few radians per year (depending on disk parameters), a limit that is detectable with LISA's sensitivity. For the most massive disk models, the drift can become as large as 1,000 radians per year, which provides the possibility for LISA to accurately probe disk parameters (possibly limited by degeneracies between migration and system parameters).

In our present study, we focus on the analog of gap-opening satellites (for $q = 10^{-3}$) in the context of BHs. While similar to the planet case, there are three major differences: (1) the BHs accrete, which is typically ignored when calculating planetary torques, (2) the BH orbit

is strongly dominated by GWs (in the LISA band), there is no analogous "external" force in the planet case, and (3) the physical parameters of AGN disks differ from protoplanetary disks, which are typically thicker (lower Mach number) and have a lower viscosity.

The combination of these effects on migration torques has not been studied in detail in any simulation to date. For completeness, we note that related works exist, which present simulations of gas disks that include unequal-mass, GW-driven binaries, both in 1D (Chang et al. 2010; Fontecilla et al. 2017; Tazzari & Lodato 2015) and in 3D (Baruteau et al. 2012; Cerioli et al. 2016). These studies aimed at understanding the tidal squeezing of the inner disk by the inspiraling companion (a 'snow-plow' effect), and the resulting enhanced accretion rate onto the primary BH and electromagnetic (EM) emission. These works did not measure the gas torques on the binary. Likewise, recent 2D simulations followed the GW-driven inspiral of an equal-mass SMBH binary (Farris et al. 2015a; Tang et al. 2018) in the LISA band, but focused on the accretion rates and electromagnetic (EM) emission, and did not measure the torques in this regime.

Finally, we note the work of Duffell et al. (2014), whose results directly inspired the present study. These authors measured the torques on a Jupiter-like planet ($q = 10^{-3}$), embedded in a protoplanetary disk, and migrating at a broad range of *manually prescribed* rates. By measuring the torques as a function of the rate at which the planet is dragged inward, a unique migration rate can be identified that is consistent with the torques measured at that rate. This is meant as a "trick" to avoid a numerically challenging simulation of a "live" binary coupled to the disk. However, as a by-product, Duffell et al. (2014) inadvertently studied migration in a case similar to GW-driven inspiral. They found that above some migration rate ($a(da/dt)^{-1} \gtrsim 10^5 t_{\rm orb} \sim t_{\rm visc}$, where a is the binary separation, $t_{\rm orb}$ is its orbital period, and $t_{\rm visc}$ the viscous timescale), the gas torques are modified. Interestingly, at sufficiently rapid migration rates, the torques change sign and start to slow down, rather

than speed up, the inspiral. While their study focused on non-accreting planets in proto-planetary disks, the dependence of torques on migration rate implies that the gas torques of a non-migrating secondary cannot simply be linearly added to the much larger external torques (in our case, from GWs).

In summary, in the present paper, we extend semi-analytic estimates of the modified GW waveforms (Kocsis et al. 2011), by running hydrodynamic simulations with a setup similar to Duffell et al. (2014), except with the addition of accretion, GW-driven migration, and a more AGN-like disk model. We expect that the torques we measure will be very sensitive to disk parameters, and therefore this study is but the first step toward a complete exploration of the importance of gas disks for LISA sources (Derdzinski et al, in prep).

2.3 Numerical methods

2.3.1 Disk model

Our model is a two-dimensional, locally isothermal, viscous gas disk, evolved using the moving-mesh grid code DISCO (Duffell 2016). DISCO is idealized for modeling accretion disks as it has the capability to allow the grid to move with the Keplerian flow of the gas, thus reducing advection errors produced by shearing flow between grid cells.

The computation domain extends from $0.5 \leq r/r_0 \leq 2.75$ where r is measured from the primary BH which is held at the origin, and r_0 is an arbitrary distance unit set to $r_0 = 1$. Likewise, the primary mass is set to $GM_1 = 1$ in code units (where G is the gravitational constant). Note that the orbital time in code units at $r = r_0$ (the final binary separation) is 2π. The grid is logarithmically spaced in polar coordinates, with a total of 512 radial cells and an increasing number of azimuthal cells at outer radii such that the aspect ratio of each cell is unity. This resolution reaches 30 zones per scale height, which is important

for capturing the gas morphology around the secondary BH. To ensure that our resolution is adequate, we have performed a test run with 800 radial grid cells, and found that our measured torques do not change. We employ Dirichlet (fixed) conditions at the inner and outer boundaries to ensure a constant mass flux rate.

The disk is parameterized by a constant aspect ratio $h/r = \mathcal{M}^{-1}$, where h is the disk scale height, r is the distance from the SMBH, and $\mathcal{M}$ is the Mach number, assumed to be independent of r. Under this assumption, gas dynamics is scale-free as the black hole migrates through the domain, and the sound speed varies as $c_s = v_\phi/\mathcal{M}$, where $v_\phi = r\Omega$ is the orbital velocity and Ω is the initial Keplerian orbital frequency at r. Viscosity is set with an α-law prescription, with the kinematic viscosity provided by $\nu = \alpha c_s h$. We neglect radiative cooling and instead assume the disk is locally isothermal by setting the vertically integrated pressure to $p = c_s^2 \Sigma(r)$, such that the mach number and corresponding temperature profile remain fixed. Here $\Sigma(r)$ is the vertically-integrated surface density, which is assumed to follow

$$\Sigma(r) = \Sigma_0 \left(\frac{r}{r_0}\right)^{-1/2}, \tag{2.1}$$

where $\Sigma_0 \equiv \Sigma(r_0)$ is a constant scaling factor. Since the orbit of the secondary BH is imposed by hand (§ 2.3.2) and we have no self-gravity, Σ_0 can be scaled to any value. Gas forces on the BH simply scale linearly with Σ_0, as long as Σ_0 remains low enough not to significantly modify the orbit. This assumes that the evolution of the binary is overwhelmingly dominated by GWs, which we show to be valid in § 2.4.1 below.

For parameters describing the disk temperature and viscosity, we choose $\mathcal{M} = 20$ and $\alpha = 0.03$. While neither of these values are typical of what we expect in AGN disks (where we believe the gas is highly supersonic, with $\mathcal{M} \sim 100$ and highly ionised leading to $\alpha \sim 0.1$–0.3), we implement these values here because they are (i) numerically easier to simulate and (ii) this particular combination of $\mathcal{M}$ and α leads to a gap with a similar depth to a disk with

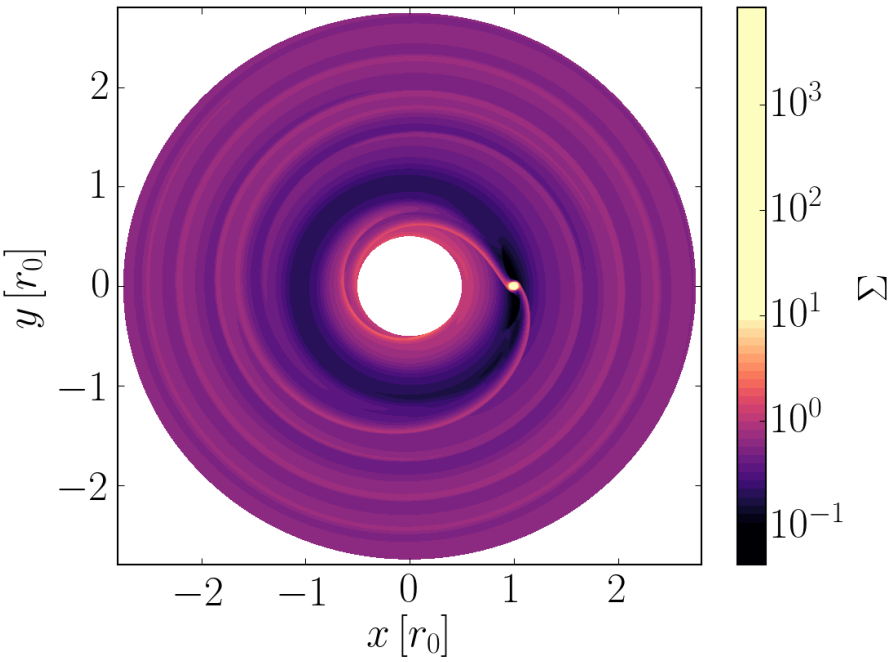

Figure 2.1: The logarithmic surface density over the whole computational domain, at the end of a simulation run. The primary BH is at the origin, and the gas disk and the secondary BH are both orbiting counter-clockwise. The secondary BH is located at $(x, y) = (1, 0)$, marked by a large overdensity.

AGN-like parameters.

Fig. 2.1 shows a snapshot of the logarithmic 2D surface density over the whole computational domain, at the end of an illustrative run.

2.3.2 The migrator and the GW inspiral

The primary BH is held at the origin which is excised from the simulation domain. The secondary BH is placed in a prograde orbit, and modeled by a 'vertically averaged' potential

of the form

$$\Phi_2 = \frac{GM_2}{({r_2}^2 + \epsilon^2)^{1/2}}, \tag{2.2}$$

where r_2 is the distance to the secondary BH and ϵ is a smoothing length, which we set to one half the scale height. This approach essentially neglects the gravitational pull of the secondary from within $r_2 < \epsilon < r/\mathcal{M}$. The purpose of smoothing the potential is not only to avoid the singularity at the position of the secondary, but to mimic the vertically integrated forces that the two-dimensional fluid elements feel within a scale height of the BH (see Tanaka et al. 2002; Masset 2002; Müller et al. 2012).

While the disk is initially steady, it experiences perturbations in response to the placement of the secondary BH. These perturbations are transient and decay after a viscous time. The viscous time is given by

$$t_{\rm visc}(r) = \frac{2}{3}\frac{r^2}{\nu} = \frac{\mathcal{M}^2}{3\pi\alpha} t_{\rm orb}(r) \approx 1415 \left(\frac{\mathcal{M}}{20}\right)^2 \left(\frac{\alpha}{0.03}\right)^{-1} t_{\rm orb} \tag{2.3}$$

where $\nu = \alpha c_s h = \alpha h^2 \Omega$, is the kinematic viscosity, and we define $t_{\rm visc}$ as a function of orbital time $t_{\rm orb}$ at the secondary location r. We therefore disregard the dynamics during the first 1400 orbits of the simulation when measuring the torques, to avoid including numerical transients. (Note that the secondary only moves a distance of $\sim 0.1 r_0$ during this phase.)

For a binary being driven together by gravitational waves, the quadrupole approximation (Peters 1964) for the evolution of the orbital separation is

$$\dot{r}_{\rm GW} = -\frac{64}{5}\frac{(GM)^3}{c^5}\frac{1}{1+q^{-1}}\frac{1}{1+q}\frac{1}{r^3}, \tag{2.4}$$

where G is the gravitational constant, c is the speed of light, and $M = M_1 + M_2$ is the total

binary mass. Integrating this expression, the secondary's position can be written as

$$r(t) = r_{\rm min}\left[1 - 4R(t - t_{\rm total})\right]^{1/4}, \tag{2.5}$$

where t is the elapsed time, $t_{\rm total}$ is the total simulation time, $r_{\rm min}$ is the final separation at $t = t_{\rm total}$, and $R \equiv \dot{r}_{\rm GW}/r$ is the inspiral rate defined at the final separation. In principle, we have the choice of specifying the initial and final position of the secondary in code units, as well as the physical scale for the total mass M (note that $q = 10^{-3}$ has already been fixed). In practice, we are numerically limited by the total number of orbits we can simulate ($\approx 10,000$ at our chosen resolution). Our choice for, say $r_{\rm min}$ and the physical mass scale, is further constrained in order for the binary to be chirping (i.e. changing its separation noticeably during the simulation), and for the GW frequency to fall in the LISA band. We therefore chose parameters that are appropriate for a LISA IMRI: $M_1 = 10^6 M_\odot$, $q = 10^{-3}$, $r_{\rm min} = 5r_{\rm S}$ (where $r_{\rm S} = 2GM_1/c^2$ is the Schwarzschild radius). Our choice of covering $\sim 10,000$ orbits leads to an initial position of the secondary BH being $r_{\rm max} = 11r_S$. Simulation parameters are defined in Table 2.1. Note that in code units, $r_{\rm min} = 1$ (i.e. twice the inner boundary), $r_{\rm max} = 2.2$.

The potential remains Newtonian, despite the fact that the final stages of the inspiral we simulate here are close to the innermost stable circular orbit (ISCO) of the central SMBH ($r_{\rm isco} = 3r_{\rm S}$ for a non-spinning BH). In reality the disk dynamics would be altered by relativistic effects, but we chose to start with the simpler, scale-free case before investigating more realistic additional physics in future work.

In a similar vein, throughout the inspiral we measure the torques exerted on the BH, but the BH does not respond to these torques. Restricting the BH to adhere to an imposed circular orbit is artificial: in reality, gas bound to the BH would imprint a time dependent

torque on it. As an analogy, the torque exerted by the Moon on the Earth is balanced by the torque from the Earth on the Moon. While the Earth would follow an epicyclic motion, the total angular momentum of the Earth-Moon system cannot change. One can therefore wonder whether in our case, by prescribing the Earth's orbit, we introduce spurious torques from the Moon and violate angular momentum conservation. However, one can show using the restricted 3-body approximation (Murray & Dermott 2000) in which the Moon's mass is zero (consistent with the massless disk assumed in our simulation runs) that the Moon's orbit is has a front-to-back symmetry around the Earth, spending equal times ahead and behind the Earth, and the net orbit-averaged torque vanishes. Not implementing a 'live' BH allows us to observe gas asymmetry and makes a single calculation scalable to any value of Σ_0. As we show below, the migration rate of the BH is strongly dominated by GW emission, and gas torques only impart a very small deviation.

2.3.3 Accretion Prescription

To model accretion onto the migrating secondary BH (M_2), we implement a sink prescription similar to Farris et al. (2014) and Tang et al. (2017). Within a sink radius centered on the BH, the surface density of the gas is reduced on the local viscous timescale, assuming the gas surrounding the secondary settles into a mini-disk with parameters $\mathcal{M} = 20$ and $\alpha = 0.03$. The sink radius is set to be the smoothing length of the gravitational potential ϵ, since we do not resolve the BH's event horizon. There are 15 cells across the accretion sink, which in physical units extends to 125 Schwarzschild radii (in radius) of the secondary BH.

The accretion timescale for the secondary BH is given by the viscous time of the mini-disk, $t_{\rm visc}(\epsilon) = (2/3)(\epsilon^2/\nu)$. This is implemented with a new source term, which reduces the

surface density inside the sink at the rate

$$\frac{d\Sigma}{dt} = -\frac{\Sigma}{t_{\rm visc}} \exp -(r_2/r_{\rm sink})^4. \tag{2.6}$$

The exponential factor acts to smooth the sink radius boundary, in order to reduce numerical artifacts that arise from discontinuous changes in the surface density.

In the context of a steady α-disk model, choosing a Mach number together with physical units for length and surface density implies an accretion rate which tends to be well in excess of the Eddington rate ($\dot{M}_{\rm Edd} \equiv L_{\rm Edd}/(\epsilon_{\rm eff} c^2)$, where $L_{\rm Edd} = 4\pi G c \kappa_{\rm es}^{-1} M$ is the Eddington luminosity, $\kappa_{\rm es}$ is the electron scattering opacity, and $\epsilon_{\rm eff}$ is the radiative efficiency). Likewise, the accretion rate onto the secondary (Eq. 6) with our choice of $M = 20, \alpha = 0.03$, and our chosen length units implies $\dot{M}/\dot{M}_{\rm Edd} > 1$ for $\Sigma_0 > 10\,{\rm g\,cm^{-2}}$. Our estimates for Σ_0, derived in Section 2.4, exceed this limit and imply an accretion rate that is $10^3 - 10^8\,\dot{M}_{\rm Edd}$.

In other words, we are simulating disks that are unrealistically thick and have unrealistically high accretion rates. Unfortunately, we, as well as all similar global numerical disk studies, are unable to model disks that are sufficiently thin to correspond to sub-Eddington accretion rates. Such thin, cool disks are numerically challenging to simulate. In addition, our simulations neglect radiation, which is inconsistent with the large luminosity expected from near- or super-Eddington accretion. Radiation would certainly play a role in the gas properties around the secondary at these high accretion rates (although, we note that radiation-hydrodynamical simulations by Jiang et al. 2014 of super-Eddington accretion disks find that radiation preferentially escapes the disk in the vertical direction, allowing radiatively efficient accretion close to that expected in a thin disk).

For simplicity, we neglect the impact of radiation in the present work. In reality the accretion efficiency onto the secondary BH is uncertain, and our fiducial choice is an estimate.

Future work will explore the dependence of the gas dynamics and torques on the accretion efficiency.

2.4 Simulation results

Here we define the various components of the torque exerted on the inspiraling BH before directly comparing them in the simulation.

The dominant mechanism for angular momentum loss of the secondary BH is GW emission (§ 2.4.1), for which the torque is derived from the quadrupole formula:

$$T_{\rm GW} = -\frac{1}{2} M_2 r \dot{r}_{\rm GW} \Omega_2. \tag{2.7}$$

Note that we are assuming the center of mass is at the position of the primary, Ω_2 is the Keplerian orbital frequency of the secondary, and we quote the torques exerted on the secondary.

Gas can impart a torque on the secondary in two different ways – by gravitational interaction and by accretion. The gravitational torque $T_{\rm g}$ arises from the gravitational force exerted by the gas. We calculate this torque by summing up the $\phi-$component of the gravitational force $\mathbf{g}_\phi$ crossed with the binary lever arm $\mathbf{r}$ over all the grid cells in the disk,

$$T_{\rm g} = \sum |\mathbf{g}_\phi \times \mathbf{r}| \tag{2.8}$$

where $|\mathbf{r}|$ is the separation of the binary. We describe this torque in detail in § 2.4.1 and distinguish between positive and negative contributions from different regions of the disk.

Accretion onto the BH is another mechanism for angular momentum gain/loss. Assuming that the relative linear momentum of the accreted gas is added to the BH, the accretion

Simulation Parameters

Parameters		[cgs]	[code]
α	Viscosity parameter	0.03	0.03
$\mathcal{M}$	Mach number	20	20
ϵ	Smoothing length	$125\, r_{\rm S}({\rm M}_2) = 3.7 \times 10^{10}\,{\rm cm}$	0.025
$r_{\rm sink}$	Sink radius	$125\, r_{\rm S}({\rm M}_2)$	0.025
$\rm M_{BH}$	Mass of primary BH	$10^6\,{\rm M}_\odot$	$G{\rm M_{BH}} = 1.0$
q	Mass ratio $\rm M_2/M_1$	10^{-3}	10^{-3}
$\rm n_{orbits}$	Total # of simulated orbits	9,721	9,721
$\rm r_{min}$	Final binary separation	$5\, r_{\rm S}({\rm M}_1) = 1.5 \times 10^{12}\,{\rm cm}$	1.0
Derived parameters			
$\dot{\rm r}/{\rm r}$	GW inspiral rate at final r	$-2.59 \times 10^{-7}\,{\rm s}^{-1}$	-4.04×10^{-5}
$\rm r_{max}$	Initial binary r	$11 r_{\rm S}({\rm M}_1) = 3.3 \times 10^{12}\,{\rm cm}$	2.2
$\rm t_{total}$	Total simulation time	$2.16 \times 10^7\,{\rm s} = 0.68$ yr	$22{,}088.3 \times 2\pi$

LISA-related Parameters

$\rm f_{min}$	Initial GW freq. of binary	0.626 mHz
$\rm f_{max}$	Final GW freq. of binary	2.042 mHz
z	Redshift	1
τ	LISA mission lifetime	5 yrs
L	LISA arm length	2.5 million km
N	Number of laser links	6

Table 2.1: Definition of parameters used throughout the paper, with their adopted values in both physical and simulation units.

torque $T_{\rm acc}$ is calculated by summing the relative momenta contributed by the cells within the sink radius:

$$T_{\rm acc} = \sum_{\rm sink} \dot{m} |\mathbf{v}_{\rm rel} \times \mathbf{r}|, \tag{2.9}$$

where $\mathbf{v}_{\rm rel} = \mathbf{v_i} - \mathbf{v}_{\rm BH}$ is the velocity of the gas relative to the BH, and $\dot{m}$ is the accretion rate inside the sink, i.e. the integral of equation (2.6). As discussed in § 2.4.2 below, we find this component of the torque to be relatively insignificant.

Analytical estimates for Type II migration torques often utilize the viscous torque as a reference, which follows directly from equation (2.3) and is given by

$$T_\nu = -3\pi r^2 \Omega_2 \nu \Sigma. \tag{2.10}$$

The magnitude of gas torques (equations 2.8, 2.9, and 2.10) all depend linearly on the normalization of the surface density, a parameter we are free to choose. Estimates for Σ vary by several orders of magnitude depending on the chosen accretion disk model. In a steady-state Shakura-Sunyaev disk (Shakura & Sunyaev 1976), Σ is determined primarily by the assumed accretion rate $\dot{M}$ and the viscosity parameter α. In the inner regions of accretion disks where radiation pressure becomes dominant, Σ is heavily dependent on whether viscosity scales with the gas pressure or with the total pressure (including radiation). For the system we consider here, the inspiraling BH is deep within the radiation-pressure dominated zone. We adopt two estimates for our normalization Σ_0 (at the secondary's final radius at $r_{\rm min} = 5r_{\rm S}$) for the inner regions of thin, near-Eddington accretion disks that utilize each of these assumptions, representing low– and high–end estimates which bracket the range of expected densities.

We normalize our disk densities to represent AGN accreting at near-Eddington rates with a radiative efficiency $\epsilon_{\rm eff} = 0.1$. The low estimate is obtained from the seminal model for a

thin, viscous accretion disk by Shakura-Sunyaev (i.e. α-disk; Shakura & Sunyaev 1973), in which the viscosity is proportional to the total (gas + radiation) pressure. For this model, the surface density in the radiation-pressure dominated inner region is given by

$$\Sigma_\alpha = 88.39 \left(\frac{\alpha}{0.03}\right)^{-1} \left(\frac{\dot{M}}{0.1\dot{M}_{\rm Edd}}\right)^{-1} \left(\frac{r}{5r_{\rm S}}\right)^{3/2} {\rm g\,cm^{-2}} \tag{2.11}$$

where the fiducial choice for the accretion rate is 10% of the Eddington rate. In case the viscosity is proportional only to the gas pressure (i.e. for a so-called β-disk), the surface density at the same accretion rate is much higher. We estimate the surface density in this second model (see Haiman et al. 2009) as

$$\Sigma_\beta \;=\; 1.55 \times 10^7 \left(\frac{\alpha}{0.03}\right)^{-4/5} \left(\frac{\dot{M}}{0.1\dot{M}_{\rm Edd}}\right)^{3/5} \times \left(\frac{M}{10^6 M_\odot}\right)^{1/5} \left(\frac{r}{5r_{\rm S}}\right)^{-3/5} {\rm g\,cm^{-2}}. \tag{2.12}$$

2.4.1 Gas torques versus the GW torque

The gas torques measured in the simulation, along with the GW torques, are compared in Fig. 2.2. All torques are shown scaled by the viscous torque and as a function of the evolving binary separation. The first point we address is the strength of the gas torques relative to the GW torque. The gas torque we measure differs from the analytical estimates (based on the viscous torque T_ν) in both magnitude and direction. As Fig. 2.2 shows, the torque we find is $5-10$ times weaker than T_ν.

As Figure 2.2 shows, the gravitational torque we find is $5-10\times$ weaker than the fiducial viscous torque. Note that for gap-opening planets on fixed circular orbits, the standard Type-II torque would match the viscous torque T_ν to within a factor of few. This torque would cause the planet to migrate inward with a drift velocity matching that of the gas,

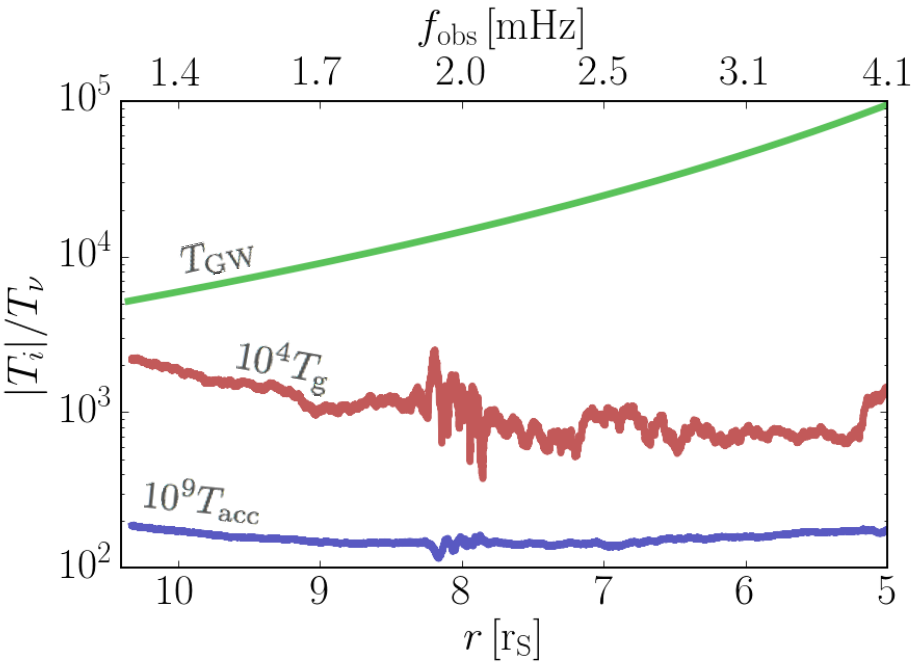

Figure 2.2: Different components of the total torque exerted on the secondary BH: gravitational torque ($T_{\rm g}$) and accretion torque ($T_{\rm acc}$) from the gas disk, as well as the torque from GW emission ($T_{\rm GW}$). All three torques are scaled by the fiducial viscous torque at the secondary's location. The gas torques are normalised to correspond to a β-disk (see equation 2.12). Note the overall different scale for each torque shown. The GW and accretion torques are both inward, while the gravitational torque is outward.

although when the disk mass is below the planet mass, angular momentum conservation implies that the drift velocity would decrease linearly with the ratio $4\pi r^2\Sigma_0/M_2$ (Syer & Clarke 1995).

In addition to being an order of magnitude weaker than standard Type II torques, for our disk parameters, the gravitational torque causes the secondary the migrate *outward* rather than inward (outward torques in isothermal disks have also been noted by Duffell 2015b). The torque also changes with migration rate, decreasing in strength as the secondary BH moves inward and accelerates. For the case that the surface density is high, resulting in the strongest torque (in the β-disk model), the gas torque is still several orders of magnitude weaker than the GW torque (Fig. 2.3). Nevertheless migration can still produce a detectable deviation in the GW signal, as we discuss in § 2.5.

Our simulation results can be used to understand the origin of gas torques in more detail, and how the different components depend on the accretion or migration rate of the BH. The entirety of the disk exerts some gravitational force on the secondary BH, including both the inner and outer disk, streams across the gap, and gas near the BH itself. We include all of these regions to calculate the total gas torque.

We find that gas closest to the BH, particularly within the Hill sphere, is the dominant contributor to the torque due to its close proximity. The Hill sphere is an approximation of an embedded body's sphere of influence in the presence of a more massive body at a distance a. Its radius is estimated as

$$r_{\rm H} = \left(\frac{q}{3}\right)^{1/3} a. \tag{2.13}$$

As gas flows across the gap, it can continue to replenish the net angular momentum of material in the Hill sphere of the secondary. This can cause an asymmetry within the Hill sphere, and a slight increase in the gas density upstream from the BH, leading to a consistently positive (outward) torque. This torque has been seen in other works (e.g.

D'Angelo et al. 2005). Accurately capturing the gas morphology within the Hill sphere requires high spatial resolution. Further work investigating the gas streamlines, particularly with high-resolution 3-dimensional simulations, will likely be necessary to accurately measure the torque arising from this asymmetry, and to fully understand the reason for the small front-back asymmetry that yields the net torque.

We note that in disk-satellite calculations, the torque within the Hill sphere is often ignored or "damped", based on the assumption that material within the Hill sphere is bound to the perturber (e.g. de Val-Borro et al. 2006; Dürmann & Kley 2017). However, gas flows through the Hill sphere − while some of it may become bound or accreted, certainly the majority flows across the gap to supply the inner disk. Asymmetrically distributed gas in this region can exert a net torque on the BH, which must be included if the BH and the gas is separately resolved and followed. This asymmetry, unlike a bound 'orbiter', is constantly supplied as gas flows across the gap. In our case the accumulation of gas leading the BH's orbit occurs because gas preferentially flows ahead of the BH and/or because it slows down (and hence spends more time) in this region.

Further evidence for torque inside the Hill sphere is present in simulations by Crida et al. (2009), in which a live BH experiences changes in migration rate when torques within the Hill sphere are truncated. In their case the planet migrates inward more quickly when the Hill region is included, suggesting an accumulation of gas in the trailing side of the planet's orbit. This is likely due to a difference in disk parameters since the dynamics are sensitive to viscosity and mach number. Ultimately truncating the torque in the Hill sphere gives a poor approximation to a self-consistent, highly resolved torque calculation, which suggests that this region is important. Our simulations sufficiently resolve gas flow within the Hill sphere, and thus we choose to not omit this region when computing the total torque.

Fig. 2.3 shows the torque broken into two components – inside and outside the secondary's

Hill sphere – along with smooth fits to the data which we use for calculating detectability in § 2.5. The Hill sphere torque is qualitatively different in that it settles to a positive value (it pushes outward). The gas from elsewhere in the disk, including the inner and outer disks, as well as the streams connecting the two regions, exerts a negative (inward) torque that is 1-5% of the viscous torque. Fig. 2.4 shows 2D torque density contours of each of these components. The left panel illustrates the torque density outside of the Hill sphere, which is dominated by the streams flowing across the secondary BH's orbit. The right panel zooms in on the torque density inside the Hill sphere, showing that there is a slight density increase in the gas in front of the BH (for a counterclockwise orbit). This asymmetry is responsible for the positive torque.

2.4.2 Accretion torque

For the fiducial accretion rate, we find that the accretion torque is negligible compared to the gravitational torque from the gas – their magnitudes differ by ~ 6 orders of magnitude, as seen in Fig. 2.2. This is because the relative velocity of the gas near the black hole is effectively negligible. We show this in Fig. 2.5, with a snapshot of the velocity field in a frame co-rotating with the binary. The gas close to the BH has low angular momentum and resembles a quasi-stationary atmosphere, rather than a near-Keplerian mini-disk.

Accretion plays a minimal role in our simulations. The most conspicuous effect of accretion is to reduce the density of the gas near the BH, which leads to a decrease in the positive component of the torque. Without including a sink, our results show the same asymmetry within the Hill sphere, albeit with more gas (and a larger positive component of the torque). The torque from elsewhere in the disk is unaffected by our sink prescription. We hypothesize that more efficient accretion (as well as feedback) would lead to more depleted gas density and less positive torque. A drastic increase in accretion rate may lead to other differences,

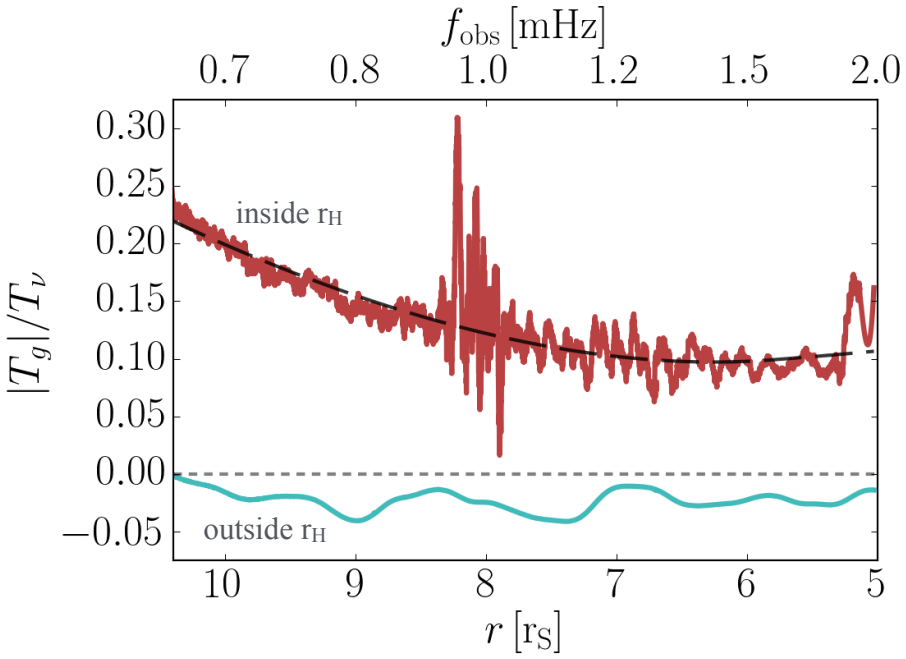

Figure 2.3: Gravitational torque T_g exerted by different regions of the gas disk onto the secondary BH, as a function of binary separation. The red (upper) curve shows torques from within the Hill sphere, and the green (lower) curve shows torques from outside this region. Both torques are scaled by the viscous torque. The dashed curve shows fitting formula we adopt for our LISA SNR computations (§ 2.5).

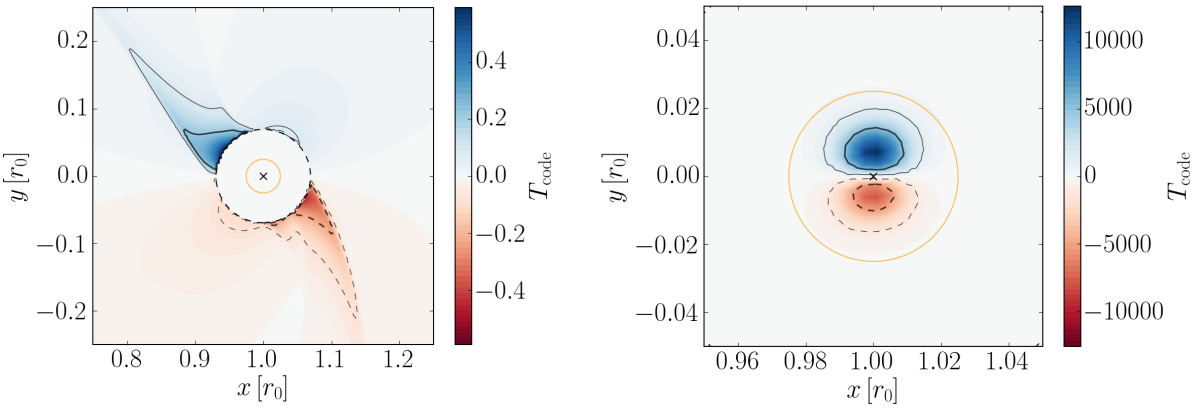

Figure 2.4: 2D contours of torque surface density, comparing the torques contributed by gas within the Hill sphere (right panel) to torques from gas outside this region (left panel).

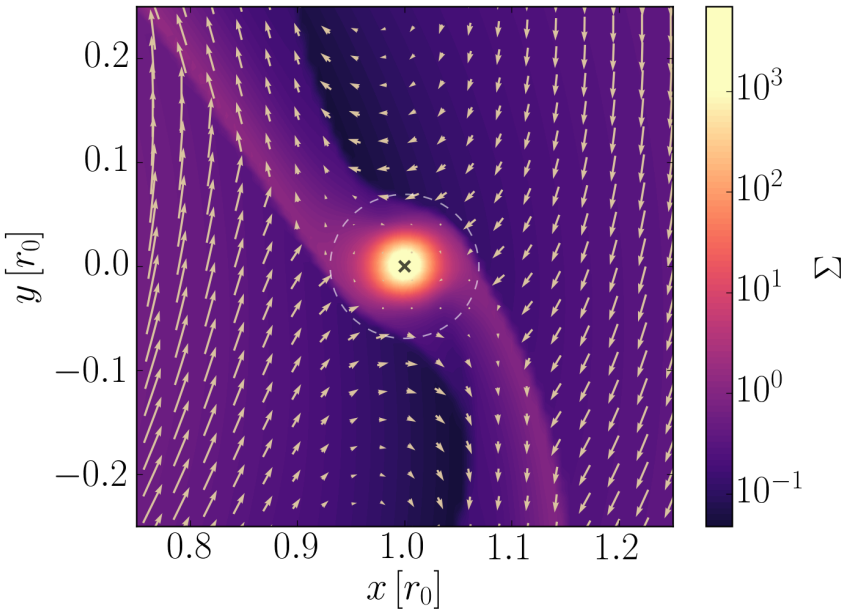

Figure 2.5: Velocity field in the frame co-rotating with the binary, overlaid on the surface density contour. Low relative velocities around the secondary BH indicate the build-up of a quasi-stationary atmosphere, rather than a near-Keplerian mini-disk.

since it would steal gas that would otherwise flow to the inner disk. We leave an investigation of the dependence of the torques on the accretion rate in the $q \neq 1$, GW-driven case to future work.

2.5 Detectability of gas imprint by LISA

2.5.1 Drift in the accumulated GW phase

In this section, we estimate the deviation from the vacuum GW signal caused by the gas disk torques, and assess its detectability by LISA.

The total accumulated phase of a gravitational wave event can be obtained by integrating over the total frequency evolution

$$\phi_{\rm tot} = \int_{t_0}^{t_0+t_{\rm obs}} \dot{\phi}_{\rm GW}\,{\rm dt} = 2\pi \int_{t(f_{\rm min})}^{t(f_{\rm max})} f_{\rm GW}\,{\rm dt} \tag{2.14}$$

where t_0 is an arbitrary reference time when the LISA observation begins, $t_{\rm obs}$ is the total observation time, $f_{\rm min}$ and $f_{\rm max}$ bracket the corresponding observed frequency range, $f_{\rm GW}(t) = \Omega(t)/\pi$ is the GW frequency, which is twice the binary's orbital frequency $\Omega(t)$, and $\phi_{\rm GW}$ is in radians. Assuming the orbit remains circular throughout the inspiral, changing the integration variable to orbital separation r gives

$$\phi_{\rm tot} = -2\pi \int_{r_{\rm min}}^{r_{\rm max}} \frac{f_{\rm GW}}{\dot{r}}\,{\rm dr}, \tag{2.15}$$

where $\dot{r}$ is the (negative) radial inspiral velocity corresponding to the angular momentum evolution of the binary. In our case, both GW emission and gas torques change the angular

momentum, so the net evolution can be described by the sum of both components

$$\dot{r} = \dot{r}_{\rm GW} + \dot{r}_{\rm gas}, \tag{2.16}$$

and the accumulated phase is given by

$$\phi_{\rm tot} = -2\pi \int_{r_{\rm min}}^{r_{\rm max}} \frac{f_{\rm GW}}{\dot{r}_{\rm GW} + \dot{r}_{\rm gas}}\, {\rm dr}. \tag{2.17}$$

Because the effect of gas is much smaller than GWs ($\dot{r}_{\rm gas} \ll \dot{r}_{\rm GW}$) the difference between the accumulated phase with and without gas, $\delta\phi \equiv \phi_{\rm GW+gas} - \phi_{\rm GW}$, can be simplified as follows:

$$\delta\phi = 2\pi \int_{r_{\rm min}}^{r_{\rm max}} \frac{f_{\rm GW}\, \dot{r}_{\rm gas}}{\dot{r}_{\rm GW}^2} \left[1 + \mathcal{O}\left(\frac{\dot{r}_{\rm gas}}{\dot{r}_{\rm GW}}\right)^2\right] {\rm dr} \tag{2.18}$$

Our simulation provides a direct measurement of $\dot{r}_{\rm gas}(\Sigma_0, r)$. We simplify the gravitational torque with a fit to the numerically measured value from the simulation. The fit for the total torque (adding the components inside and outside of the Hill sphere) has the form

$$T_{\rm fit} = \Sigma_0 (Ar^2 + Br + C) \tag{2.19}$$

with $A = 4.37 \times 10^{-28}\,{\rm cm^2\,s^{-2}}$, $B = -8.16 \times 10^{-16}\,{\rm cm^3\,s^{-2}}$, and $C = 4.19 \times 10^{48}\,{\rm cm^4\,s^{-2}}$, This fitting formula is shown together with the numerically measured torques in Fig. 2.3. For $r < 6r_{\rm S}$, the spike at the end of the simulation is likely numerical, so in the range $3r_{\rm S} \leq r \leq 6r_{\rm S}$, we set the torque to remain a constant (we assume $3r_{\rm S}$ represents the end of the inspiral phase).

Using this fit for the total gas torque in equation (2.18) with the relation $\dot{r}_{\rm gas} = 2\dot{\ell}_{\rm gas} r^{1/2} (GM)^{-1/2}$ (where $\dot{\ell}_{\rm gas} = T_{\rm gas}/M_2$ is the rate of change of the secondary's specific angular momentum),

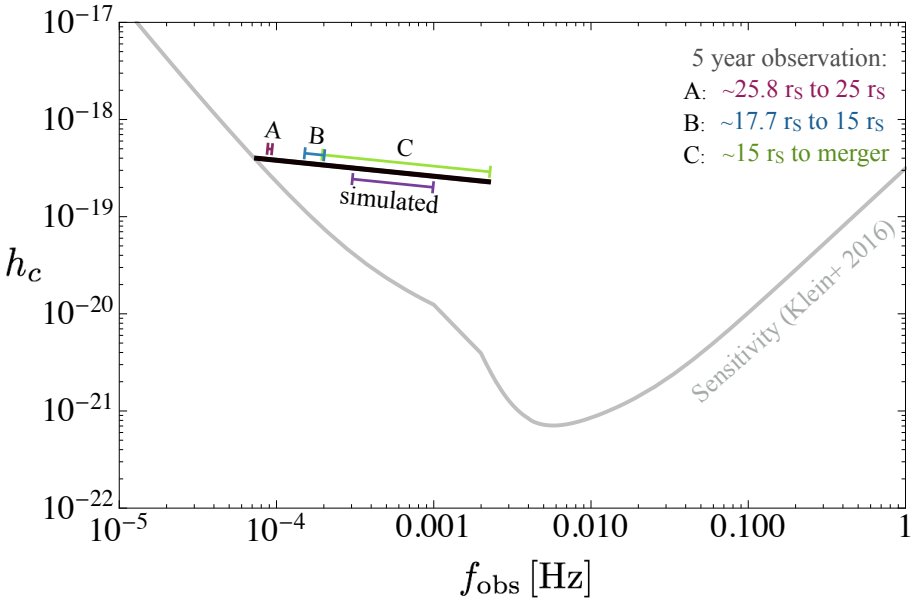

Figure 2.6: The characteristic strain amplitude of the binary inspiral, for an $M_1 = 10^6 M_\odot$, $M_2 = 10^3 M_\odot$ IMRI at redshift $z = 1$, as a function of the observed GW frequency. The top bracketed regions delineate three different 5–year observation windows as labeled, and the bottom bracket highlights the portion we cover in our simulation ($\sim$0.7yr in the binary rest frame).

we compute the phase drift $\delta\phi$ over an observed frequency window from $f_{\rm min}$ to $f_{\rm max}$. Unless stated otherwise, we use the total gas torque, including the contribution inside the Hill sphere.

2.5.2 Signal to noise ratio of the waveform deviation

To estimate the detectability of deviations from the vacuum inspiral waveform, we compute the signal–to–noise ratio (SNR) of the deviation produced by gas, compared to an event occurring in vacuum. The detectability of the gas-induced phase drift in an event depends on the strength of the torque (and thus linearly on the disk mass) as well as the frequency

range of the LISA observation, since this determines the loudness of the event (the strain amplitude h), the number of observed orbits during which the phase drift can accumulate, and the instrumental noise.

The sky- and polarization-averaged GW strain amplitude of a source at comoving coordinate distance $r(z)$ is

$$h = \frac{8\pi^{2/3}}{10^{1/2}} \frac{G^{5/3}\mathcal{M}_c^{5/3}}{c^4 r(z)} f_r^{2/3}, \tag{2.20}$$

where $\mathcal{M}_c = M_1^{3/5} M_2^{3/5}/(M_1+M_2)^{1/5}$ is the chirp mass and $f_r = f(1+z)$ is the rest-frame GW frequency (e.g. Sesana et al. 2005).

The *characteristic* strain h_c of a periodic source takes into account the total observation time τ (i.e. the LISA mission lifetime) as well as the characteristic number of cycles the source spends in each frequency band, $n \equiv f^2/\dot{f}$. For illustrative purposes, in Fig. 2.6 we plot the characteristic strain of an IMRI with our chosen mass ratio $q = 10^{-3}$, primary mass $M_1 = 10^6 M_\odot$ and redshift $z = 1$. The top bracketed regions highlight the evolution of the binary during three different possible 5-year long observational periods. The bottom bracketed portion delineates the evolutionary track we cover in our simulation, which corresponds to ~ 0.7 years. The torques outside this regime are extrapolated using the fitting formula (eq. 2.19).

Following Kocsis et al. (2011), the phase drift $\delta\phi$ can be expressed by the strain *deviation* $\delta\tilde{h}$ in Fourier space. If the Fourier amplitude strain of a vacuum waveform is $\tilde{h}$, the difference in strain due to the phase drift is given by

$$\delta\tilde{h} = \tilde{h}(1 - e^{i\delta\phi}), \tag{2.21}$$

assuming the gas-impacted and vacuum waveforms differ only in phase. The SNR of the

deviation $\delta\rho$ can be computed in Fourier space as

$$(\delta\rho)^2 = 2 \times 4 \int_{f_{\rm min}}^{f_{\rm max}} df \frac{|\delta\tilde{h}(f)|^2}{S_n^2(f) f^2}, \tag{2.22}$$

where $S_n(f)$ is the LISA sensitivity per frequency bin taken from Klein et al. (2016). The factor of 4 comes from the normalization of the one-sided spectral noise density, and the extra factor of 2 arises from the currently proposed configuration of LISA having 6 links, or effectively two interferometers. Similarly, the total SNR of the event is

$$\rho^2 = 2 \times 4 \int_{f_{\rm min}}^{f_{\rm max}} df \frac{|\tilde{h}(f)|^2}{S_n^2(f) f^2}, \tag{2.23}$$

The total inspiral for this particular binary takes ~ 100 years after the strain enters the LISA frequency band (at $f_{\rm min} \sim 10^{-4}$Hz), so the total SNR depends on what separation the binary is at (or what GW frequency the binary is emitting) when the LISA observation begins. The top panel in Fig. 2.7 shows the SNR of the gas-induced deviation as a function of the disk surface density Σ_0 and the phase drift $\delta\phi$ for three different 5–year observed frequency windows. Vertical lines in the figure mark the two estimates of the surface density for near-Eddington accretion disks (Eqs. 2.11 and 2.12). Initially the SNR scales linearly with surface density, before it saturates around a particular value once $\delta\phi \approx 2\pi$.

The bottom panel of Fig. 2.7 shows the ratio of the SNR of the deviation compared to that of the total event, $\delta\rho/\rho$. By dividing out the total SNR, this quantity isolates the impact of the gas. For the case where the SNR of the deviation is highest (the green curve in Fig. 2.7), the SNR never reaches a saturated value because as the binary chirps towards merger, the change in the GW frequency results in a considerable contribution to $(\delta\rho)^2$ from a broad range of higher frequencies. While the influence of gas is comparatively stronger than GWs during the earlier stages of the inspiral, the detectability is less likely because a

smaller frequency range results in a weaker SNR.

The SNR of the deviation (top panel in Fig. 2.7) is directly relevant to the detectability, and is dependent both on the strength of the deviations introduced by the gas, as well as on the total SNR of the event. While gas effects are stronger in the earlier stages of the inspiral, the overall SNR obtained by observing these stages (regardless of any phase change) is relatively low. If LISA catches the binary 5 years prior to merger, however, where its initial rest-frame separation is $r_{\rm min} \sim 10 r_{\rm S}$, it will accumulate a significant amount of SNR as the binary chirps to merger, largely because the LISA noise is much lower towards higher frequencies (see Fig. 2.6). Thus for this particular binary, the deviation is most detectable in the final five years of the inspiral. This would not necessarily be the case, however, for lower-mass primary BHs, or lower-redshift events, which would chirp past the minimum of the noise curve. Adopting the criterion of detectability $\delta\rho \geq 10$, we find that the gas imprint is detectable for our fiducial binary if the BH is embedded in gas with surface density $\Sigma_0 \gtrsim 10^3\,{\rm g\,cm^{-2}}$.

2.6 Discussion and caveats

In the present work we find that, depending on the AGN disk mass, LISA can detect the migration imprint on gas-embedded IMRIs in the final 5 years of the inspiral. With our current understanding of AGN, the typical density of accretion disks is uncertain, and theoretical estimates range from $\Sigma \sim 10^1 - 10^8\,{\rm g\,cm^{-2}}$ in the regions of interest ($\lesssim 30 r_{\rm S}$). We find that the deviation is detectable (SNR ¿ 10) if the secondary BH is embedded in a disk with a surface density $\Sigma \gtrsim 10^3\,{\rm gcm^{-2}}$. This density is reasonably reached in models of near-Eddington accretion disks; in particular it is exceeded in so-called β-disks. In our fiducial α-disk model, the torques are too weak to detect.

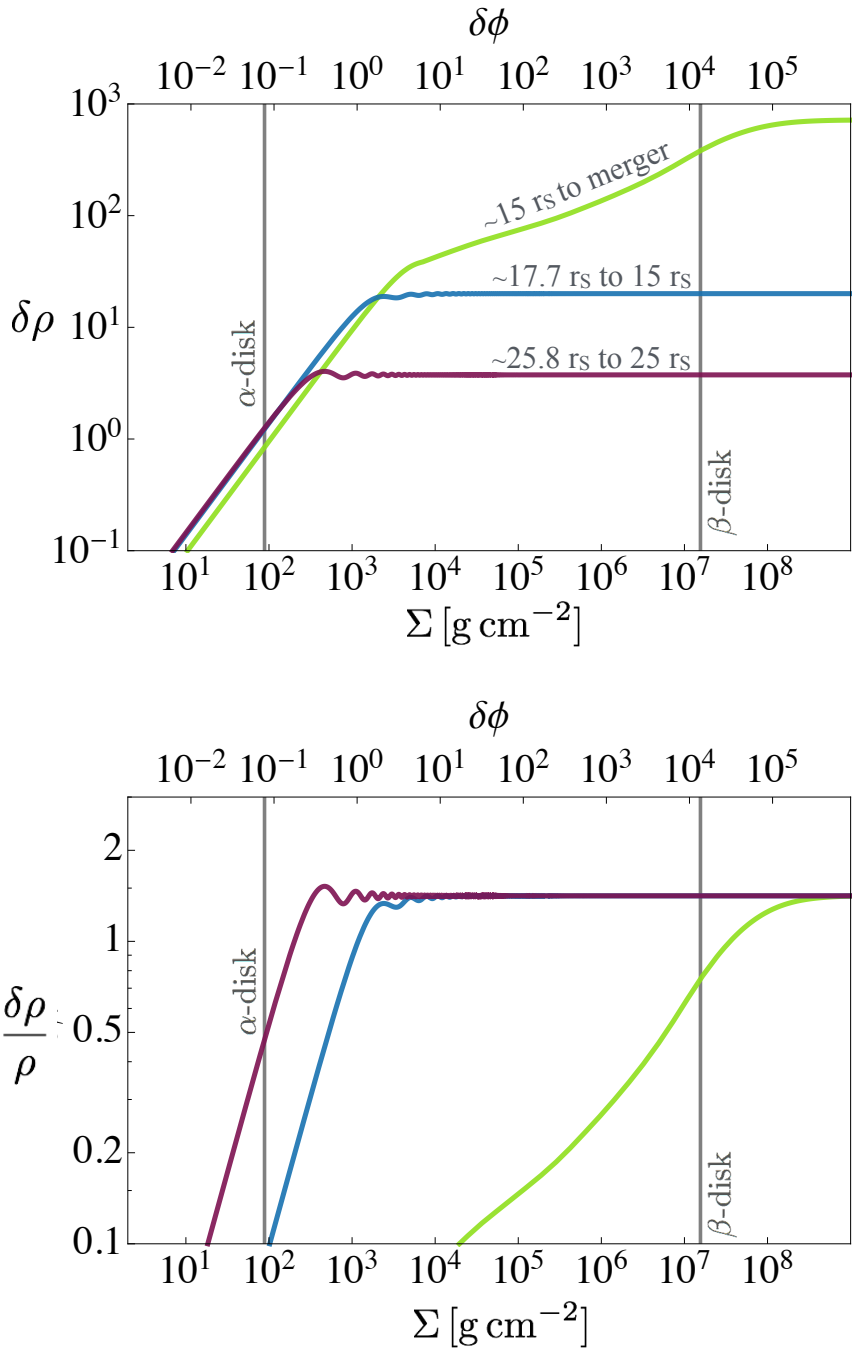

Figure 2.7: The top panel shows the SNR of the gas-induced deviation ($\delta\rho$; eq. 2.22) in the LISA waveform as a function of disk density, for different 5–year observation windows, and with our fiducial parameters $M = 10^6 M_\odot$, $q = 10^{-3}$, and $z = 1$. The lines are labeled with the binary's rest-frame separation during each LISA observation. The top axis shows the corresponding total accumulated phase drift for each surface density, for the (ideal) case of observing the final 5 years to merger (green line). The lower panel shows the relative SNR: the SNR of the deviation in units of the total SNR of the event ($\delta\rho/\rho$; with ρ from eq. 2.23).

The difference between Σ in these models lies in the physical mechanism providing the viscosity and its dependence on radiation pressure, an area of active research in accretion disk dynamics (see Blaes et al. 2011; Jiang et al. 2013). The viscosity in β-disks, in particular, is assumed not to rise with radiation pressure. As a result, it is much lower than in the α-disks, resulting in a much higher disk surface density at a fixed accretion rate. If the signatures of a gas-embedded IMRI are detected by LISA, then it should be possible to extract information about the underlying disk, as even a measurement of a total accumulated phase shift will provide (at the least) a lower limit on the disk density. If both the amplitude and frequency-dependence of the deviation in the GW signal are well measured, this will directly probe the density, and we expect other disk parameters to be constrained as well (e.g. density gradient, temperature, viscosity) provided the frequency-dependence amongst these parameters is well understood and not degenerate. Our basic conclusion is that *LISA will have to opportunity to probe disk migration physics via gravitational waves.*

We find that the effect of migration torques is stronger during the earlier stages of the inspiral, but its detectability is highest at higher frequencies, where LISA is most sensitive, and the system is chirping rapidly. For our fiducial binary ($M_1 = 10^6 M_\odot$, $q = 10^{-3}$, $z = 1$), the gas-induced deviation is most detectable during the final years of the inspiral, as this is when LISA accumulates most of the total SNR for the event. This feature is characteristic of the particular (redshifted) chirp mass, for which the last several cycles of the coalescence occur at frequencies near the minimum of the LISA sensitivity curve (see Fig. 2.6). For IMRIs with a higher chirp mass the merger will occur more quickly, the characteristic frequency is shifted to lower values, and we expect the contribution to the SNR from the final stages to be lower. The same may be true for lower chirp masses, which shift the final few cycles to higher frequencies past the minimum of the LISA noise curve. We plan to explore the range of detectability over various system parameters in future work.

It is worth noting that the torques depend on both disk physics and the accretion efficiency of the secondary BH. In particular, simulations of equal–mass binaries find that the build–up of gas within and near the Hill sphere, and therefore the net torque, scales with viscosity (Tang et al. 2017). To assess the sensitivity in our case, we re-run our fiducial calculation, except we reduced the viscosity by a factor of three. The evolution of the gas torques in both cases are compared in Fig. 2.8. We normalize the torques by the conventional Type I torque from Tanaka et al. (2002) provided by $T_0 = \Sigma r^4 \Omega^2 q^2 \mathcal{M}^2$, which does not depend on viscosity and thus allows for a direct comparison. As this figure shows, in the new run with $\alpha = 0.01$, the Hill sphere torque is 3 times weaker than in the $\alpha = 0.03$ case. On the other hand, the torques from outside the Hill sphere remain similar, and they tend to converge to the same value by the end of the inspiral. This suggests that the increase in the sink timescale (eq. 2.3) caused by the smaller α, is more important than the change in the dynamics due to the reduced viscosity in the bulk of the simulation, although we note that the reduced bulk viscosity may also play a role in reducing the gas flow around the secondary BH. We plan to further explore the sensitivity to α and to other parameters in future work.

We also note that in all cases, the migration torque exerted by the gas outside the Hill sphere is much weaker (by approximately an order of magnitude) than the torques from inside, and they also have the opposite sign (resulting in inward migration). Thus if the torques from inside the Hill sphere were excluded, the phase drift would be negative, corresponding to a slight increase in the inspiral rate, and the detectability would require an order of magnitude higher disk surface density.

Our detectability estimates are obtained for an intermediate mass ratio binary. For binaries with a more extreme mass-ratio, we expect that the gas effects would be more easily observable. First, a lower mass-ratio binary emits weaker GWs: the GW inspiral time is

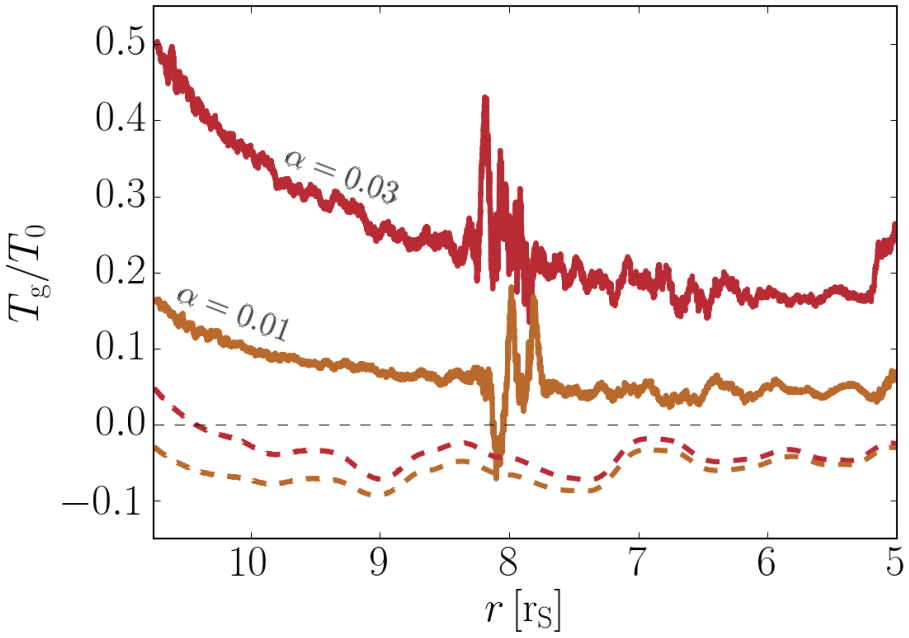

Figure 2.8: Torques exerted on the secondary BH from gas within the Hill sphere (solid curves) and outside the Hill sphere (dashed curves), for two runs with different viscosity parameter α as labeled. The torque from gas inside the Hill sphere is highly sensitive to the viscosity.

proportional to q^{-1} (at fixed total mass and binary separation measured in gravitational radii). The total number of cycles observed during the fixed LISA observation time scales with chirp mass as $\propto \mathcal{M}_c^{-5/8}$, yielding more cycles over which the phase drift can be measured for lower-mass companions. On the other hand, the scaling of the disk torques with mass ratio in the GW-driven regime is unknown and must be computed in future work. We note here only the following: If the gas-induced migration time-scale followed the viscous time, it would be independent of the secondary's mass M_2. However, migration may be slower than the viscous timescale by a factor that depends on the ratio of the secondary and disk mass, $M_2/M_{\rm disk}$. In the self-similar models employed in Haiman et al. (2009), the migration timescale is proportional to $q^{-3/8}$, although simulations by Duffell et al. (2014) demonstrate that this dependency may be more complex. Finally, as the mass ratio decreases and the secondary BH no longer carves a gap, it will enter the Type I regime, in which the torque (provided by T_0) scales differently with mass ratio and disk parameters. As a comparison, if the secondary BH was instead a $10M_\odot$ BH (which for the disk parameters we adopt in this work, puts the BH in the Type I regime, see Duffell 2015a) then the torque estimated by T_0 is ~ 3 orders of magnitude weaker than the torque exerted on our more massive, gap-opening secondary. However, it is currently unclear how the torque changes with migration rate in this migration regime. Additionally, while IMRIs will characteristically have higher SNR, the current capabilities of numerical relativity are computationally limited for calculating waveforms for intermediate mass ratio systems (Mandel & Gair 2009a). Accurate waveforms will be crucial for extracting the system parameters and for detecting a gas-induced phase drift.

An important question to consider is whether the impact of gas may be degenerate with system parameters (such as chirp mass, inclination, eccentricity, spin, etc.) or with other environmental effects, such as dynamical friction from dark matter (Barausse et al. 2015c).

In principle, gas torques can also be degenerate with modifications to general relativity, although this effect would then be present in all E/IMRIs, while gas would have a variable effect from source to source. An exploration of the parameter space is beyond the scope of the present paper, and we leave it to future work. However, we note that the frequency dependence of the gas torque is generally different from that of the system parameters. At least for high SNR measurements for a source that chirps over a broad frequency band, and for which the frequency-dependence can be measured, we expect that the gas effects can be disentangled from system parameter variations (see discussion in Yunes et al. 2011).

We focus primarily on migration torques, but accretion disks can produce other interesting effects on BH inspirals that we neglect in the present study, including mass, spin, and eccentricity evolution. Efficient accretion can lead to a non-negligible increase in mass of the secondary BH throughout the inspiral, which will affect the GW frequency evolution (accretion onto the primary SMBH is negligible, as the increase in mass throughout the LISA lifetime is under the accuracy limit). The possibility exists for accretion to drive up the spins of the BHs (e.g. Teyssandier & Ogilvie 2017), an effect which we neglect here, and it may also act to align the spins of both BHs, particularly if the BHs form in the accretion disk (Bogdanović et al. 2007). While we do not model the spin of the BHs in this paper, we hypothesize that significant spin-up of the secondary is unlikely (at least for the prograde case we simulated here), because the relative angular momentum of the gas near the BH is low. This is shown in the velocity map in Fig. 2.5, where the gas around the BH exhibits properties more akin to an atmosphere than to a mini-disk.

Gas also provides the possibility for EM counterparts to the GW detection. If an associated EM signature is detected, it would confirm the presence of gas around the source. In this case, even a non-detection of a GW phase deviation for an EM-identified IMRI would teach us about the environment by putting a limit on the density and/or viscosity of the

disk.

Simulations of intermediate-mass planets show that a disk may drive periodic eccentricity oscillations in the planet's orbit that are low but not negligible, with the eccentricity ranging from 0.01 to 0.1 (Ragusa et al. 2018, see also Papaloizou et al. 2001; Bitsch et al. 2013) although this depends on both the disk mass and the perturber mass (Dunhill et al. 2013). We expect that gas-embedded E/IMRIs will be close to circular compared to events originating from stellar remnants in galactic nuclei, which will have significantly higher eccentricities. Thus spin-aligned and near-circular events will be indicative of a gas disk.

In future work, we intend to relax several assumptions made in this study, as well as explore a range of values for the key parameters. In this paper we assumed a locally isothermal equation of state. This assumption should be relaxed by incorporating a more sophisticated treatment of the thermodynamics, allowing the gas to heat due to local shocks and viscous dissipation, and to cool through its surface (e.g. Farris et al. 2015b). It is also known that the α-prescription is a poor approximation in parts of the disk where the flow is not laminar, an issue that can be addressed using magneto-hydrodynamics simulations (e.g. Shi et al. 2012). As already mentioned above, a near-Eddington circumbinary accretion disk around a BH in the LISA band is likely to be supported by radiation pressure, which will need to be included in future simulations. Finally, our simulations in this study are in 2D. We expect that the 3D vertical structure will modify the structure of the gap and the accretion streams, as well as the gas distribution near the secondary BH, and will inevitably have a strong affect on the gas torques.

We also expect that the migration torques depend on disk parameters (such as α and $\mathcal{M}$), the density and temperature profiles of the disk, the BH mass ratio, any orbital eccentricity, and also the GW-driven orbital decay rate. Indeed, even for non-migrating planets, Duffell (2015b) find that disk torques are sensitive to combinations of these parameters, particularly

in the intermediate mass-ratio regime.

Despite its limitations, our present study suggests that the impact of circumbinary gas may be measurable in the LISA waveform of an E/IMRI event and warrants further investigation. We intend to address the outstanding issues in future work.

2.7 Conclusions

In this paper, we study the gas torques exerted on a gravitational wave driven inspiral with high resolution 2D hydrodynamic simulations of a 10^{-3} mass ratio binary in an isothermal viscous disk. Motivated by the prospect of LISA detecting the late stages of intermediate mass ratio inspirals, we apply the results of our simulations to estimate the detectability of gas torques on a $10^6 M_\odot + 10^3 M_\odot$ binary merger occurring at a redshift $z = 1$.

We find that the net disk torque differs from previous semi-analytic estimates, which were based on the viscous torque for a non-migrating secondary. While these previous torque estimates were negative, we here find that the total torque is positive, resulting in a slow-down of the inspiral, and its strength is only fraction $(1\% - 5\%)$ of the viscous torque. While it is $4 - 5$ orders of magnitude weaker than the torque due to GW emission, it can still produce a detectable phase drift in the GW waveform. For our fiducial estimate of the accretion rate, the accretion torque is at least $10 - 11$ orders of magnitude weaker than that due to GWs and does not contribute significantly to the gas imprint in the waveform.

An analysis of the origin of the torques shows that gas very close to the secondary BH (inside its Hill sphere) exhibits a front-to-back asymmetry with respective to the direction of the secondary's motion, and leads to the positive (outward) component of the torque, whereas gas elsewhere in the disk exerts a weaker negative torque. More sophisticated simulations that resolve the 3-dimensional gas morphology and velocity of gas near the secondary BH

could provide insight into whether and how this asymmetry occurs.

For the IMRI we consider here, the deviation in the GW waveform is detectable (with a signal to noise ratio > 10) if the system is embedded in a disk with a surface density $\Sigma_0 \gtrsim 10^3\,\mathrm{g\,cm^{-2}}$. This density may be exceeded in cold, thin, near-Eddington disks expected in active galactic nuclei. Gas-induced deviations are strongest during the earlier stages of the inspiral, but they are more detectable for binaries at higher frequencies, where LISA's sensitivity is stronger and the binary is chirping significantly. We expect the gas disk-induced phase drift in the GW waveform to be sensitive to disk properties, which implies that the detection of a gas-embedded inspiral will provide the opportunity for LISA to probe the physics of AGN disks and migration torques.

Chapter 3

Simulations of gas-embedded intermediate mass ratio inspirals in the LISA band

3.1 Introduction

In Chapter 2 we have shown that torques exerted by gas can influence the coalescence of an IMRI, but that the direction, strength, and temporal evolution of the torques is difficult to predict. With a simulation that resolves the gas disk response to an embedded $q = 10^{-3}$ IMRI for several thousand orbits, we found that torques can slow down, rather than speed up, the inspiral, due to a critical contribution to the torque that comes from asymmetry within the BH's Hill sphere. Applying the measured torques to a fiducial binary with $M = 10^6 M_\odot$ at $z = 1$, we estimate that the resultant deviation in the GW waveform, that arises as a shift in the accumulated phase, is detectable if the IMRI resides in a disk with surface densities

This section contains work completed in collaboration with the following authors: Derdzinski, A.; D'Orazio, D.; Duffell, P.; Haiman, Z.; Macfadyen, A.

above $\Sigma_0 \gtrsim 10^{3-4}\mathrm{g\,cm^{-2}}$ (Derdzinski et al. 2019).

This proof of concept was demonstrated for a single set of system and disk parameters: a binary mass ratio $q = 10^{-3}$ a viscosity parameter $\alpha = 0.03$ and Mach number $\mathcal{M} = 20$. In reality, whether or not the torques accelerate or hinder the inspiral, and whether the resultant phase drift is detectable, is dependent on the combination of these parameters. As we have seen in similar works for planet migration in protoplanetary disks, even small changes in the satellite mass or disk properties can affect the evolution of the system (Baruteau & Masset 2013; Duffell 2015b). This challenge is present not just for small mass ratio systems, but even more equal mass MBH binaries, where recent simulations show that torques can either help merge the binary or stall it (Duffell et al. 2019a; Muñoz et al. 2018). The current standing is that the disk response to an embedded perturber, especially in the co-orbital region of the satellite, is sensitive to disk parameters and the equation of state, and the resulting migration torque is hard to predict (e.g., Duffell et al. 2014; Duffell 2015b; Paardekooper & Mellema 2006) Moreover, it has not yet been fully explored how the torques in all regimes may change when the perturber is moving, particularly at a rate dictated by GW emission.

In the current Chapter, we expand upon the results presented in Chapter 3. We explore the gas response, resulting torque, and its temporal evolution with an expanding suite of simulations that explore changes in binary parameters (namely q and inspiral rate $\dot{r}/r$) and disk parameters (viscosity α and Mach number $\mathcal{M}$). We push the simulations to faster inspiral rates (approaching the ISCO of a $q = 10^{-3}$ inspiral), in an attempt to fully isolate the effect of migration on the torque and how its evolution may vary for different systems. We expect, as informed by similar studies, that the torques exerted on the embedded satellite will be some fraction of the viscous rate (e.g., Edgar 2007) (which, as we will show, is much weaker than GWs), but that the scaling of torques with disk parameters may be unpredictable.

Changing the mass ratio of a binary will affect not only the gas dynamics and resulting

torque, but also the GW evolution and overall detectability of the event by LISA. We revisit the question of detectability with these new findings, estimating the potential for detecting gas imprints and how this changes with q, binary mass, and evolutionary stage of the binary. We take our measured torques and, as in Chapter 2, extrapolate them to solutions of the total torque during the final coalescence of a physical IMRI. We show that the direction and evolution of the torque, and its ultimate detectability, will depend on the mass ratio of the binary and at what evolutionary stage we observe it.

As further motivation, semi-analytical estimates of in-situ star formation suggest that the accretion of compact objects may contribute substantially to the growth of MBHs (Dittmann & Miller 2019), in which case gas-embedded inspirals may be more common than initially anticipated. This work is motivated by the idea that, provided we understand how gas torques impact a GW inspiral, gravitational waves can be used as a valuable tool for providing measurements of AGN disk density and perhaps improve our understanding of migration.

This Chapter is presented as follows: In Section 3.2 we summarize our numerical approach, including the hydrodynamical simulations and the range of simulated parameters. Section 3.3 presents our simulation results, analyzing the torques over all parameters. In Section 3.4, we apply our results to a fiducial set of LISA binaries, calculating the detectability of gas imprints via deviations in the waveform. After a discussion in Section 3.6, we list our conclusions in Section 3.7.

3.2 Simulation Setup

We use the moving-mesh hydrodynamics grid code DISCO (Duffell 2016) to model a 2-dimensional, viscous disk with an embedded migrating BH. In this section we describe our scale-free numerical approach, the prescribed orbit of the migrator, as well as how we measure

the torques.

3.2.1 Disk model

The simulation setup is the same as in Chapter 2, with slight modifications to the domain size and resolution. Our simulations model a vertically-integrated, Keplerian disk, parameterized by a constant aspect ratio $h/r = \mathcal{M}^{-1}$, where h is the disk scale height, r is the distance to the central MBH, and $\mathcal{M}$ is the Mach number. The sound speed varies as $c_s = v_\phi/\mathcal{M}$, where $v_\phi = \sqrt{GM_1/r}$ is the Keplerian orbital velocity around a central BH of mass M_1. We adopt an α-law prescription for the viscosity, with the kinematic viscosity set by $\nu(r) = \alpha c_s(r)h(r)$. The disk is locally isothermal, with the pressure solved by $p = c_s\Sigma(r)$, with $\Sigma(r)$ being the vertically-integrated surface density profile. Under the above constraints the initial condition for the density profile becomes:

$$\Sigma(r) = \Sigma_0 \left(\frac{r}{r_0}\right)^{-1/2}, \tag{3.1}$$

where r_0 is an arbitrary distance unit, and Σ_0 is a surface density normalization.

The simulation boundary extends from $0.5 < r/r_0 < 6.0$, with a logarithmically-spaced grid of 666 radial cells (to maintain the resolution of simulations in Chaper 2). A resolution test confirms that torques do not change with higher resolution. However, a test of the inner and outer boundaries proved to be very important. Compared to Chapter 2, we more than double the simulation outer boundary after finding that for larger satellites, a too-close boundary will lead to numerical transients in the torque that last for several viscous times. Overall the simulation boundaries must be considered carefully, as the location can affect the magnitude of the torque on a satellite and also produce numerical transients that affect the torque even if the disk reaches a 'viscous steady state'. We test that our simulations

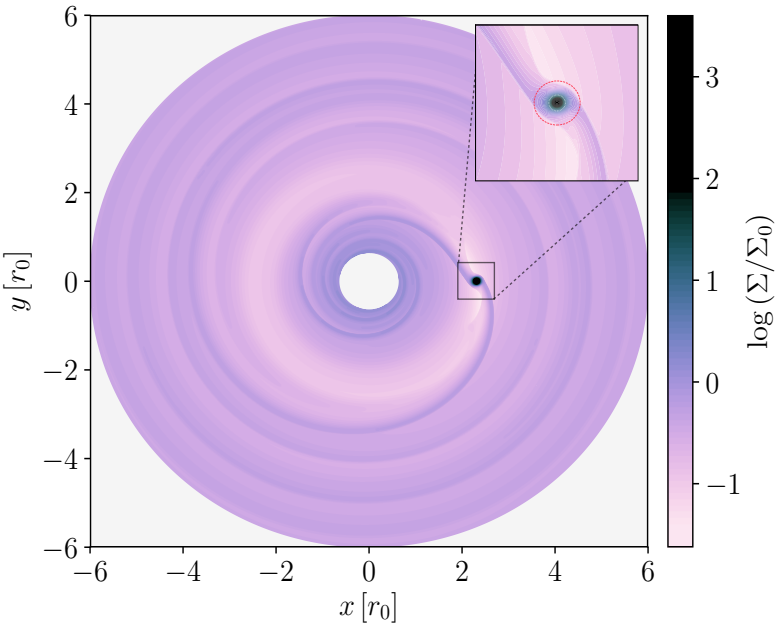

Figure 3.1: Snapshot of surface density during one of our simulations with $q = 10^{-3}$, $\alpha = 0.03$, and $\mathcal{M} = 20$. A migrating, embedded perturber excites spiral density waves and carves a shallow gap. Zoom-in panel shows a close-up of streams flowing across the BH Hill radius.

are converged with resolution and boundary location, but take caution when analyzing the exact torque value and small scale fluctuations.

To visualize our simulation we show a snapshot of the 2D surface density in Fig. 3.1.

3.2.2 The inspiralling BH

The primary BH is excised from the simulation domain, and the secondary BH is modeled as a point mass with a smoothed gravitational potential, defined by

$$\Phi_2 = \frac{GM_2}{({r_2}^2 + \epsilon^2)^{1/2}}, \tag{3.2}$$

where r_2 is the distance to the secondary BH and ϵ is the smoothing length, which we set to half a scale height $\epsilon = h(r)/2$ at the secondary's radius. As the BH migrates to smaller separations due to GWs, the smoothing length is updated accordingly.

Following the quadrupole equation for a GW inspiral (the Peters formula, Peters 1964), the BH is placed in a quasi-circular, prograde orbit whose separation evolves according to

$$r = r_f(1 - 4R(t - t_{\rm f}))^{1/4}, \tag{3.3}$$

where $R = \dot{r}/r$ is the migration rate defined at the final separation r_f. For all simulations, the BH ends at $r_f/r_0 = 1$ at a final time t_f. For a circular gravitational wave inspiral, the migration rate is defined as

$$R = -\frac{64}{5}\frac{G^3}{c^5}\frac{M^3}{(1+1/q)/(1+q)}\frac{1}{r^4}. \tag{3.4}$$

While the simulation is scale-free, prescribing an inspiral rate with Eq. 3.4 implies a physical length scale r_0 that depends on the mass ratio q and the binary mass M. Now that we are interested in simulating binaries with smaller q, this conversion becomes important.

When referring to the 'migration rate' of the BH it is natural to state the inspiral rate in units of the orbital time, as

$$\frac{\dot{r}}{\Omega r} = \frac{64}{20\sqrt{2}}\frac{1}{(1+1/q)(1+q)}\left(\frac{r_{\rm S}(M_1)}{r}\right)^{5/2}, \tag{3.5}$$

where $r_{\rm S} = 2GM_1/c^2$ is the Schwarzschild radius around the primary MBH. This gives us a dimensionless migration rate factor, given by the gravitational wave inspiral timescale R in units of the dynamical timescale Ω.

Each of our simulations covers 5,000 orbits of the BH, and we cover a fixed range of

migration rates, specifically from $7 \times 10^{-5} \leq \dot{r}/\Omega r \leq 2 \times 10^{-4}$. For each q this corresponds to a physical binary separation. This conversion is depicted in Figure 3.2, where we highlight regions we simulate for each mass ratio. Our fiducial system is a $q = 10^{-3}$ binary coalescing to merger in the LISA band, from $10r_{\rm S}$ to $r_{\rm ISCO} = 3r_{\rm S}$, where $r_{\rm ISCO}$ corresponds to the last stable circular orbit around a non-spinning BH. (Note that this is similar to the system in Chaper 2, except that the current setup probes faster migration rates.) We run all our simulations over this range of migration rates, keeping in mind that when decreasing q, we are in fact modeling a smaller physical binary separation. When scaled to physical units, our lower mass ratio simulations reach separations inside the ISCO. While such inspiral rates are not physical for these binaries, this approach allows us to isolate the effect of migration on the torque, changing one parameter at a time, since torques are also sensitive to mass ratio.

To simulate the entire inspiral with one simulation requires having the BH start at a large separation that can be dangerously close to the outer boundary. For this reason, each set of system parameters is covered with two simulations that correspond to different stages of the inspiral, each spanning the same total number of orbits. First a 'slow' simulation (comparable to Chapter 2) corresponds to a $q = 10^{-3}$ gravitational-driven inspiral from $10r_{\rm S}$ to $6.5r_{\rm S}$, spanning 5,000 orbits of the binary. After finding that torques are relatively well behaved in this regime, we run 'fast' simulations that probe separations from $8r_{\rm S}$ to $3r_{\rm S}$, or the final 5,000 orbits of a $q = 10^{-3}$ IMRI. The overlap between these simulations, shown as the dashed overlapping lines in Fig. 3.2, ensures that our solution for the torque as a function of migration rate is physical, and not from other factors such as disk settling or boundary effects.

Each simulation runs for well over a viscous time of the disk. For reference, this can be

defined as a function of orbital time $t_{\rm orb}$ at the BH position as

$$t_{\rm visc} = \frac{2}{3}\frac{r^2}{\nu} \approx 1415 \left(\frac{\mathcal{M}}{20}\right)^2 \left(\frac{\alpha}{0.03}\right)^{-1} \mathrm{t_{orb}}. \tag{3.6}$$

We neglect relativistic effects and keep the potential Newtonian, despite the fact that we are simulating regions close to the ISCO where relativistic effects will undeniably affect the dynamics. This primarily to maintain the simplicity and scale-free nature of the simulation.

We calculate the torques exerted by the gas, but we neglect them during the BH's orbital evolution, effectively disregarding the gravitational influence of the gas on the BH. This assumption is justified in the regime where the disk mass is insignificant compared to the mass of the BHs, and when the torque due to GW emission is far dominant. We demonstrate both of these results to be true in Section 3.3. This approach keeps the equations scale invariant and Σ_0 arbitrary, and keeps our computation less expensive, allowing us to run a full parameter study.

3.2.3 Sink prescription

Accretion onto the secondary is implemented with the same approach as in Chapter 2, in which the gas inside the smoothing radius ϵ is approximated as a mini-disk with the same α and $\mathcal{M}$ as the global disk. The surface density within a distance ϵ of M_2 is decreased on the viscous timescale, $t_{\rm visc}(\epsilon)$ at a rate

$$\frac{d\Sigma}{dt} = -\frac{\Sigma}{t_{\rm visc}(\epsilon)} \exp -(r_2/\epsilon)^4. \tag{3.7}$$

This timescale, when converted to orbital times of the BH, corresponds to a very 'slow' accretion timescale. We demonstrate the importance of this assumption in Section 3.3.1,

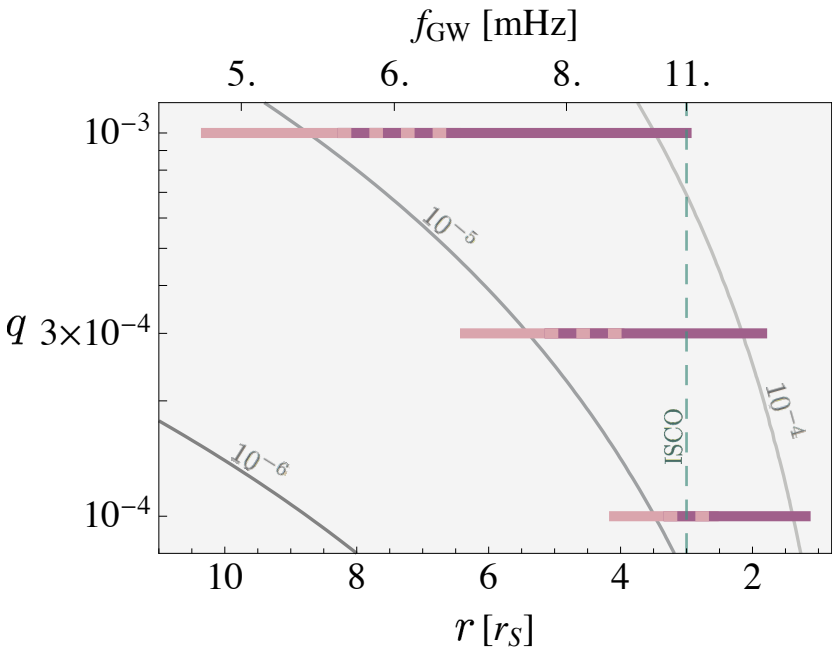

Figure 3.2: Contour lines (in grey) of $\dot{r}/(\Omega r)$, a dimensionless migration rate factor, as a function of q and binary separation r (or corresponding gravitational wave frequency $f_{\rm GW}$, given a fiducial primary mass $M_1 = 10^6 M_\odot$). The horizontal colored lines show the migration rate we cover in our simulations, which, for each mass ratio, corresponds to different physical separations in Schwarzschild radii. We choose to simulate all mass ratios over the same range of dimensionless migration rate, so portions of smaller mass ratio simulations correspond to separations inside the ISCO (vertical dashed line).

particularly when $q = 10^{-3}$. Unlike more equal-mass binaries (such as those studied in Duffell et al. 2019b), the sink prescription affects the torque when a gap-opening satellite is sufficiently massive.

3.2.4 Torque measurement

When measuring the torques in the simulation, we use the same formulas introduced in Section 2.4 to compare the torque on the secondary due to GW emission ($T_{\rm GW}$, Eq. 2.7)

to the gravitational torque exerted by the gas ($T_{\rm g}$, Eq. 2.8). We neglect the accretion torque in subsequent calculations after finding that it is negligible for our chosen parameters and accretion prescription. We compare our measured torques to the viscous torque (T_ν, Eq. 2.10). However, when comparing torques on binaries of different mass ratios, it is useful to utilize the Type I formula from Tanaka et al. (2002),

$$T_0 = \Sigma(r) r^4 \Omega^2 q^2 \mathcal{M}^2, \tag{3.8}$$

which, in our disk model, carries the same radial scaling as T_ν. When analyzing torques on a moving BH, normalizing by T_0 scales out any radial dependence of the torque, allowing us to compare between mass ratios and isolate the effect of migration. To analyze various contributions of the gas disk to the total torque, we also compute torque density maps, defined by $\mathcal{T} \equiv \mathbf{g}_\phi \times \mathbf{r}$.

The magnitude of any torque exerted by gas (for $T_{\rm g}$, T_ν, or T_0) will depend linearly on the normalization of the surface density, which is arbitrary in our simulation setup. Rather than choosing a single value for Σ_0, we are given the freedom to ask: at what surface density do gas torques produce a detectable phase drift? Additionally, is this density physically reasonable?

We again define two bracketing estimates of the surface density in the inner regions of thin, near-Eddington accretion disks, this time computing them for our new simulation scaling, where the length scale is now $r_0 = 3r_{\rm S}(M_1)$. Our estimates represent AGN accreting at 10% of the Eddington rate with a radiative efficiency $\epsilon_{\rm eff} = 0.1$. The first estimate is obtained from the seminal model for a thin, viscous accretion disk by Shakura-Sunyaev (i.e.

α-disk; Shakura & Sunyaev 1973) in the radiation-pressure dominated region,

$$\Sigma_\alpha = 41.08 \left(\frac{\alpha}{0.03}\right)^{-1} \left(\frac{\dot{M}}{0.1\dot{M}_{\rm Edd}}\right)^{-1} \left(\frac{r}{3r_{\rm S}}\right)^{3/2} {\rm g\,cm^{-2}}. \tag{3.9}$$

In case the viscosity is proportional only to the gas pressure (i.e. for a so-called β-disk), the surface density at the same accretion rate is much higher. We estimate the surface density in this second model as

$$\Sigma_\beta \;=\; 2.11 \times 10^7 \left(\frac{\alpha}{0.03}\right)^{-4/5} \left(\frac{\dot{M}}{0.1\dot{M}_{\rm Edd}}\right)^{3/5} \times \left(\frac{M}{10^6 M_\odot}\right)^{1/5} \left(\frac{r}{3r_{\rm S}}\right)^{-3/5} {\rm g\,cm^{-2}}. \tag{3.10}$$

While both of these models carry a different density radial scaling than our disk model, the values are meant to provide a reference for possible surface densities, which becomes important for detectability in Section 3.4. Note that in both these estimates, the total disk mass within the BH's orbit is much less than the mass of the BHs. For example, for the high mass estimate, an integral of the total enclosed mass within $10r_{\rm S}$ gives

$$M_{\rm encl} = 2\pi \int_{3r_{\rm S}}^{10r_{\rm S}} \Sigma_\beta r dr \simeq 0.16 M_\odot \tag{3.11}$$

for $\alpha = 0.03$, $M = 10^6 M_\odot$, and $\dot{M} = 0.1\dot{M}_{\rm Edd}$, which is sufficiently negligible compared to the embedded BH's mass of $10^{2-3} M_\odot$.

3.2.5 Simulation suite

We extend our model from Chapter 2 by first expanding on the range of migration rates to more extreme values, and then varying q, $\mathcal{M}$, and α. Our fiducial system is a $q = 10^{-3}$ binary embedded in a disk with $\alpha = 0.03$ and $\mathcal{M} = 20$. We then run simulations for three different mass ratios ($q = [10^{-3}, 3 \times 10^{-4}, 10^{-4}]$), each with two different values of $\alpha = [0.03, 0.1]$. We

also run a range of Mach numbers $\mathcal{M} = [10, 20, 30]$ for our fiducial run. Our simulations are listed in Table 3.1, where each run is labeled with its mass ratio and viscosity (For example, 'q1e3a03' corresponds to a run with $q = 10^{-3}$ and $\alpha = 0.03$.)

For computational feasibility, our study is limited to lower Mach numbers and higher values of α We note that our fiducial choice of $\mathcal{M} = 20$ corresponds to a hotter, thicker disk than expected in thin, near-Eddington AGN discs. However, higher Mach numbers are numerically challenging to simulate. As we show in Section 3.3.1.3, increasing the Mach number to 30 already produces incredibly noisy torques and gas morphology that is difficult to resolve.

3.3 Results

Here we describe results from our simulations, primarily analyzing the torque exerted on the BHs, before deriving estimates of the detectability of the gas imprint in a LISA event.

3.3.1 Gas torques depend on parameters

We expect the torque to have some radial dependence as the secondary moves through the disk, given the initial disk density profile, so when analyzing simulation torques we divide them by T_0 (Eq. 3.8). For a stationary satellite in a steady state disk, this normalized torque should be constant, and any deviation of $T_{\rm g}/T_0$ from a constant is due to the increase in migration rate.

Torques are sensitive to the perturber mass q as well as disk parameters α and $\mathcal{M}$. For all simulations, we find that torques oscillate around some fraction of T_0. As we discuss in the following sections, whether torques are negative (inward) or positive (outward) depends on a combination of q, α, and $\mathcal{M}$, and we find there is no direct or obvious scaling in this

SIMULATIONS

Name	Mass Ratio	Viscosity	Mach	Separation $[r_S]$	Average Torque
	q	α	$\mathcal{M}$	$[r_i, r_f]$	$< T/T_0 >$
q1e3a03 (fiducial)	10^{-3}	0.03	20	$[10.3, 6.5]$ $[8.2, 3.0]$	0.21 see Fig. 3.3
q3e4a03	3×10^{-4}	0.03	20	$[6.4, 4.0]$ $[5.1, 1.9]$	0.01 see Fig. 3.3
q1e4a03	10^{-4}	0.03	20	$[4.1, 2.6]$ $[3.3, 1.2]$	-0.28 see Fig. 3.3
q1e3a1	10^{-3}	0.1	20	$[10.3, 6.5]$ $[8.2, 3.0]$	0.33 see Fig. 3.5
q3e4a1	3×10^{-4}	0.1	20	$[6.4, 4.0]$ $[5.1, 1.9]$	0.38 see Fig. 3.5
q1e4a1	10^{-4}	0.1	20	$[4.1, 2.6]$ $[3.3, 1.2]$	-1.27 see Fig. 3.5
q1e3a03m10	10^{-3}	0.03	10	$[8.2, 3.0]$	see Fig. 3.7
q1e3a03m30	10^{-3}	0.03	30	$[8.2, 3.0]$	see Fig. 3.7
q1e3a03 (no sink)	10^{-3}	0.03	20	$[8.2, 3.0]$	see Fig. 3.9

Table 3.1: List of simulations and parameters used throughout this work. Each binary is given a migration rate that corresponds to the binary evolution from an initial separation r_i to a final separation r_f. In cases where we run two simulations for a single binary to probe different migration rates, two ranges of radii are listed. We also show the average torque value (measured in the last 1000 orbits) in simulations for which we calculate the SNR of the gas deviation.

intermediate mass ratio regime.

3.3.1.1 Mass ratio

Fig. 3.3 shows the gas torque T_g normalized by T_0 as a function of migration rate for three different mass ratios, in a disk with $\alpha = 0.03$ and $\mathcal{M} = 20$. As we expect from similar studies of torques on stationary satellites, torques are stochastic in this regime. In fact, when increasing q from 10^{-4} to 10^{-3}, torques change sign. This particular behavior is dependent on the current choice of α.

For a reference of the magnitude of these torques, we take the average torque on each binary, taken in the last 1,000 orbits of the slower portion of the inspiral, and compare this to the GW torque for each mass ratio during the last stages of coalescence in Fig. 3.4. The average measured in the simulation is extrapolated to earlier times for the smaller mass ratios (shown by dashed lines). To scale to a physical value we normalize the surface density to our estimate for a β-disk making this a high-end estimate of the torque strength. In all cases, despite the high assumed disk density, gas torques are several orders of magnitude weaker than that due to GWs at this stage of coalescence.

The normalized torque for all runs oscillates around a constant at earlier times, but deviates towards stronger torques (either negative or positive) as the inspiral rate increases. This happens at the final stages of the inspiral (the final $\sim$ 1000 orbits), and in the case of the smallest mass ratio $q = 10^{-4}$, the merger occurs before migration has a chance to substantially affect the torque. However, as we describe below, when this deviation occurs depends on other disk properties.

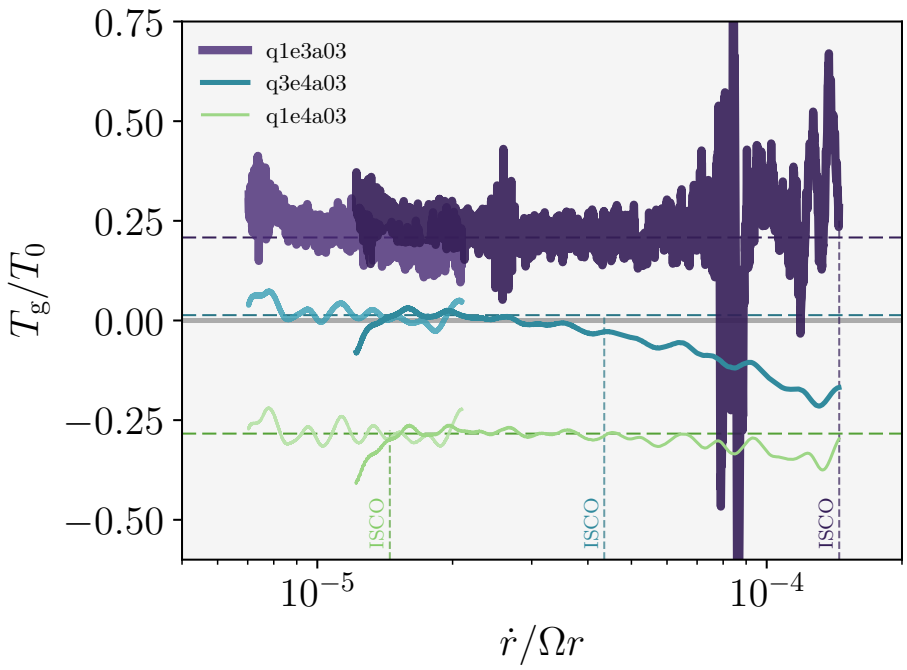

Figure 3.3: Total torque as a function of dimensionless migration rate, normalized by the Type I torque T_0, for each q. Dotted lines show the average in the last 1000 orbits of the slow migration runs. In the last few thousand orbits, higher mass ratios show a deviation from this average due to fast migration. Vertical dashed lines mark which migration rate corresponds to the ISCO for each q.

3.3.1.2 Viscosity

Viscous forces govern the gap depth and formation timescale. As gas must be flowing from the outer disk to the inner disk via streams around the BH, viscosity is intimately tied to gas dynamics near the BH. For this reason it is not surprising that both the magnitude and direction of the torque change with α. Particularly for intermediate mass ratio binaries (and even up to $q \sim 0.5$, see Duffell et al. 2019b), simulations show that even small changes in α can change the sign of the torque (Duffell 2015b).

We run a second set of inspiral simulations in a disk with $\alpha = 0.1$ to observe changes

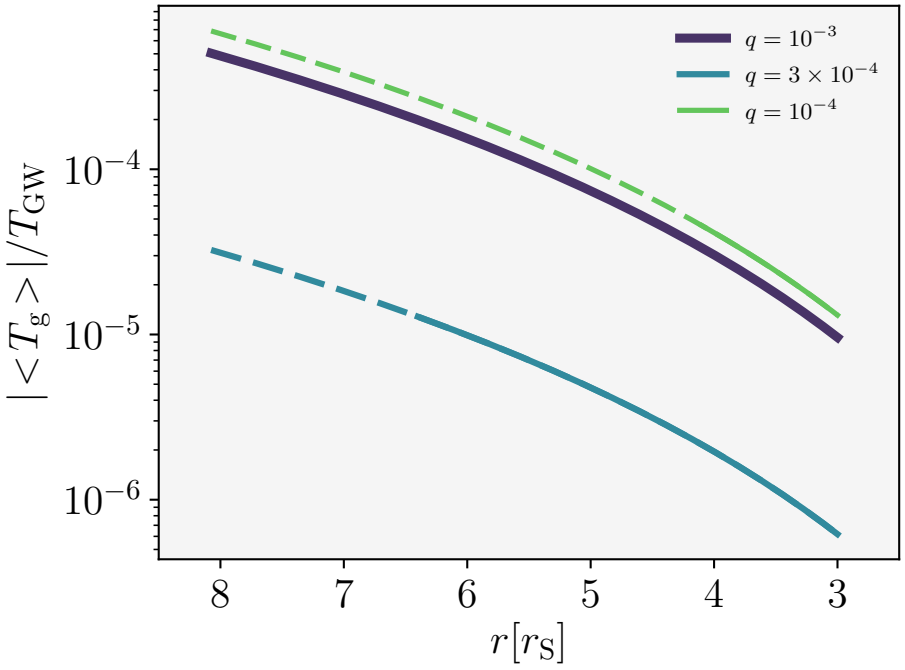

Figure 3.4: Average torque from simulations of three different mass ratios with $\alpha = 0.03$ and $\mathcal{M} = 20$, divided by the GW torque during the last few r_S to ISCO. The dashed lines indicate the radii for which the torque is extrapolated outside of the simulated range. Gas torque is normalized assuming Σ_β, a high end estimate for the disk surface density.

in the overall torque and its evolution with migration rate. Results are shown in Fig. 3.5, with the same scaling to compare to Fig. 3.3. We find that the magnitude $|T_{\rm gas}|$ typically increases in strength with α, as has been observed in other numerical studies (e.g. Robert et al. 2018).

Viscosity acts to stabilize a disk whose state is constantly disrupted by an embedded perturber. Intuitively we expect that for higher values of viscosity, migration should have less impact on the torque, simply because the disk can reorganize more quickly. Indeed, this is what we observe as shown in Fig. 3.5. For all mass ratios, the torque (minus small scale oscillations) is essentially constant throughout the entirety of the inspiral when $\alpha = 0.1$.

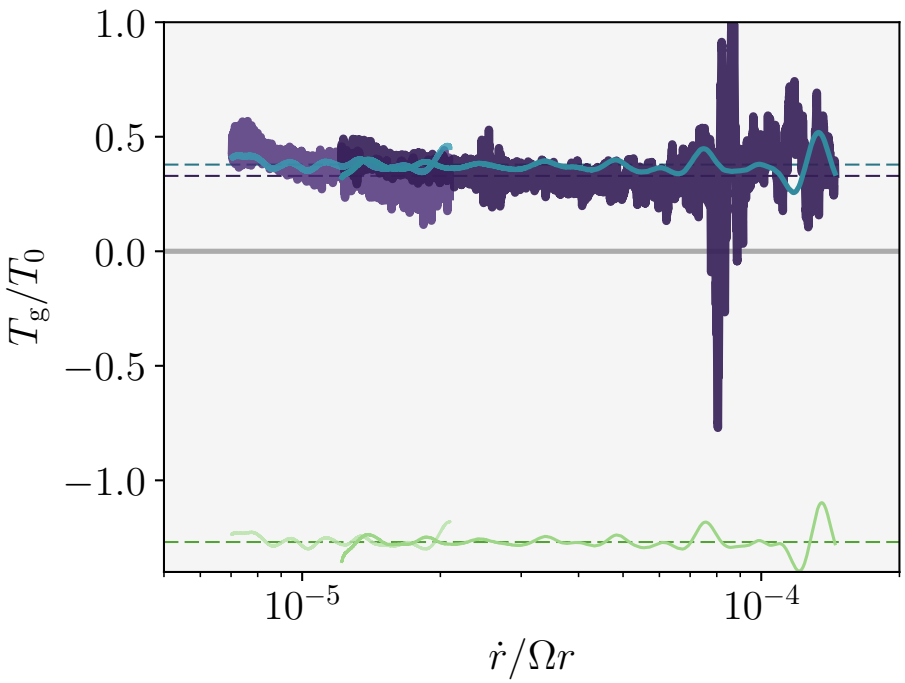

Figure 3.5: Gas torque normalized by T_0 for runs with $\alpha = 0.1$. Higher viscosity means the disk stabilises more quickly, and torques do not change as significantly as migration rate increases.

In the case of thin, fully ionized disks in near-Eddington AGN, observational evidence suggests that viscosity may reach values $\alpha = 0.1 - 0.4$ (King et al. 2007). Thus E/IMRIs in such viscous disks may be subject to stronger torques, but are less likely to show significant changes in torque strength during the inspiral. We conclude that in these cases, torques on average may follow a simple scaling with radius, which we discuss further in Section 3.4.

3.3.1.3 Mach number

The Mach number, a measure of disk temperature and thickness, is also a critical factor in determining the gap depth and disk dynamics near the BH. A low Mach number disk is subject to stronger pressure forces, resulting in shallower gaps, while a higher Mach number

describes a dynamically colder disk that can consequently form deeper gaps.

For our fiducial system with $q = 10^{-3}$, we explore a range of Mach numbers from $\mathcal{M} = 10 - 30$. While this range is limited (as we expect thin AGN discs to be highly supersonic, which $\mathcal{M} \sim 100$), we are able to observe trends in gap depth and gain insight into the increasingly complicated gas dynamics close to the BH.

Fig. 3.6 shows surface density contours of gas close to the BH at the end of each simulation. For the lowest Mach number (which, we note, is a value often adopted in binary simulations), pressure forces significantly smooth the flow. The resulting torque is *negative*, rather than positive as in the $\mathcal{M} = 20$ case. For the highest Mach number ($\mathcal{M} = 30$), gas flows more tightly around the BH (indeed, the scale height and corresponding smoothing length ϵ is smaller). Gas morphology within the Hill radius is dynamic, with narrower streams that flow across a deeper gap and stark density contrasts that lead to instabilities in the gap edges and streams. Ultimately this produces a noisy torque that is difficult to measure numerically.

Fig. 3.7 shows the resultant torque exerted on the BH. Not only does the value and sign of the torque change with $\mathcal{M}$, but more notably colder disks show an increase in variability in the torque as the BH migrates. We expect that disks that are more dynamically cold may be more sensitive to changes in BH position during a GW inspiral. Without stronger pressure forces to smooth out fluctuations in the flow close to the BH, gas torques may be more sporadic and variable.

3.3.2 Dissecting the torque

With our simulations we have the ability to assess different contributions of the disk to the gravitational torque. Of particular interest is being able to distinguish between gas very close to the BH, within the Hill radius (Eq. 2.13), and that from elsewhere in the disk, including

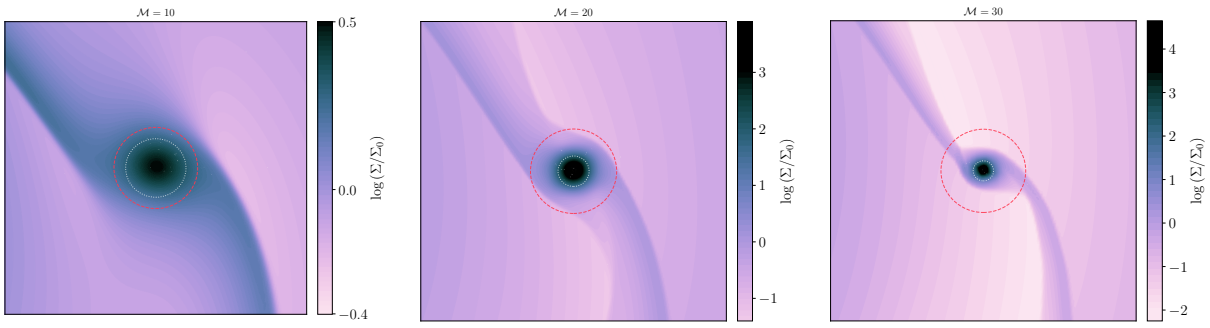

Figure 3.6: Density contour zoomed in on the Hill sphere for three different Mach numbers. Lower Mach number disks are hotter and subject to strong pressure forces that smooth out the flow. For higher Mach numbers, gas flow across the gap occurs along thinner streams, the BH carves a much deeper gap, and gas inside the Hill sphere is more sensitive to changes in the BH position. Note the different color scalings in each of the panels.

the inner and outer disks as well as streams crossing the gap.

As discussed in Chapter 2, when $q = 10^{-3}$, gas pile-up close to the BH becomes non-negligible. This can be seen in the density contrasts in Fig. 3.1 or in Fig. 3.8, where we show various distributions of torque density $\mathcal{T}$ for our fiducial $\alpha = 0.03$ runs for each q. Excising the Hill radius allows us to observe contributions to the torque from nearby streams, while zooming in on the Hill radius allows us to analyze the most dominant contribution to the torque density (due to its proximity to the BH). This is most prominent for $q = 10^{-3}$, where a high density atmosphere accumulates close to the BH. Despite such high values of $\mathcal{T}$, the net torque in this region remains below T_0, implying that as density around the BH increases, to some extent so does its degree of symmetry.

Gas within the Hill radius still contributes a substantial fraction to the total torque, as we show in Fig. 3.9, where we divide torque into contributions from gas within and outside of the Hill radius for the fiducial $q = 10^{-3}$ inspiral. Gas inside $r_{\rm H}$ is responsible for the positive component of the torque and also shows the strongest response to migration, increasing from $\sim 4r_{\rm S}$ to $3r_{\rm S}$.

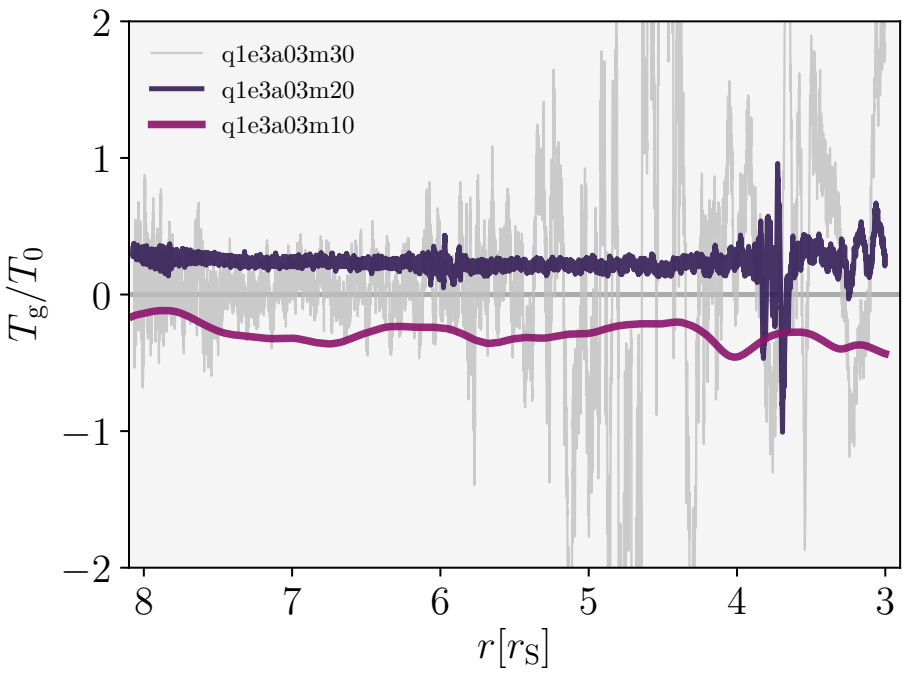

Figure 3.7: Gas torque for three different Mach numbers. With higher Mach number, the torque shows sporadic variability throughout the inspiral.

Gas within the Hill radius is sometimes assumed to not contribute to the torque (e.g. Dempsey et al. (2019)), despite that this gas is a crucial component of material flow across the gap and may exhibit non-negligible asymmetry. Indeed, in simulations by Crida et al. (2009), the migration rate of a live planet is dependent on how much the material in the Hill sphere is dampened, suggesting that this torque is indeed a physical component.

In the present work, the Hill sphere torque is of particular importance as the asymmetry near the BH may be exacerbated with migration (here driven by GWs), and we expect that any changes in the torque during a GW-driven inspiral will first arise from gas closest to the BH. This is shown more clearly in versions of our fiducial run for which the sink prescription is turned off (shown as light lines in Fig. 3.9). Unsurprisingly, an accreting BH experiences less positive torque as density within the Hill radius is depleted. Without

accretion, however, torque within $r_{\rm H}$ substantially increases with migration rate, more than doubling in comparison to T_0 within the final 5,000 orbits of the inspiral (from $8r_{\rm S}$ to $3r_{\rm S}$). If the evolution of the torque for more massive IMRIs (as we see for $q = 10^{-3}$) is sensitive to accretion efficiency of the secondary BH, this raises the hope that detecting the torque evolution with frequency may provide insight into the gas dynamics near the BH.

Satellites with mass ratios smaller than $q = 10^{-3}$ accrete an insignificant amount of material according to our sink prescription−they experience no significant pile-up of gas in their orbit due to their weaker gravitational pull−so accretion has a negligible impact on their torque evolution.

3.3.3 Torque evolution

Does the torque on an embedded IMRI change in response to migration? The short answer is: it depends. Whether migration produces a significant effect on the torque depends on the mass of the inspiraling BH, the disk viscosity, Mach number, and the BH accretion efficiency.

During the inspiral, we observe three effects that are possibly correlated with migration. First, for all simulated binaries, the torque on a migrating BH shows long-term oscillations (on a timescale of $\sim$ 100s of orbits). These modulations arise from global perturbations as they are present in the torque contribution from outside the Hill radius. The magnitudes are of order $\lesssim 10\%$, so for detectability purposes the torque can be approximated by an average, or possibly a stationary approximation for Type II torques (however, analytical approximations tend to neglect the ability for Type II torques to become positive).

Second, depending on the mass ratio, a sufficiently fast migration rate can change the magnitude of the torque. These changes arise from deviations in the torque inside the Hill radius. For our fiducial viscosity $\alpha = 0.03$ (Fig. 3.3), the torque begins to deviate from its

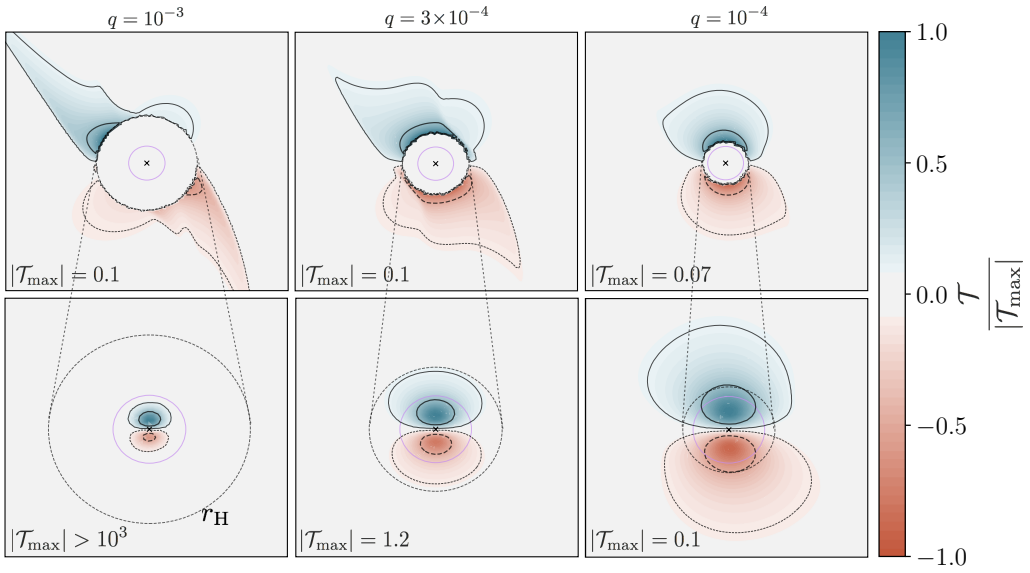

Figure 3.8: 2D contours of torque density ($\mathcal{T} \equiv \mathbf{g}_\phi \times \mathbf{r}$, equivalently a torque per unit disk surface area) close to the BH. In the top panels we have excised the gas in the Hill radius (dashed circle) to highlight the gas morphology in streams nearby. Bottom panels show zoom-in views of the torque contributed by gas within the Hill sphere. All contours are normalized by the maximum $\mathcal{T}$, printed in each panel for reference. Note that gas pile-up for $q = 10^{-3}$ is deep within the Hill radius and reaches significantly high densities. This results in much higher torque densities. The smoothing length of the gravitational potential is denoted with the solid purple circle.

steady-state value[1] at migration rates approaching $\dot{r}/\Omega r \sim \times 10^{-4}$. In reality, this rate is only reached in a circular binary with $q \geq 10^{-3}$. Smaller mass ratio binaries merge before reaching this rate. However, this trend is dependent on accretion efficiency and disk viscosity. In disks with lower viscosity (or less efficient accretion), we expect this deviation to occur at earlier times. Overall we find that the most prominent torque evolution occur for $q = 10^{-3}$, due to the significant pile-up of gas in its Hill sphere. Interestingly enough, our $q = 3 \times 10^{-4}$

[1]We note that the decreasing trend in the gas torque reported in Chapter 2 was in fact a long-term transient due to the simulation having a closer outer boundary. Our slower migration runs confirm that the normalized torque on a $q = 10^{-3}$ IMRI is indeed constant (albeit with oscillations) until reaching separations near $\sim 4r_{\rm S}$, although this depends on the accretion rate.

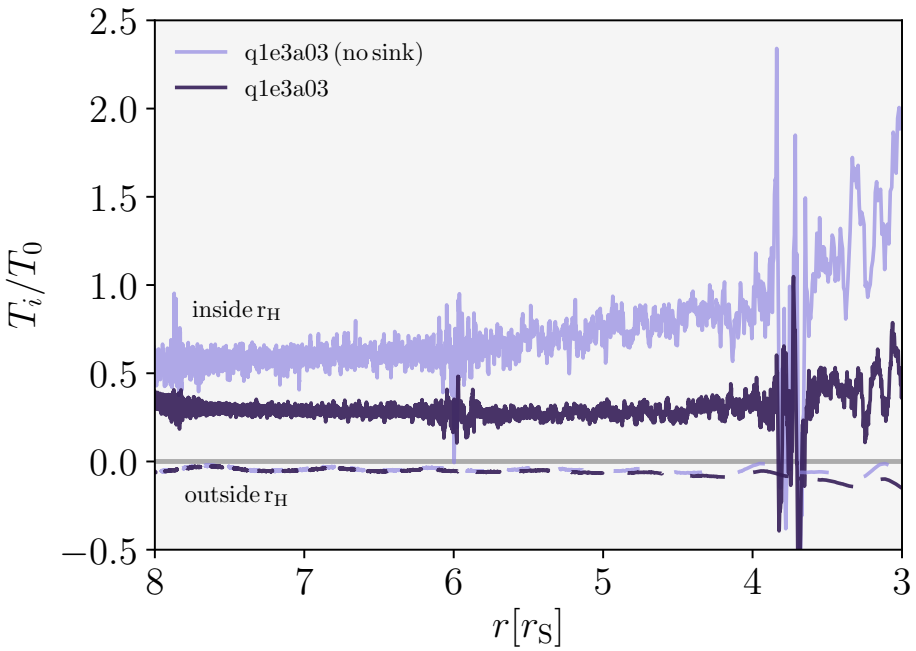

Figure 3.9: Torque on a $q = 10^{-3}$ mass ratio inspiral divided into contributions from within and outside of the Hill radius, compared to the torque from a run with no accretion. Accretion damps the torque component inside the Hill radius, which otherwise would be affected by the increasing inspiral rate.

simulation experiences a *sign change* in the torque as it approaches merger. In this case, gas torques would initially slow down the inspiral before suddenly accelerating it.

Finally, migration has an impact on torque fluctuations. In particular for $q = 10^{-3}$, for which gas pile-up on the BH is most significant, the Hill sphere torque exhibits prominent fluctuations in the final $\sim$ 1000 orbits. These are more extreme for higher Mach number. While some oscillations in the torque may be numerical artifacts, some may be physical (occurring irrespective of the simulation boundary or initial conditions). In particular the noise peaks in the Hill torque for $q = 10^{-3}$ and $\mathcal{M} = 20$ may signify an interesting dynamical interaction between the BH's orbit and the gas, given that they occur at the same radii regardless of viscosity or sink rate. To test the physical nature we perform simulations with

a varying boundaries ($0.4 - 0.5 \leq r/r_0 \leq 3.0 - 6.0$) and higher resolution (up to 800 radial cells), and find that these fluctuations still occur at the same physical radii.

3.4 Significance for LISA inspirals

For the rest of this Chapter we take the results from our simulations, primarily the average torques during the $\alpha = 0.03$ and $\alpha = 0.1$ runs, and analyze their detectability if present in a GW signal. First we describe some relevant quantities that describe a GW event as it arises in the LISA band, with the goal of computing the detectability of the gas imprint in an event subject to the environmental torques.

As illustrated in Figure 3.2, the inspiral rate for each mass ratio corresponds to a physical separation and gravitational wave frequency. Recall that the GW frequency is twice the orbital frequency for a binary on a circular orbit, $f = 1/\pi\sqrt{GM/r^3}$, and we have chosen these migration rates to correspond to IMRIs in the LISA frequency band.

In Fig. 3.10 we plot the characteristic strain (Section 1.4) of IMRIs at each simulated mass ratio for two different possible observations of duration $\tau = 4$ years, the (updated) nominal LISA mission lifetime (Amaro-Seoane 2018). Recall that the characteristic strain is an illustrative quantity, given by $h_c = h\sqrt{n}$, where $n \equiv f^2/\dot{f}$ is a measure of the total number of cycles the source spends at each frequency (see Sesana et al. 2005 for a more detailed derivation). We assume a fiducial primary mass $M_1 = 10^6 M_\odot$ and place the source at redshift $z = 1$. These parameters are listed in Table 3.2. The dashed lines correspond to the final 4 years of the binary to merger (assumed to occur at $r_{\rm ISCO} = 3r_{\rm S}$), and the shorter, solid lines correspond to a 4-year evolution if the binary were to reach $15r_{\rm S}$ (in its rest frame).

For a fixed primary mass, binaries with smaller mass ratios (smaller $\mathcal{M}_{\rm c}$) emit weaker

Fiducial Parameters and LISA Specifications		
z	Redshift	1
M	Primary Mass	$10^6 M_\odot$
τ	LISA mission lifetime	4 yrs
L	LISA arm length	2.5 million km
N	Number of laser links	6

Table 3.2: LISA parameters are used when computing detectability.

gravitational waves, and thus span shorter frequency windows during an observation of fixed time τ. This reduces the total SNR (Eq. 2.23) as well as the chances of detecting a deviation in a signal.

3.4.1 Gas imprints in GWs

3.4.1.1 Phase drift

Depending on the mass ratio and viscosity, gas either slows down or speeds up the inspiral. For a gravitational wave event in the LISA data stream, this arises as a shift in the total accumulated phase of an event, or a phase drift in the waveform compared to that in vacuum. Recalling from Chapter 2, if the accumulated phase of an event (often defined in Fourier space) due to merely GW emission is $\Phi_{\rm GW}(f)$, the phase of an event experiencing gas torques will be $\Phi_{\rm GW}(f) + \delta\phi(f)$, the underlying vacuum signal plus some small deviation which can also depend on frequency. If the phase deviation $\delta\phi(f)$ is significant (and unique), the gas imprint is potentially distinguishable from the vacuum waveform. This ultimately depends on a few things: (i) the strength of the gas torque compared to GWs, which changes with radius; (ii) the frequency window that is observed, as this affects how much the system is chirping; and (iii) the signal to noise ratio (SNR) of the event itself. All of these factors will be affected by the mass ratio of the binary.

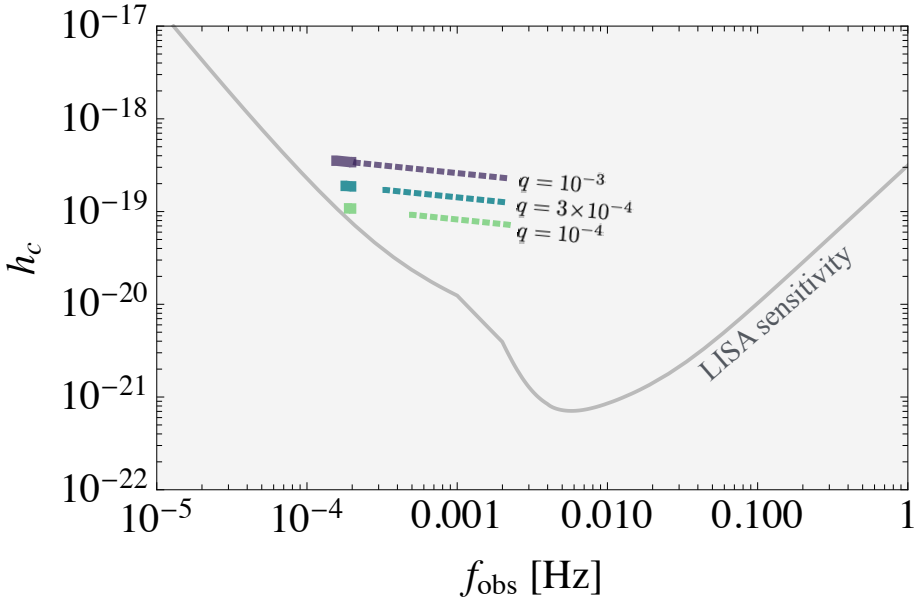

Figure 3.10: The characteristic strain as a function of observed frequency. For each mass ratio we show two possible observations of duration $\tau = 4$ years, using our fiducial parameters $M_1 = 10^6 M_\odot$ and $z = 1$. Dashed lines correspond to the final 4 years of the inspiral up to merger ($r_{\rm ISCO}$), and solid lines at lower frequencies correspond to earlier observations that reach a rest-frame separation of $15r_{\rm S}$. The sensitivity curve is provided by Klein et al. 2016.

For calculating the phase shift induced by gas we take the same approach as described in Section 2.5, but we implement the updated result for the simulated gas torque and apply this to all simulated mass ratios.

Given that gas torques are much weaker than GWs (Fig. 3.4) and assuming the inspiral remains circular, the phase drift (in radians) can be integrated by

$$\delta\phi = 2\pi \int_{r_{\rm min}}^{r_{\rm max}} \frac{f_{\rm GW}\,\dot{r}_{\rm gas}}{\dot{r}^2_{\rm GW}} \left[1 + \mathcal{O}\left(\frac{\dot{r}_{\rm gas}}{\dot{r}_{\rm GW}}\right)^2\right] dr, \tag{3.12}$$

where $\dot{r}_{\rm gas}$ is the change in separation due to gas torques. Note that $\dot{r}_{\rm gas}$ can be a function of radius, as we define explicitly below, but that this function can vary for different systems.

As shown in our fiducial runs, the magnitude of the gas torque when normalized by T_0 is approximately constant throughout the inspiral for all mass ratios. To compute detectability we use the average of these torques (dashed lines in Fig. 3.3). We neglect the small scale oscillations in the torque as well as the deviations from the average that occur at high migration rates. Given that normalized torques either stay nearly constant or increase in absolute value with inspiral rate, this provides a lower limit on detectability.

If $T_{\rm g}/T_0$ is constant throughout the inspiral, then torques scale with the radial dependence of T_0, which is dependent on the disk density profile. We can define the gas torque analytically as

$$T_{\rm gas} = C_{\rm fit} T_0(q, r, \mathcal{M}, \alpha, \Sigma(r)), \tag{3.13}$$

where $C_{\rm fit}$ is the (constant) average of the torque before it begins to deviate due to migration. These fits are shown as horizontal dashed lines in Fig. 3.3 and also provided in Table 3.1.

Expressing the gas torque in terms of the rate of change of specific angular momentum $\dot{\ell}_{\rm gas} = T_{\rm gas}/M_2$ allows us to solve for the shift in GW phase due to the gas torque on each binary, provided some observed frequency window. We integrate over two different frequency

windows for each mass ratio, defined by 4-year observations shown in Fig. 3.10. Since our simulated inspiral does not cover the entire observed frequency range, we extrapolate the torque fit from Eq 3.13 to the earlier stages, which implicitly (and reasonably) assumes that torques scale with T_0 at earlier times.

3.4.1.2 Detectability of waveform deviation

Let us calculate the detectability of a deviation in the waveform, once again with an integral for the SNR of the difference between a phase-shifted waveform and a vacuum waveform (Eq. 2.22). This allows us to assess, given a disk density, how distinguishable the phase-shifted waveform will be from the vacuum waveform. We hold the assumption that the gas only imparts a difference in GW phase and not amplitude, also known as the Stationary Phase Approximation (as seen in Yunes et al. 2011 and Kocsis et al. 2011).

We show the accumulated SNR of the gas-induced deviation for the $\alpha = 0.03$ runs in Fig. 3.11 as a function of disk surface density normalization Σ_0. Just as the phase shift depends linearly on the surface density, $\rho_{\delta\phi}$ initially scales linearly with Σ_0. However, at high enough surface densities, where torques shift the phase by a whole period ($\delta\phi \gtrsim 2\pi$), the SNR saturates. This behavior is observed in binaries that are essentially monochromatic in frequency, an inevitable feature of circular, small mass ratio inspirals that coalesce very slowly.

The exception is for binaries that are approaching merger, whose phase shift accumulates past 2π as they sweep through higher frequencies. Thus if an IMRI is embedded in a disk with surface densities reaching that of the β-disk model, and we are lucky to observe the late stages of coalescence, its waveform may be significantly altered.

The distinguishability is still ultimately a function of the SNR of the event itself, which is affected by the mass ratio. To highlight this interplay we show the SNR of the deviation

divided by the SNR of the event (a relative SNR, $\rho_{\delta\phi}/\rho$) in Fig. 3.12.[2] This illustrates that the accumulated deviation (related to $T_{\rm gas}/T_{\rm GW}$) for inspirals that are chirping is weaker than at earlier times (as seen by the dashed lines in Fig. 3.12). But as we see in Fig. 3.11, these weaker deviations are the most detectable, primarily due to the increasing sensitivity of LISA at frequencies where IMRIs merge, which allows for sources at this stage to accumulate substantial SNR. Basically, a smaller deviation in a louder source is more detectable.

Adopting a detectability threshold of $\rho_{\delta\phi} \gtrsim 10$, we conclude that the gas imprint is detectable for all simulated mass ratios *if* observed during the final 4 years to merger, given a disk density that exceeds $\Sigma_0 \gtrsim 10^{4-6}\,{\rm g\,cm^{-2}}$. The required surface density for detectability is dependent on the strength of the torque, which varies for each value of the mass ratio.[3] Given that the gas torque on the $q = 3 \times 10^{-4}$ binary was a order of magnitude weaker than the higher mass ratios, it requires a correspondingly higher Σ_0 for detectability. The detectability of gas for smaller mass ratios at earlier stages suffers from weaker GW emission and less frequency evolution, and gas torques are undetectable even for the highest disk densities.

For higher viscosities, where torques are stronger for each mass ratio, the detectability of a deviation is improved (Fig. 3.13), and an SNR deviation of $\rho_{\delta\phi} \gtrsim 10$ can be reached with lower disk densities ($\Sigma_0 \gtrsim 10^{3-5}\,{\rm g\,cm^{-2}}$). However, this is still dependent on the binaries being in their final stages of the inspiral.

One may wonder how our choice of primary mass affects detectability. In principle IMRIs can occur for more or less massive primary MBHs. We demonstrate the effect of our choice of primary mass M_1 for a fixed mass ratio $q = 10^{-3}$ in Fig. 3.14. Higher mass

[2]Note that the relative SNR saturates to unity at high disk densities, when the SNR of the deviation becomes comparable to the SNR of the event. In Figure 2.7 of Chapter 2, this saturation occurs slightly above unity, due to a small error in the SNR integral.

[3]Compared to Chapter 2, $q = 10^{-3}$ requires a slightly higher Σ_0 for detectability because we are using a weaker estimate for $T_{\rm g}$.

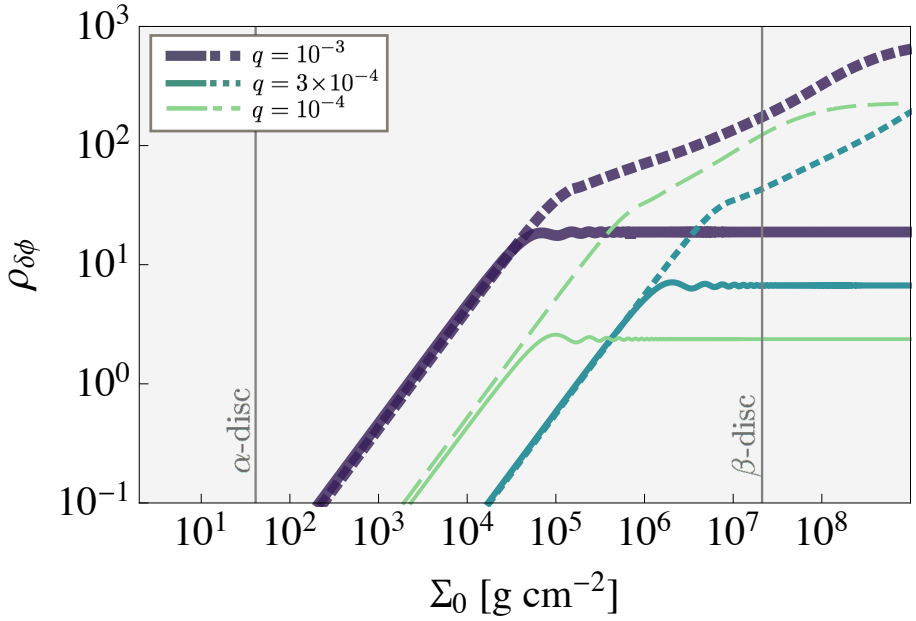

Figure 3.11: Accumulated SNR of the waveform deviation in our $\alpha = 0.03$ runs, assuming fiducial binary parameters $M_1 = 10^6 M_\odot$ and $z = 1$ and a 4−year LISA observation. Observations at lower frequencies (solid lines) saturate once the phase shift reaches $\delta\phi \approx 2\pi$. Observations at later stages of coalescence continue to accumulate a larger phase shift due to the changing frequency, thus higher values of disk density lead to large SNR. The intermediate mass ratio $q = 3 \times 10^{-4}$ binary experiences the weakest gas torque, so the gas imprint is only detectable ($\rho_{\delta\phi} \gtrsim 10$) for larger disk densities.

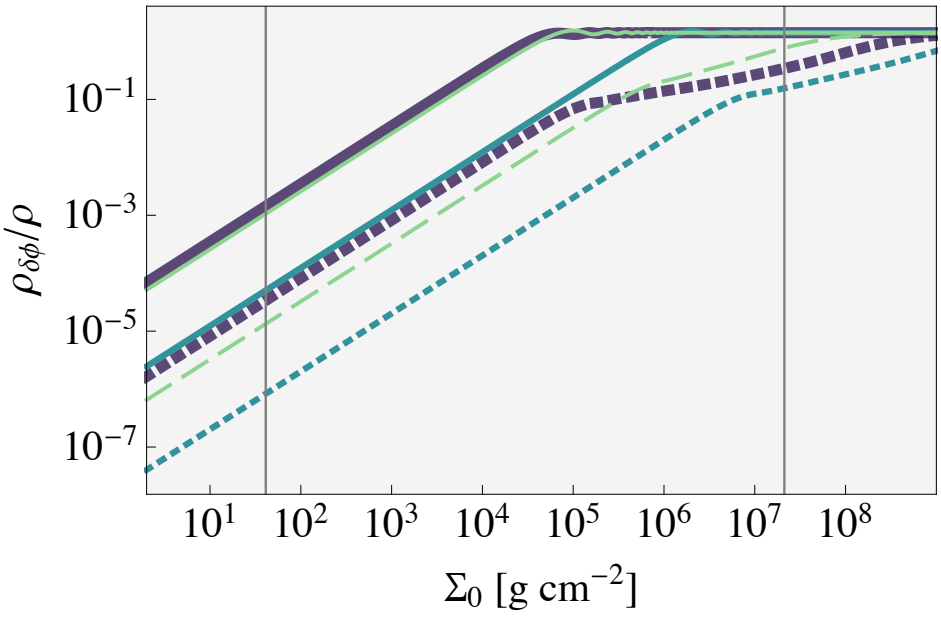

Figure 3.12: Relative SNR (SNR of the deviation divided by the SNR of the event) for the $\alpha = 0.03$ runs, with the same color key depicted in Fig. 3.11.

binaries emit louder gravitational waves, but they merge at lower frequencies due to their increasingly large ISCO ($r_S \propto M$). Taking the mass ratio $q = 10^{-3}$, we plot the strain and corresponding detectability of the phase shift, given the gas torque from our fiducial run (q1e3a03, where $T_{gas}/T_{GW} = 0.21$). We fix each observation window to the binary reaching $3r_S$ in a 4 year observation. In this case the lower mass binary exhibits more detectable gas torques, given that it merges at frequencies where the LISA noise is at its lowest. Additionally, lower mass binaries span a larger frequency range in a fixed observation time, simply because the frequency evolution rate $\dot{f}$ scales more steeply with frequency than chirp mass ($\dot{f} \propto M_c^{5/3} f^{11/3}$, see Sesana et al. 2005).

The detectability of the gas deviation is tied to the portion of the coalescence we observe– binaries that are chirping in the cusp of LISA sensitivity are the most hopeful candidates for extracting a phase shift.

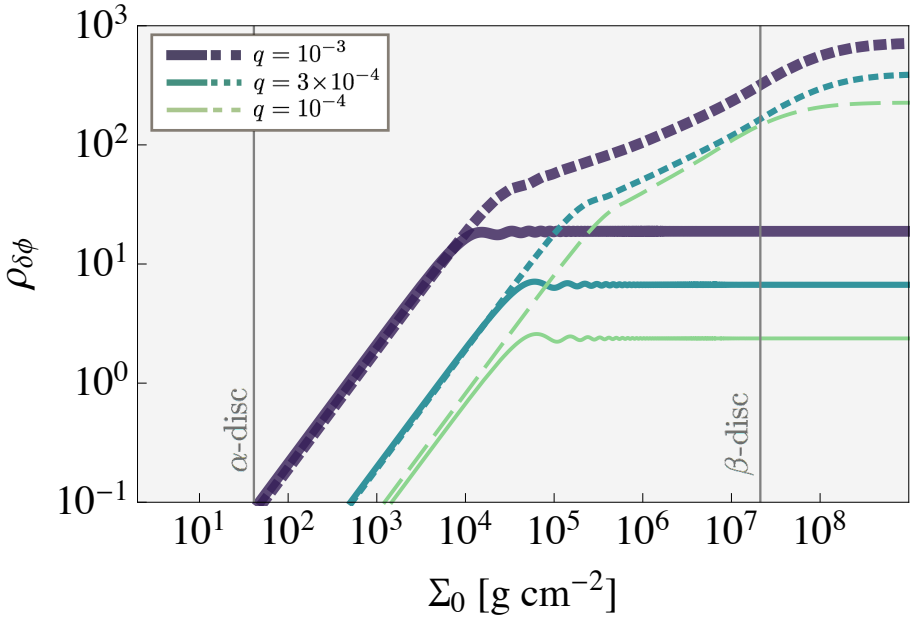

Figure 3.13: Accumulated SNR of the deviation for the $\alpha = 0.1$ runs. Higher viscosity generally produces stronger torques; hence the imprint is detectable at lower disk densities.

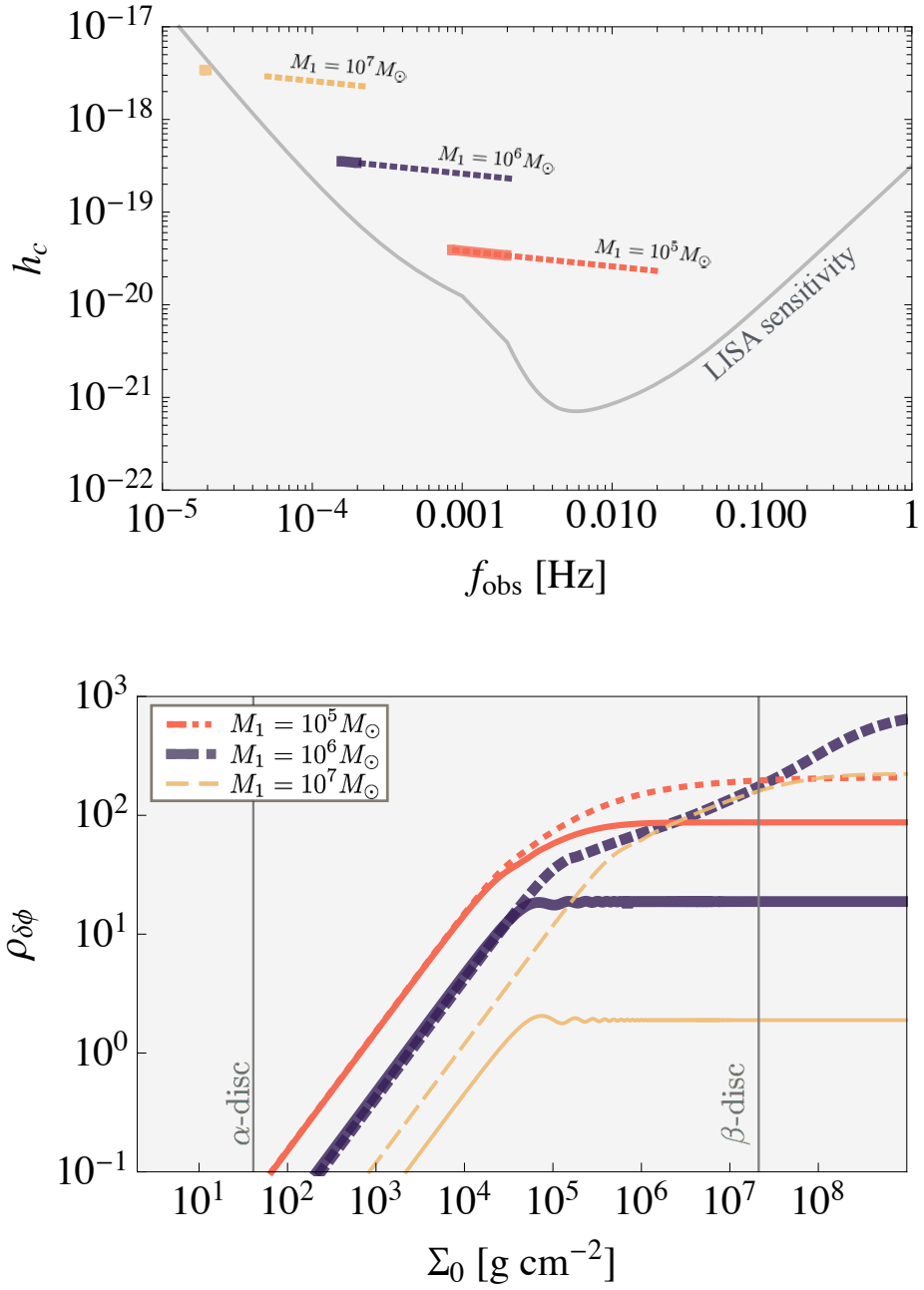

Figure 3.14: *Top panel*: Strain h_c of $q = 10^{-3}$ binaries, varying the primary mass M_1 from $10^5 M_\odot$ to $10^7 M_\odot$, for two 4-year observations that reach the ISCO (dashed line) and 15 $r_{\rm S}$ (thicker line). For a decreased binary mass, the merger occurs at a smaller $r_{\rm ISCO}$ and correspondingly higher frequencies. This affects the detectability of the event. *Bottom panel*: SNR of gas deviation as a function of disk surface density given the observation windows depicted above, and using the gas torque for the $\alpha = 0.03$ run. In this case, gas impact is more detectable for a binary with $M_1 = 10^5 M_\odot$, even if observed at earlier stages, because this event accumulates high SNR. Note that the vertical line for the Σ_β estimate corresponds to a disk around an $M_1 = 10^6 M_\odot$ BH; see Eq. 3.10 for weak scaling with BH mass.

3.4.2 Uniqueness and degeneracies

It is important to consider whether deviations in the waveform are degenerate with other possible environmental effects, or if they may hinder parameter estimation or chances of detection.

A critical feature for distinguishing between various environmental effects and system parameters is the respective scaling of each effect with binary separation or GW frequency. For example, some proposed modifications to general relativity predict waveform deviations that would increase as the EMRI coalesces, scaling with frequency to some predictable power (Yunes 2009). In principle a deviation to the waveform could be interpreted as a binary with different system parameters that also affect the frequency evolution, such as chirp mass M_c. This can be distinguished by how various parameters affect the waveform as the frequency evolves. This dependence is often quoted in Fourier space, where deviations can be compared to Post-Newtonian (PN) terms in the Fourier phase. The scaling of changes in parameters with frequency can then be compared amongst system parameters, external effects, or even deviations from general relativity.

Neglecting small scale deviations, our simulated gas torque scales with the analytical estimate T_0, which is a function of the disk density profile. Given our disk model, $T_{\rm gas} \propto r^4\Omega^2\Sigma(r) \propto r^{1/2}$. The viscous torque also carries the same scaling with radius, given by $T_\nu \propto r^2\Omega\nu(r)\Sigma(r) \propto r^{1/2}$. This predicts that gas torques get progressively weaker as the binary coalesces: If $f_{\rm GW} \propto r^{-3/2}$, then the gas torque initially scales with GW frequency as $T_{\rm gas} \propto f_{\rm GW}^{-1/3}$, and the integral for the deviation scales as $\delta\phi \propto f^{-13/3}$. This can be compared to the phasing function for a circular inspiral around a non-spinning BH, where 1.5 PN terms scale with frequency as $\phi(f) \propto Af^{2/3} + Bf$ (where A and B are constants that depend on system parameters, see a more detailed description in Will & Yunes 2004). So in this case,

gas torques scale uniquely with frequency, suggesting that migration is non-degenerate with system parameters or GR corrections. Similar negative powers of frequency may arise in modified gravity theories, but these would be present in all E/IMRIs while gas will only affect a subset.

This estimate excludes deviations in the torque that can occur at the fastest migration rates, particularly for lower viscosity disks, or if the BH migrates through a disk where parameters vary with radius. It also neglects the oscillations that occur in the torque which we see for all simulated migration rates. If measurable, these time-variable fluctuations could be a smoking-gun signature of disk response to an embedded IMRI. Ultimately the frequency dependence of the effect varies with disk physics, and changes in α, $\mathcal{M}$, or even accretion efficiency will lead to different scalings.

3.5 Caveats

This study provides a crucial step in determining how migration torques respond to a GW-driven inspiral. We summarize our limitations here.

Our simulations are 2-dimensional and do not resolve any 3-dimensional gas morphology which may be particularly important for resolving torques close to the secondary. Our disk model is isothermal and does not include radiative cooling or heating, and we neglect more sophisticated physics such as magnetohydrodynamics or radiation pressure, all of which may alter the gas dynamics near the BH. As we have shown for the $q = 10^{-3}$ inspiral, gas near the secondary BH plays a critical role in the torque direction and temporal evolution. Future work must consider 3D gas morphology more closely, and how it is affected by accretion rate and feedback, if one wants to make more accurate predictions for LISA.

In particular, the choice of accretion prescription and sink timescale of the embedded

BH should be considered carefully. Our estimate assumes that accretion occurs on the viscous timescale via a thin disk around the BH. However, given that the specific angular momentum of the gas with respect to the gap-opening perturber is low (and the resulting accretion torque is negligible, as discussed in Chapter 2), perhaps a quasi-spherical accretion prescription (i.e., Bondi accretion, Edgar (2004)) would be more appropriate. The possibility for super-Eddington accretion rates should be considered, which can result in feedback that further affects the orbital properties of the BH (Gruzinov et al. 2020).

Our simulations are purely Newtonian, neglecting any relativistic effects which can alter gas dynamics in the inner regions of the accretion disk closer to the primary BH ISCO. We assume the binary inspiral remains circular, when in fact gas discs may excite non-negligible eccentricity to the orbit, and this eccentricity may also produce additional modulations in the torque. Moreover, our estimates of binary evolution may be slightly inaccurate due to our use of the Peter's formula for the inspiral rate, which is lacking PN terms that can slow down binary evolution (Zwick et al. 2019).

These simulations are numerically challenging in that they require a large boundary and adequate resolution, and they must be evolved for several thousand dynamical times. Incorporating any of these processes would sacrifice computational efficiency, which is a critical strength in our setup that allows for a substantial parameter study. We argue that while our model neglects some realistic physics, it is valuable to determine whether migration torques evolve in the simple isothermal case, in order to isolate which affects are most important before introducing more complicated physics which can convolute results.

3.6 Discussion

In the present work we analyse torque evolution during GW-driven inspirals in the intermediate mass ratio regime. These sources, while their rates are less certain, provide the tantalizing possibility of probing nonlinear binary+gas-disk physics. At smaller mass ratios, they evolve more slowly and quietly than equal mass MBH mergers, yet they maintain the ability to accumulate significant SNRs compared to the LISA noise.

In all cases, we observe small scale modulations in the torque throughout the inspiral. For most cases, torque follows the radial evolution of T_0 or T_ν, but its value does not scale predictably with q. The strength and direction of the torque, as seen in similar studies, is sensitive to q, and so is its response to migration. For our highest simulated mass ratio $q = 10^{-3}$, where gas pile-up on the BH is significant, torques are noisy and sensitive to accretion efficiency. As the migration rate increases, torques increase in strength (becoming more positive) and also exhibit increased variability. For larger perturbers, this effect could be amplified. For a slightly smaller q, torques are smoother, and become *negative* as migration increases. Thus IMRIs of similar but different system parameters can experience different torque evolution.

Unsurprisingly, the dependence of torque with migration rate is itself dependent on disk parameters, namely $\mathcal{M}$ and α. We find that inspirals in low α discs show deviations in the torque at earlier times. We interpret this as the discs inability to respond to the BHs increasing migration speeds. Given the current understanding of viscosity in AGN discs (from estimates of α in MHD simulations), such low viscosities are unlikely. In the case of higher α, torques may hold a relatively steady dependence on radius that scales with the viscous torque.

Additionally, the gas torques demonstrate a degree of variability during the inspiral.

These temporal fluctuations may highlight interesting physical processes and deserve further exploration. For example, the fluctuations in the noise amplitude in the $q = 10^{-3}$ simulations occur at the same radii regardless of the simulation boundary or sink prescription. This raises the possibility that torques may show coherence with binary separation, carry signatures of resonances between the binary and the gas, or other phenomena. We defer this analysis to future work.

The variability in the torque is highly dependent on the Mach number, or disk temperature. Hotter (low $\mathcal{M}$) disks produce smooth, 'well-behaved' torques, while thinner, colder disks will exert torques that are dynamic and spurious, albeit of comparable strength. IMRIs in high Mach number disks may exhibit the most variable gas effects, assuming the environmental effects do not hinder detectability or parameter extraction.

Assuming a gas-affected IMRI event has sufficiently high SNR and spans a large enough frequency range that a frequency-dependent waveform deviation $\delta\phi(f)$ can be measured, it will not only confirm the deviation to be of gas origin, it will also provide an invaluable measure of disk properties as a function of radius. While a measure of accumulated phase shift can place a constraint on the disk density Σ_0, in the most optimistic case a phase *drift* $\delta\phi(f_{\rm GW})$ could reveal how this evolves with radius $\Sigma(r)$, which is a distinguishing factor amongst several accretion disk models. Understanding the complex physical processes at play in the inner regions of AGN accretion discs is an active field of research. Recent radiation, magneto-hydrodynamic simulations by Jiang et al. 2019 predict that inner disk regions may have lower densities than predicted by the $\alpha-$disk model, although this should increase with accretion rate and may change with central MBH mass.

We note that these results are in the limit of our particular disk model, where the Mach number and aspect ratio do not vary with radius. This approach allows us to investigate whether changes in the torque are truly due to migration, and not due to encounters with

varying disk dynamics. Previous works suggested that torques in response to migration may change sign at fast inspiral rates (Duffell et al. 2014), but these simulations utilized a disk model with constant surface density, implying a radially dependent aspect ratio. Comparison between these types of studies highlights the importance of considering how different disk models may affect an inspiraling BH. On this basis, IMRIs embedded in more physically-motivated disks, where the Mach number changes with radius, should show more extreme changes in the torque.

The presence or absence of a phase drift should be considered in conjunction with other characteristics of the source, particularly any tell-tale signs of gas disks. A likely signature of a gas-embedded E/IMRI would be the combination of a phase drift with low eccentricity and spin-alignment with the central MBH (although, whether MBHs should be aligned with their accretion disks remains to be confirmed). Gas-embedded E/IMRIs should be less eccentric than those expected to occur in dry galactic nuclei. They may be close to circular, but with mild gas-driven eccentricity ($e \lesssim 0.2$, see Ragusa et al. 2018; D'Orazio et al., in prep; Zrake et al. in prep).

Our estimate of detectability of the deviation, or the ability to extract phase shift information from a GW event, implicitly relies on the assumption that we have a waveform catalog of all possible IMRIs. Currently, the catalog of intermediate mass ratio waveforms is incomplete (Mandel & Gair 2009b). While detection of an event is still possible if it is sufficiently loud, a lack of available waveforms will affect the accuracy with which we can extract parameters from a signal (Cutler & Vallisneri 2007). The degree to which one can extract a phase deviation from the signal will require sufficiently precise parameter extraction. Additionally, the range of possible AGN environments means that deviations may arise differently in various systems. In terms of data analysis, methods that search for *generic* deviations in the waveform are ideal, as they can then be compared to models such as that

presented here.

Gas also provide the opportunity for electromagnetic emission that may coincide with the GW event. We do not address this here, but remind the reader that combining a phase shift with any associated EM signatures would be invaluable for confirming this effect and for learning about AGN disks. For example, the coalescence of a gap-opening secondary may accompany a change in AGN continuum that correlates with the mass ratio (e.g. Gültekin & Miller 2012). This could also be correlated with the fading observed in changing-look quasars, where the characteristic timescales suggest the change in emission is due to an abrupt change in the structure of the innermost accretion disk (Stern et al. 2018). Such changes could by driven by thermal or magnetic instabilities and possibly triggered by embedded perturbers.

In general, EM signatures may shed light on the population of embedded BHs in AGN disks and their accretion properties *regardless* of the detection of GWs. Complimentary work should address possible signatures of an accreting embedded BH (or a population thereof), and its observability. A population of accreting BHs near an active MBH may be seen in certain regimes as resolvable point sources, or more generally as an additional component to the AGN continuum. If observed, one could constrain the expected population of gas-embedded inspirals before LISA flies.

3.7 Conclusions

In the present work we analyze the migration torque on an intermediate mass ratio BH binary inspiral embedded in an accretion disc. We present a suite of simulations of intermediate mass ratio inspirals embedded in 2-dimensional, Keplerian, isothermal accretion disks, where the BH is modeled as a smoothed point-mass with a sink prescription. We analyze the torque exerted by the gas onto the migrating BH for a range of mass ratios ($10^{-4} < q < 10^{-3}$),

viscosities ($0.03 < \alpha < 0.1$) and Mach numbers ($10 < \mathcal{M} < 30$). Here we summarize our conclusions:

- As in similar numerical studies, we find that torques in the intermediate mass ratio, gap-opening regime have a nonlinear scaling with disk properties. Torques either slow down or speed up the inspiral; their strength is some fraction ($\sim 1\% - 120\%$) of the Type I torque T_0 (Tanaka et al. 2002), but these values are sensitive to small changes in q, α, and $\mathcal{M}$

- During the inspiral, the torques exerted by the gas onto the BH show weak fluctuations, but the average strength of the torque (T_g normalized by T_0) remains constant for the majority of inspiral rates in the LISA band. For the fastest inspiral rates, particularly for $q = 10^{-3}$ approaching the ISCO, torques exhibit an increase in variability originating from the gas flow within the BH Hill radius.

- We scale our simulation setup to a fiducial binary with primary mass $M = 10^6 M_\odot$ at $z = 1$ in order to compute the detectability of gas-induced deviations in the GW waveform. Using the average of $T_{\rm gas}$ for each mass ratio, we integrate for the change in accumulated phase due to the gas torque, and the corresponding SNR of the deviation as a function of disk density normalisation. We find that the gas imprint is most detectable if the binary is observed during the final stages of the inspiral. At this stage the source is chirping, allowing the phase shift to accumulate past 2π, and evolving at frequencies at which LISA is most sensitive.

- The gas imprint is most detectable (SNR¿10) for the loudest source with $q = 10^{-3}$, when the source is embedded in a disk with surface density $\Sigma_0 \gtrsim 10^{3-4}\,{\rm g\,cm^{-2}}$, depending on the disk viscosity. For mass ratios $q \lesssim 10^{-3}$, gas deviations are less detectable, requiring surface densities $\Sigma_0 \gtrsim 10^{4-6}\,{\rm g\,cm^{-2}}$. These densities are attainable in models

of near-Eddington disks where the viscosity is assumed not to scale with radiation pressure (so-called β-disks), but not in the seminal α-disk model.

- This work is another step towards understanding the scope of environmental impact on LISA sources. Ultimately the strength, direction, and evolution of the torque exerted on a gas-embedded IMRI is dependent on the mass ratio and disk parameters, and the resulting waveform deviations can manifest in a variety of ways. A measure of a phase drift can provide a constraint on the disk surface density or disk structure, provided we have the tools to extract a variable deviation from the waveform data.

Chapter 4

Hydrodynamical evolution of circumbinary disks following central black hole mass loss: shocks above the disk midplane

4.1 Introduction

In Chapter 2, we find that the torques exerted on a gas-embedded IMRI are different from analytical predictions in both strength, direction, and scaling with radius. We also know from planet migration studies that torques can be highly sensitive to various properties of the system, such as the embedded satellite's mass or the properties of the accretion disk (i.e. Duffell 2015b). For this reason, we should expect that our result for the specific case simulated in the previous Chapter is dependent on our assumptions, and a natural next

This section contains text from an article in progress, with the following authors: Derdzinski, A.; Hegde, S.; Haiman, Z.; Macfadyen, A.

step is to investigate how the result (specifically the torques, their evolution, and their detectability in a waveform) may change with our assumptions and choices of parameters.

In the following Chapter, we extend the previous study. Using the same 2-dimensional simulation setup, we simulate the inspiral of intermediate mass ratio binaries at GW rates in the LISA band over an extended parameter space in mass ratio, inspiral rate, BH accretion rate, disk viscosity, and Mach number.

One of the primary sources for the upcoming space-based gravitational wave (GW) detector, LISA, is the mergers of massive black hole (MBHs) between $10^4 - 10^7 M_\odot$ up to redshifts as high as $z \sim 20$. Comprising the smaller end of the MBH mass function, these mergers are expected to occur at higher redshifts and also include MBH 'seeds' which by many merger and accretion events become their more massive counterparts today.

Many of these events in the early universe are expected to occur in gaseous environments, given that the triggering of active galactic nuclei is expected to be tied to galaxy mergers that fuel fresh supplies of gas into the post-merger galactic nucleus (Goulding et al. 2018). Additionally, gas is expected to settle around the binary (Goicovic et al. 2015), and if it cools sufficiently it will form a circumbinary disk (Dotti et al. 2007; Barnes & Hernquist 1996). The evolution of the MBHs in the post merger galaxy proceeds through various phases before becoming a bound binary, and interplay with gas can be crucial for the binary's fate. It is possible that the binary eventually reaches a separation after which gravitational wave emission will dominate the evolution, driving the binary to merge in less than a Hubble time (Mayer 2017), although this depends on the amount of stars and gas in the nucleus. Recent limits from Pulsar Timing Arrays that measure nanoHertz GW background also suggest that MBH binary (MBHB) interaction with their environment may drive them past sub-parsec separations rather quickly, in which case we should expect MBHB mergers to be occurring within less than a Hubble time (e.g. Sampson et al. 2015; Taylor et al. 2016).

In the case that gas is still present around the binary up to merger, the event becomes a LISA source that may also emit coincident electromagnetic (EM) radiation. Gas provides the opportunity for electromagnetic signatures, both as precursor variability (Haiman 2017) or post merger flares that arise from perturbations in a circumbinary disk following the merger of a MBHB. A characteristic EM signature would be valuable for correlating with GW detections of massive black hole mergers by LISA (Barausse et al. 2015b; Baker et al. 2019). In principle, another possibility for the detection of MBHBs even prior to GW detections is finding their EM counterparts.

In the present Chapter we focus on the EM signature produced after the merger of a MBH binary, which is produced as follows. Numerical general relativity calculations predict that the final coalescence of the MBHs will carry away a significant amount of energy from the system. More importantly, during the final stages of coalescence the timescale of GW emission becomes shorter than the dynamical time of the surrounding disk. The energy carried away during this time can amount to several percent of the binary's rest mass and serve as an *impulsive* change in the gravitational potential of the system. The disk perceives this change as an essentially instantaneous reduction in the central black hole mass. Additionally, if the MBHs coalesce asymmetrically, the merger remnant will experience a recoil, or "kick" that can disturb the surrounding disk (Lippai et al. 2008). The importance of post-merger recoil versus mass-energy loss for the dynamics of the circumbinary disk depends on the binary mass ratio and the initial black hole spins (see Berti et al. 2007 for numerical calculations of equal mass mergers, González et al. 2007 for numerical simulations of various mass ratio BHBs, and Herrmann et al. 2007 for spin dynamics). For very small mass ratios ($q \lesssim 0.14$) and high spin parameters, kicks become important. For low spins, the merger is dominated by mass-energy loss. For equal mass ratio kicks are irrelevant due to symmetry. In this work we consider the merger of a non-spinning equal mass binary, thus only considering the effects

of mass-energy loss on the disk.

Both GW-emitted mass-loss and recoil can perturb a surrounding disk, with the tantalizing possibility of producing characteristic signatures associated with a LISA event. The region of the disk that perceives the change in potential as impulsive can exhibit shocks or sound waves that accumulate on timescales of days to weeks, depending on the mass of the central (newly formed) MBH.

Modeling of such post-merger flares has been done primarily with 2-dimensional simulations (discussed further in Section 4.2), but these works do not resolve the vertical structure of the disk. Evolution of shocks above the disk midplane carries critical implications when predicting the resulting emission, since it determines whether or not the emission from shocks is reprocessed under a layer of optically thick gas. It is precisely this concept that we tackle here: gas above the midplane will also respond to the impulsive change in potential, but in a way that is inherently hydrodynamical. This has not been carefully considered in previous work.

The purpose of this Chapter is to explore the post-merger signature in more detail by investigating the response of a disk to a central MBHB merger in the region above the disk midplane. Motivated by previous work, here we investigate the formation and propagation of shocks within the disk's vertical structure. Our motivation is to understand whether the possible shocks are confined to the midplane of the disk, where they are shielded by a layer of optically thick gas, or if they propagate to higher regions of the disk, where they could produce non-thermal radiation. We perform a parameter study of disk thickness versus fractional mass loss in order to gain a more complete understanding of the variety of possible responses.

First, in Section 4.2, we provide a summary of previous work. In Section 4.3, we discuss the disk response in the radial direction in the non-interacting limit, to be used as a reference

for our hydrodynamical calculations. These are presented in Section 4.4, where we introduce our simulation setup and discuss what behavior one should expect in the disk atmosphere. In Section 4.5 we show our results, pointing out the sensitivity to parameters, and conclude with a discussion in Section 4.6.

4.2 Previous work

First, this work is primarily inspired by analytical predictions by Lippai et al. (2008) and Bode et al. (2011), that lay out the foundational framework for such a response. As we will show in Section 3, the initial response is purely dynamical. Once hydrodynamical forces are included, simulations are necessary to predict the disk response. The hydrodynamical response of a circumbinary disk to a binary merger has been investigated by several authors, including Schnittman & Krolik (2008), Krolik (2010), O'Neill et al. (2009), Megevand et al. (2009), Corrales et al. (2010), Rossi et al. (2010), Zanotti et al. (2010), and Rosotti et al. (2012).

Schnittman & Krolik (2008) first discussed a possible electromagnetic afterglow of a circumbinary disk in response to a MBHB merger. Soon after, O'Neill et al. (2009) performed both 3D MHD and 2.5D hydrodynamic simulations in a pseudo-Newtonian point mass potential to investigate the post-merger evolution of a close circumbinary disk. They concluded that shocks produced in response to the mass loss contribute little to the overall emission of the disk, and ultimately the rarefactions produced will result in a dip in luminosity. Works like O'Neill et al. (2009) and Megevand et al. (2009) computing the bremsstrahlung emission, which implicitly assume optically thin emission–this may not be the case in the dense accretion disks expected in AGN. Additionally, they model a relatively small surrounding disk that extends to less than $100R_s$ from the central mass. This limits their analysis to

shorter timescales (due to the short orbital timescales at these radii), and it also neglects the idea that their exists a central cavity in the disk extending to $\sim 100R_s$ due to torques exerted by the pre-existing binary (MacFadyen & Milosavljević 2008).

Work by Rossi et al. (2010) uses SPH simulations to analyze the response of a disk to various orientations of the recoil of the post-merger black hole remnant. Their simulations technically resolve the disk vertical structure (although SPH simulations may have difficulties resolving strong shocks) but they focus primarily on the effect of recoil rather than mass loss. They predict prompt emission signatures in response to various kick angles, as well as a dependence of the corresponding emission to the disk density profile.

Corrales et al. (2010) investigate the response of an extended disk to both recoil and mass loss with hydrodynamic simulations in 2D polar geometry. By considering a larger region of the disk, they predict responses on longer time scales, since the timescale of the disk response is ultimately dictated by the orbital time of the disk. These simulations are grid-based (using FLASH, as we do here) and capture the formation of shocks in response to both mass loss and recoil. They predict the emission from shocked disks with a simple diffusion approximation and conclude that thin disks will experience an increase in luminosity after merger. However, by evolving the vertically-averaged surface density of the disk, such 2-dimensional simulations inherently disregard any detailed dynamics in the vertical disk structure. Their calculation of energy diffusion carries the assumption that the shocks are produced in the midplane of the disk, when in reality, shocks may form and propagate above the mid plane, depositing more heat above the disk midplane and possibly produced non-thermal emission.

In summary, several works have explored this phenomenon, primarily focusing on the radial response of a circumbinary disk. In this work we maintain the simple nature of 2-dimensional simulations (that save computational efficiency and allow for a substantial

parameter study) but instead bring our attention to the effect of including the disk atmosphere.

4.3 The non-interacting limit

Before delving into hydrodynamics, it is useful to understand the dynamical response of a non-interacting disk. To build intuition, consider a single particle in a circular, Keplerian orbit around a point mass. If the central mass is reduced instantaneously, the particle suddenly finds itself in a shallower potential. Its velocity $v_\phi \propto M^{1/2}$ is too fast for its orbit around the reduced central mass, so it finds itself on a new, eccentric orbit. Such an orbit can be described in terms of epicyclic oscillations, or a circular orbit at radius r with radial oscillations that amount to Δr. To first order, the amplitude of the epicyclic motions scales with the change in the potential, and can be approximated by

$$\frac{\Delta r}{r} \sim \frac{\Delta M}{M},$$

where $\Delta M/M$ is the fractional amount of mass loss. These radial oscillations have frequencies that differ for radii that are Δr apart, by the amount

$$\Delta\Omega = \left|\frac{d\Omega}{dr}\right| \Delta r.$$

The response of an orbiting particle will depend on its distance r to the central mass, and particles at different radii will experience epicyclic perturbations that induce a varying Δr. If we consider a 2-dimensional disk of non-interacting particles, the epicyclic response across the disk will produce a range of eccentricities in the particle orbits, eventually producing orbit-crossings, or caustics (see Penoyre & Haiman 2018 for a detailed derivation of caustic

formation).

To demonstrate the dynamical nature of this response, we integrate the orbital trajectories of a disk of non-interacting particles. Starting with an initially uniform distribution of particles on Keplerian orbits, we instantaneously reduce the central mass. This induces a slight eccentricity $e \sim \delta M/M$ to all particles, and over-densities occur within a few orbital times. Figure 4.1 shows different snapshots of three different particle simulations along with histograms of the initially uniform distribution of particles over radii. Several aspects of the post-merger behavior of the non-interacting disks is expected: While all particles experience the same eccentricity, those at smaller radii have higher orbital velocities, and thus the over-densities occur first in the inner radii of the disk before forming at outer radii. For higher amounts of mass loss, higher radial velocities are induced in the surrounding disk. These higher-amplitude oscillations are observed in our particle simulations, particularly in the 10% mass loss run where there exists a significant under-density in the mid-region of the disk.

4.3.1 Vertical response

When incorporating the vertical direction into this model, the problem becomes inherently hydrodynamical because pressure forces will govern the vertically-oriented flow. To understand this, consider a particle at some radius r and some height z above the midplane of the disk. To be in a steady state ($v_r = v_z = 0$), it must move at a (sub-)Keplerian velocity that provides centrifugal support against the radial gravitational acceleration g_r. The velocity is sub-Keplerian to compensate for the pressure forces that are are necessary for initial hydrostatic equilibrium. Pressure forces are also present to fully support the disk vertically against the vertical gravitational acceleration g_z. Just after merger, the particle will experience an instantaneous reduction in both g_r and g_z. The radial response will ini-

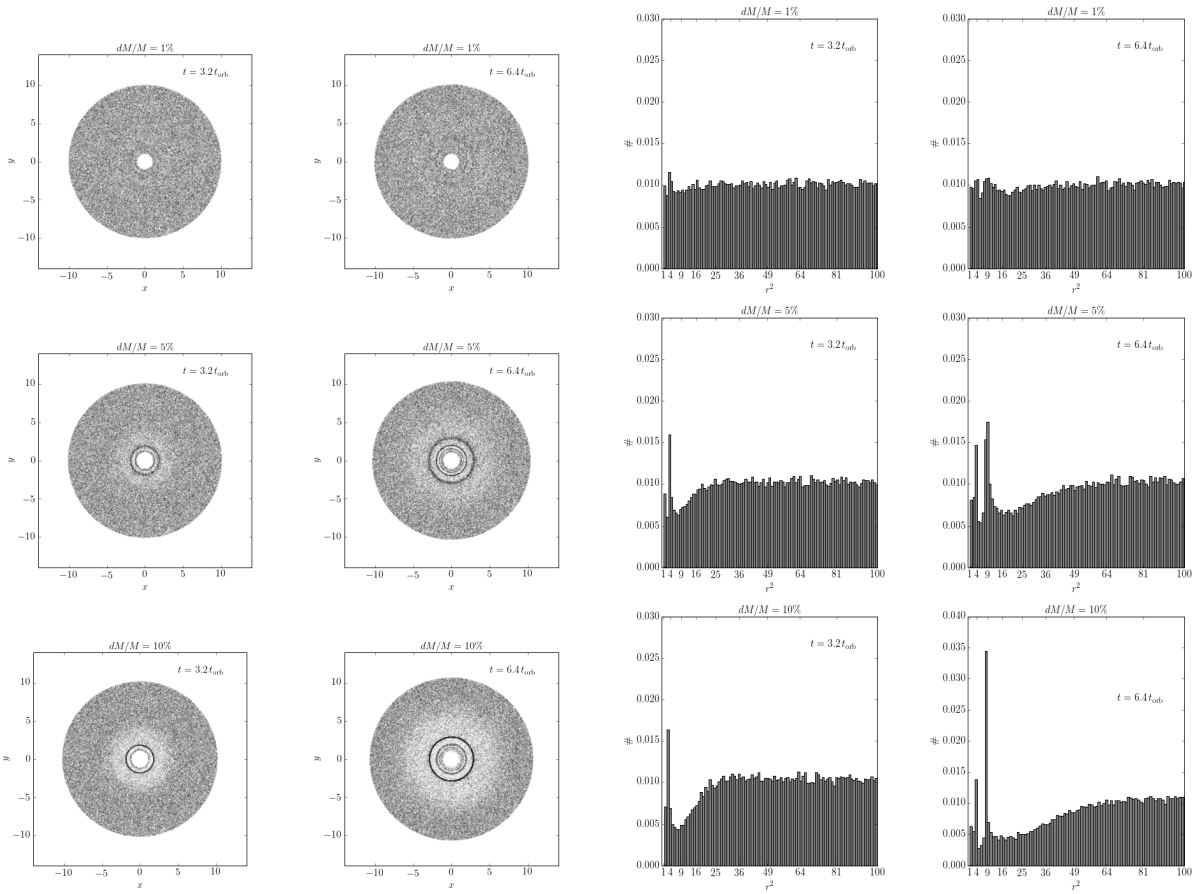

Figure 4.1: Particle simulations show a 2D disk of massless particles, initially uniformly distributed in circular Keplerian orbits, in response to central mass loss. The first and second columns show the disk evolution after $\sim 3t_{\rm orb}$ and $\sim 6t_{\rm orb}$, respectively, where $t_{\rm orb}$ is the orbital time at the inner radius. The histograms on the right show the distribution of particles weighted by r^2, since this is what was initially uniform. The peaks indicate where there lies an over-density of particles at a given radius after a few orbital times. While the over-density in the 1% mass loss case is negligible, both the 5% and 10% mass loss simulations show distinct over-densities at the same approximate radius.

tially be the same as described above — the particle will move outwards before experiencing epicyclic oscillations. However, the particle with also move *upward* initially in response to the change in g_z. The vertical response is primarily dependent on the pressure gradient, and thus the non-interacting approximation is ultimately inapplicable. This is why we turn to hydrodynamical simulations to gain an understanding of the vertical disk response.

The vertical hydrodynamical response to a potential perturbation has been explored in a somewhat analogous case by Coughlin et al. (2018) in the context of failed supernovae[1]. This work described the response of a spherically symmetric system in hydrostatic equilibrium, a case not too different from the disk atmosphere. They find that the outward velocity imparted on layers of the stellar atmosphere is dependent on their distance from the center, and the dominant response is a sound wave that propagates to the surface. At first glance a similar effect may be expected in the atmosphere of an accretion disk. However, one crucial difference between the spherical case and the cylindrical one is the difference in gravitational potential and orientation of the system. In a stellar atmosphere, the response of the gas is dependent on the radius of the star (scaling with the gravitational potential, which scales as $\Phi_r(r) \propto r^{-1}$), and gas deeper in the atmosphere experiences a stronger perturbation. In our accretion disk, however, gas higher above the midplane feels a stronger component of the vertical gravitational force (because $\Phi_z \sim z$), and hence should respond more dramatically to the change in potential than the gas closer to the midplane. In the following section we describe our simulation setup, aimed at investigating how this response takes place.

[1]In this case instantaneous massloss is driven by neutrino emission from the core.

4.4 Hydrodynamics

4.4.1 Simulation setup

We perform simulations in 2D cylindrical geometry, assuming axisymmetry along the ϕ axis and resolving the $r - z$ plane of the disk, including the normal velocity component. We use version 4.2.2 of the hydrodynamics simulation code FLASH (Fryxell et al. 2000) with the unsplit PPM hydrodynamic solver. FLASH is a higher-order Godunov-type code with capabilities of adaptive mesh refinement. The unsplit hydrodynamic solver, written by Lee (2013), comes with a variety of runtime parameters. For those interested in these details, we use a 3rd order PPM method for data reconstruction with the HLLC Riemann solver. We ensure that angular momentum is conserved during evolution by setting the parameter `conserveAngMom = .true.`. We also turn on the switch `grav_half_update = .true.`, which allows the code to solve for the gravitational acceleration at half time steps during evolution, providing better accuracy with the coupling of hydrodynamics and gravity.

The simulation domain extends from $1 \leq r/r_0 \leq 10$ and $0 \leq z/r_0 \leq h(r_{\rm max})$, where h is the disk scale height approximated by $h \approx c_s(r_0)\, r$, $c_s(r)$ is the sound speed, and r_0 is an arbitrary distance unit. It should be noted that the evolution of the disk in response to black hole mass loss is *self-similar*, meaning that there are no pre-imposed relevant length scales. Rather, given a black hole mass, one can scale the simulation length and time to physical units. A length scale pertinent to this study, for example, would be just outside the inner radius—or cavity edge—of the circumbinary disk. For example, given a black hole mass of $M_{\rm BH} = 10^6 M_\odot$, the inner cavity of the disk would be at approximately 100 Schwarzschild radii, or $r_0 = 200\, GM/c^2 \approx 3 \times 10^{13}$ cm. With this scaling, the orbital timescale at the inner radius is $t_0 = 2\pi r_0 / v_\phi(r_0) \approx 1$ day. For the remainder of this study we show distance in

arbitrary units of r_0, and we scale the simulation time to the orbital time $t_{\rm orb}$ at the inner boundary.

We model a disk with an aspect ratio h/r that is approximately constant with radius (in the thin disk limit). The vertical domain extends to include one scale height at the outer boundary, which corresponds to 10 scale heights at the inner radius. We vary h/r from 0.01 to 0.2.

Our resolution varies depending on the disk thickness, but in the lowest resolution case our domain contains $[r, z] = [50, 20]$ blocks, where each block contains 8×8 cells, corresponding to radial and vertical resolution of $\Delta r = 0.0225 r_0$ and $\Delta z \leq 0.0625\, h$. Note that, once shocks have formed, their strength (or maximum density) is dependent on the resolution. In analyzing the propagation of over-densities and shocks, we performed resolution tests (running test simulations with $60 - 80$ blocks in r) to ensure that their positions were unchanged with higher resolution.

We are concerned with the response of the disk on dynamical timescales ($t_{\rm dyn} \sim 1/\Omega$), which is much shorter than a viscous time ($t_\nu \sim r^2/\nu$ where ν is the kinematic viscosity). For this reason we do not include viscosity in our accretion disk model, since we do not expect the disk to accrete significantly on such short timescales.

4.4.1.1 Equation of State

We assume an ideal gas and locally isothermal EOS, such that the pressure is solved by

$$p = c_s^2 \rho, \tag{4.1}$$

where the sound speed $c_s = \sqrt{\frac{k_b}{\mu m_H} T(r)}$ can be a function of r, but remains constant in time. With this formalism, the internal energy and temperature of the gas are held fixed in time.

In practice, compressions in the disk will change its internal energy. By setting these values back to the initial values at every time step, we are assuming that any increase in internal energy is effectively radiated immediately. Additionally we are assuming that any *decrease* in internal energy is immediately re-heated. An isothermal equation of state is analogous to the assumption of very short cooling timescales. For comparison, future work will explore disk response with an adiabatic equation of state, as a limit of very long cooling timescales.

4.4.1.2 Initial Conditions

We solve for an initial disk model from the fluid momentum equations in cylindrical geometry as follows: The radial and vertical momentum equations for a zero-viscosity fluid in cylindrical coordinates are

$$\begin{aligned} \frac{\partial v_r}{\partial t} + v_r\frac{\partial v_r}{\partial r} + \frac{v_\phi}{r}\frac{\partial v_r}{\partial \phi} + v_z\frac{\partial v_r}{\partial z} - \frac{v_\phi^2}{r} &= -\frac{1}{\rho}\frac{\partial p}{\partial r} - \frac{\partial \Phi}{\partial r}, \\ \frac{\partial v_z}{\partial t} + v_r\frac{\partial v_z}{\partial r} + \frac{v_\phi}{r}\frac{\partial v_z}{\partial \phi} + v_z\frac{\partial v_z}{\partial z} &= -\frac{1}{\rho}\frac{\partial p}{\partial z} - \frac{\partial \Phi}{\partial z}, \end{aligned} \tag{4.2}$$

where the gravitational potential Φ is that of a point mass at the origin:

$$\Phi = -\frac{GM}{\sqrt{r^2+z^2}}, \tag{4.3}$$

since we are interested in the final moments of binary coalescence during which the black holes are sufficiently close together. Additionally we are interested in the dynamics of the disk beyond the inner cavity, at which relativistic effects are unimportant.

Setting axisymmetry ($\partial_\phi = 0$) and invariance in time ($\partial_t = 0$), and setting $v_r = v_z = 0$, we get the condition for centrifugal balance:

$$-\frac{v_\phi^2}{r} = -\frac{1}{\rho}\frac{\partial p}{\partial r} - \frac{GMr}{(r^2+z^2)^{3/2}}, \tag{4.4}$$

Similarly, the $\hat{z}$-momentum equation gives the condition for vertical balance ($v_z = 0$) i.e. hydrostatic equilibrium,

$$\frac{1}{\rho}\frac{\partial p}{\partial z} = -\frac{GMz}{(r^2+z^2)^{3/2}}. \tag{4.5}$$

Using the isothermal energy equation $p = c_s^2\rho$, and assuming that c_s is not a function of z, we can integrate Eq (6) to get

$$\rho(r,z) = \rho_0(r)\exp\left[\frac{GM}{c_s^2(r)}\left(\frac{1}{(r^2+z^2)^{1/2}} - \frac{1}{r}\right)\right],$$

where $\rho_0(r)$ can be some function of r and we choose $\rho_0(r) = \rho_0 r^{-1}$. We choose a sound speed profile given by $c_s = c_s(r_0)r^{-1/2}$, which corresponds to a temperature profile of the disk $T \propto r^{-1}$ that is independent of z. These conditions create a disk of roughly constant surface density $\Sigma(r)$ (in the thin $h \ll r$ limit), a model that is primarily motivated by comparison to previous work. The initial density profile becomes

$$\rho(r,z) = \rho_0 r^{-1}\exp\left[\frac{GM}{c_s(r_0)^2}\left(\frac{r}{(r^2+z^2)^{1/2}} - 1\right)\right], \tag{4.6}$$

and the initial pressure profile is given by

$$p(r,z) = c_s(r_0)^2\, r^{-1}\rho(r,z). \tag{4.7}$$

This gives us a sub-Keplerian rotational velocity

$$v_\phi(r,z) = \left[\frac{GM}{(r^2+z^2)^{1/2}} - \frac{2\,c_s(r_0)^2}{r}\right]^{1/2}. \tag{4.8}$$

4.4.1.3 Boundary Conditions

Following the assumption of hydrostatic equilibrium in our initial conditions, we set fixed boundary conditions at the upper boundary to ensure initial hydrostatic equilibrium. A typical "outflow", or zero-gradient, boundary condition is insufficient for stability because pressure gradients are essential for supporting the disk against the vertical component of the gravitational acceleration. Finding a stable inner radial boundary condition proved to be numerically challenging given that the disk model is prone to numerical oscillations. We fix the inner radial boundary cells to the initial density, pressure, temperature, and internal energy of a steady disk configuration, and we impose a diode condition such that gas can flow out but not in the domain in order to avoid artificially feeding gas into the disk. Given the symmetry of the disk across the midplane, it is unnecessary to resolve both quadrants, thus our bottom boundary condition is reflecting.

4.4.2 The epicyclic Mach number

While it is the oscillations from the non-interacting approximation that cause compressions in the disk, ultimately pressure forces will govern the flow. To compare various simulations it is useful to parameterize the scale height of the disk—a characteristic of how pressure-dominated it is—and the amount of mass loss. It is useful to parametrize simulations with the epicyclic Mach number M_e, first introduced by Bode et al. (2011), given by the ratio of the induced radial velocity to the sound speed. It is essentially a Mach number for radial flow:

$$M_e = \frac{v_{\rm epicycle}}{c_s} \sim \frac{v_{\rm orb}\,\epsilon_{\rm m}}{v_{\rm orb}\,h/r} \approx \frac{\epsilon_{\rm m}}{h/r} \tag{4.9}$$

This parameter provides an indication of how the disk will behave once the perturbations are induced. Given an impulsive change in potential, epicyclic oscillations in the surrounding

gaseous disk will create compressions that travel radially outward. When $M_e \gg 1$, these compressions travel significantly faster than the sound speed of the disk and we expect them to produce shocks. For $M_e \ll 1$, perturbations evolve acoustically. Note that M_e can depend on r, and so the dynamics of the disk can change with radius. For our particular disk model M_e is roughly constant, despite the slight sub-Keplerian radial dependence in v_ϕ.

To investigate the varying regimes of disk response we explore the M_e parameter space by simulating disks of various aspect ratios (h/r = 0.01, 0.05, 0.1, 0.2) in response to different amounts of mass loss ($\Delta M/M$ = 0.01, 0.05, 0.1). In addition to varying the amounts of mass loss $\Delta M/M$, we vary the normalization of the sound speed $c_s(r_0)$, which corresponds to the temperature profile of the disk and sets the disk aspect ratio. For small h/r,

$$\frac{h}{r} \sim \frac{c_s}{v_\phi} \sim c_s(r_0) = \frac{1}{\mathcal{M}}.$$

The Mach number $\mathcal{M}$ tells us how supersonic (and cold) the disk is. Thinner disks are colder and are characterized by a higher Mach number, while thicker disks are correspondingly hotter.

A table of our simulation suite is shown in Table 4.1, with a brief reference to the observed disk response.

4.5 Results

In this section we describe the range of disk responses as they vary with disk temperature, first analyzing the vertically-integrated radial response, as this can be compared to the particle limit and 1-D hydrodynamical simulations. We then discuss the evolution in the vertical region.

h/r	$\Delta M/M$	M_e	Post-merger characteristics
0.01	5%	5	concentric shocks
0.05	1%	0.2	acoustic waves
	5%	1	leading shock
	10%	2	leading shock
0.10	1%	0.1	acoustic waves
	5%	0.5	over-density + rarefaction
	10%	1	leading shock + rarefaction
0.20	1%	0.05	negligible
	5%	0.25	under-density
	10%	0.5	under-density

Table 4.1: The suite of simulations spanning disk aspect ratios (h/r) and fractional mass loss ($\Delta M/M$). The epicyclic Mach number M_e approximates the post-mass-loss behavior of the disk. For $M_e > 1$, we observe the formation of strong over-densities and shocks. In contrast, for $M_e < 1$ disks are perturbed acoustically, producing small over-densities and rarefactions.

4.5.1 Radial response

To focus on the radial response, we can integrate over the vertical structure of the disk to obtain the surface density

$$\Sigma(r) = \int_{-\infty}^{\infty} \rho(r, z) dz,$$

in order to analyze the strength of the over-densities. This can be compared directly to the non-interacting limit demonstrated in our particle simulations.

The epicyclic Mach number provides a good approximation for the radial disk response. Similar to Bode et al. (2011), we find an array of possible disk responses that are particularly dependent on the disk thickness.

The coldest disk in the set of simulations has an aspect ratio of $h/r = 0.01$, corresponding to a Mach number $\mathcal{M} = 100$. We consider this our fiducial case, since its response should be most comparable to that of the non-interacting disk. Figure 4.2 shows snapshots of the

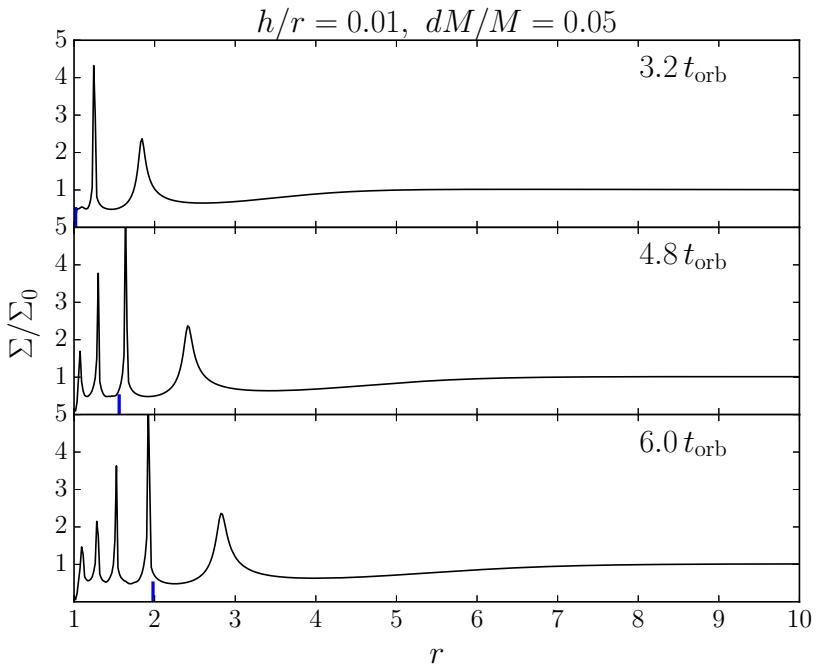

Figure 4.2: Surface density evolution of an $h/r = 0.01$ disk after 5% mass loss. Concentric over-densities develop on orbital timescales and immediately turn into shocks. The blue lines indicate the location of the most orbit-crossings found in the particle simulations. After a few orbits, the location of the first shock follows that of the non-interacting disk.

surface density evolution. The blue lines indicate the location of the highest over-densities produced in the particle simulations. Comparing to the hydrodynamical disk, we find that the location of the shocks is quite similar. As expected with a high epicyclic Mach number of $M_e \sim 5$, the over-densities almost immediately become shocks. We expect that for higher mass loss more energy would go into the front-most compression, as this is the behavior we observe in other disks.

Figure 4.3 shows the vertically-integrated evolution of disks with different aspect ratios in response to 1%, 5%, and 10% mass loss. Ranging from the lowest M_e (lower left panel) to the highest M_e (upper right panel), we see a range of responses: colder disks produce concentric shocks, while hotter disks are perturbed acoustically. The behavior in hotter

disks ($M_e \lesssim 1$) deviates from the concentric shock evolution in the non-interacting disk, due to non-negligible pressure forces. While thinner, colder disks tend to quickly produce shocks, thicker disks are perturbed acoustically. These disks do not form significant over-densities because pressure forces tend to diminish the compressions. Rather, a single wave steepens into a shock that travels at the sound speed. In general simulations of higher mass loss produce the strongest shocks, but also the deepest rarefactions (under-densities proceeding the shock).

An interesting feature found in our simulations is that shocks and over-densities are *dissipated* when compared to 1D simulations such as that in Bode et al. (2011). When resolving the vertical structure of the disk, the radial response is 'smoothed,', especially when compared to the non-interacting particle integration (which, in fact, produces caustics of infinite density, see Penoyre & Haiman 2018).

4.5.2 Shocks above the midplane

We have resolved the vertical disk structure which allows us to analyze the amount of shocked gas above the disk midplane, a characteristic that is important for understanding the energy dissipation and ultimately the corresponding emission. We find that the shocks, when present, form and propagate near the surface of the disk. Density contours shown in Figure 4.4 clearly indicate that over-densities occur up to $\sim$1 scale height of the disk.

For colder disks (with higher M_e) the vertical response of the disk is almost identical to the radial response for all z. Intuitively this is not surprising given our simulation assumptions: a vertically isothermal disk has a sound speed that is constant in z, so any hydrodynamical response may not vary significantly as a function of scale height. However, a notable difference arises for disks with higher sound speeds (lower M_e). As shown by the bottom panels in Figure 4.4, the vertical shock begins to curve. These thicker disks also

show much lower overall densities, as indicated by the varying colorbar scalings.

One crude approximation for the strength of a shock can be obtained by looking at its density as a function of scale height. This is shown in Figure 4.5, where we show the vertical density profile near the radius of the leading shock, normalized to the initial density. We see that the density increase (found at the location of the maximum surface density) persists up above the midplane, peaking near the disk edge ($z \sim h$). Notice, also, that for the thinner, colder disk ($h/r = 0.05$) the density contrast is nearly twice as extreme as in the thicker disk ($h/r = 0.1$), suggesting stronger shocks for colder disks.

Because our simulations assume an isothermal gas, any increase in the internal energy of the gas due to compression is discarded immediately, in order to keep the gas at a constant temperature. (Conversely, any decrease in internal energy in cases where the gas expands is "re-heated" back to the initial temperature profile). This means we cannot trace how the energy deposited by shocks affects the dynamics of the disk. We can, however, trace this quantity, change in internal energy ΔE_i, over time. This measurement provides a measure of the strength of the shocks, as we show in Figure 4.6. The most prominent feature of this diagnostic is that energy is deposited by the shocks above a scale height of the disk.

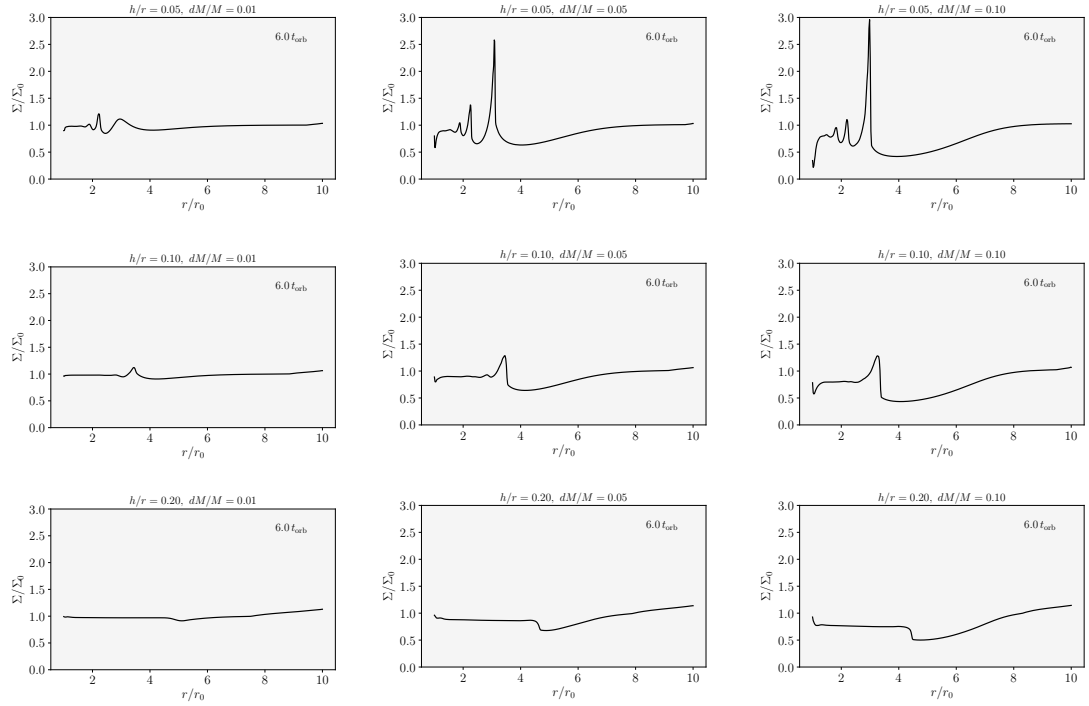

Figure 4.3: Surface density evolution for the suite space of simulations, showing the variety of hydrodynamical responses to black hole mass loss. In the presence of shocks, we have marked the location of the over-densities produced in the particle simulations for comparison. In the highest Mach number simulation, corresponding to the top right corner, a strong shock is produced within a few orbital times. In the lowest Mach number simulation, corresponding to the lower left panel, the effects of mass loss are negligible, particularly for hotter, more pressure-dominated disks. While the colder disks have an inherently lower sound speed and hence are easier to shock, hotter disks tend to produce under-densities in response to mass loss.

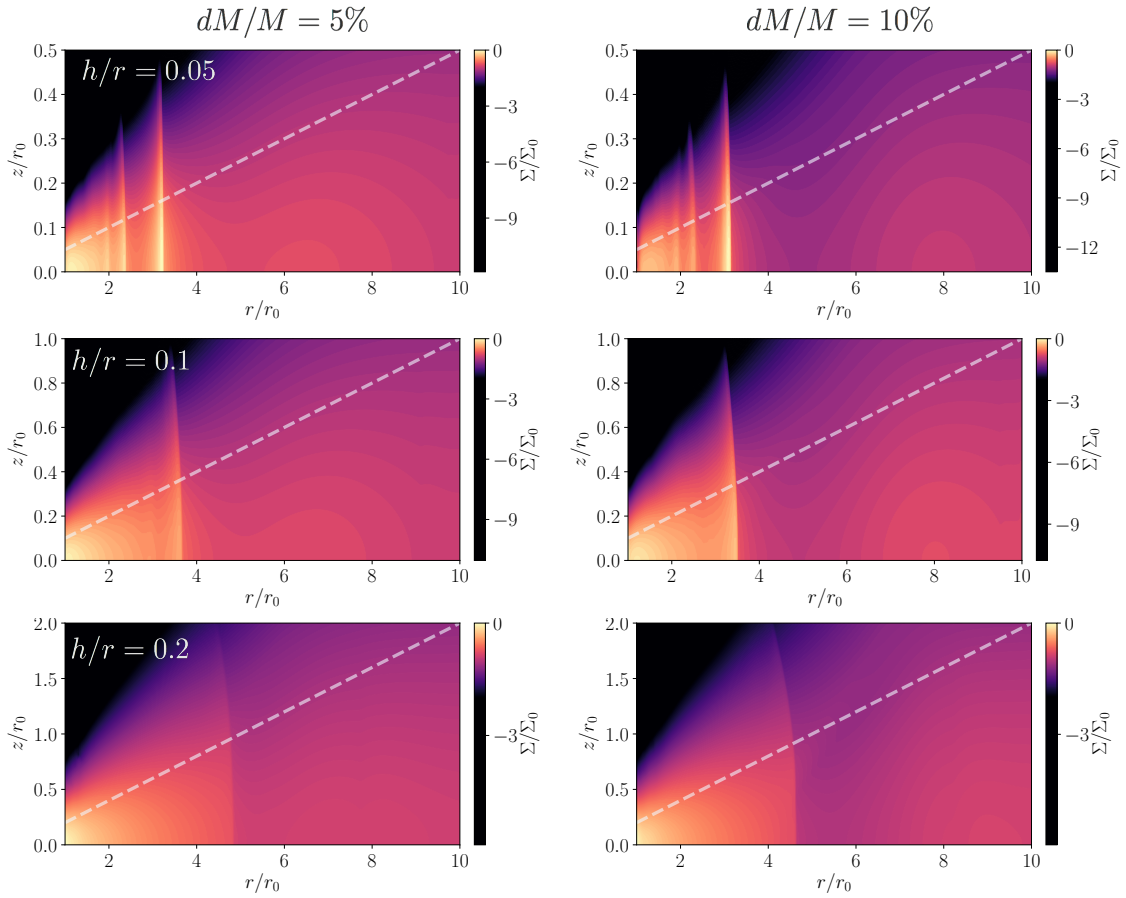

Figure 4.4: A variety of post-merger disk behaviors depending on disk thicknesses (corresponding to $h/r = 0.05, 0.1, 0.2$). Each snapshot shows the surface density of the disk at a post-merger time of $t = 6\,t_{\rm orb}$. Note the difference z axis for each run. The dashed line indicates a scale height. Colder, thinner disks produce concentric shocks throughout the vertical structure of the disk. Hotter disks, however, only produce small over-densities. For higher mass loss, the shocks and over-densities—as well as the under-densities proceeding the shocks–are more prominent.

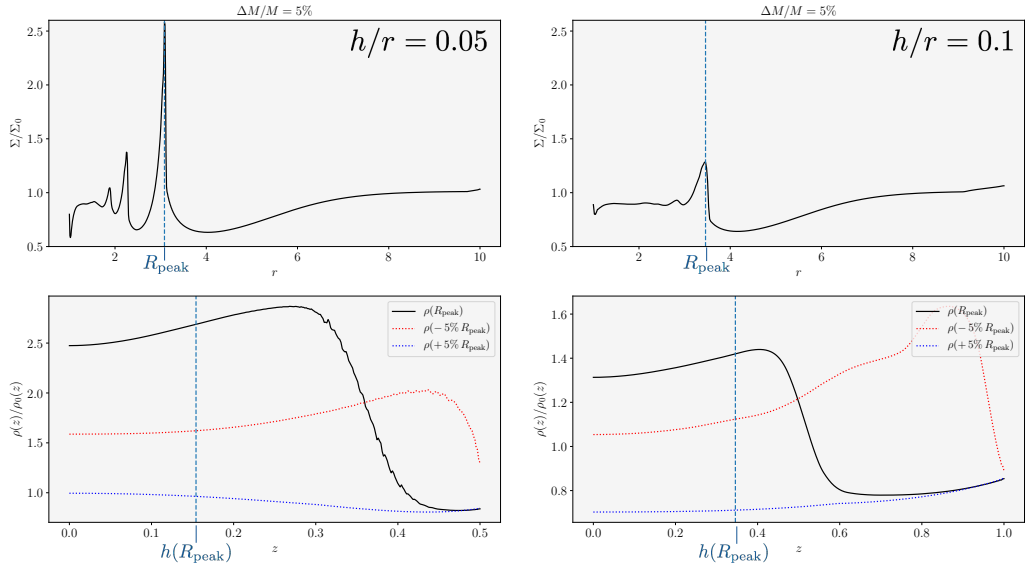

Figure 4.5: *Top panels:* Surface density profiles for reference, to show the radius of the peak surface density. *Bottom panels:* The vertical profiles of the normalized density near the radius of the shocked gas for $h/r = 0.05$ (*left*) and $h/r = 0.1$ (*right*), each at $6t_{\rm orb}$ following 5% mass loss. The red and blue dotted lines correspond to the vertical density profiles just behind and in front of the shocked gas, respectively. Rather than being confined to the midplane, the high-density gas occupies a significant portion of the vertical disk structure. In both cases, the over-density ($\rho/\rho_0 > 1$) is present over a scale height, suggesting strong shocks near the disk edge.

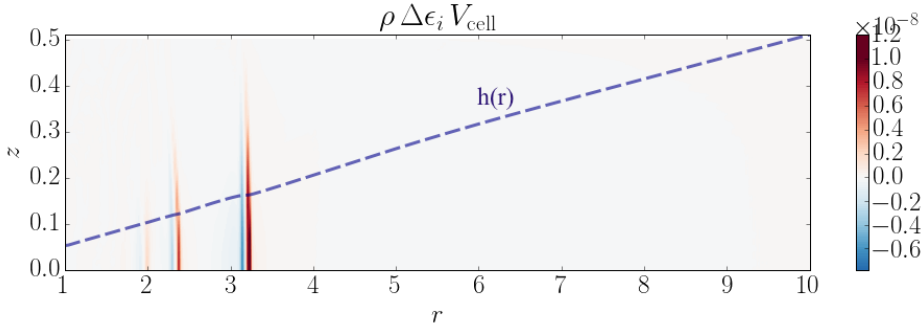

Figure 4.6: The effective energy deposited by the shocks in a single timestep for the $h/r = 0.05$ disk with $dM/M = 5\%$ after $t = 6t_{\rm orb}$ (to be compared with the top left panel of Figure 4.4). In the limit of an isothermal gas, any change in the internal energy is effectively radiated/re-heated immediately to maintain the initial temperature profile. This change in specific internal energy, $\Delta\epsilon_i$, is multiplied by the density ρ and the cell volume ΔV to show a total internal energy. Notice that most of the energy is deposited by the leading shock, and that this deposition is extended significantly above the disk midplane.

4.6 Conclusions and discussion

In this work we investigate the response of a circumbinary disk to a MBHB merger, specifically due to the reduction in mass of the central post-merger MBH. We perform axisymmetric simulations that resolve the gas structure above the disk midplane, studying the possibility of shock production near the disk surface. First we compare our results to previous studies that analyze the radial response in the disk. We find general agreement with disk response as a function of gas temperature (or Mach number): colder disks tend to produce strong shocks, while hotter disks respond with sound wave perturbations that later steepen into shocks. In including the vertical disk component, we find that radial response can become dissipated as compared to 1D or 2D polar calculations, meaning that the integrated density is less radially confined.

Resolving gas dynamics above the disk midplane is important for understanding the complete picture of disk response. We have shown that shocks can form above the disk midplane, and propagate outward radially. This response is highly dictated by the disk temperature. Sufficiently cool, thinner disks ($h/r \lesssim 0.05$) show the formation of strong shocks and density compressions that persist up to the disk scale height. Hotter, thicker disks show deviations from the radial solution above the disk midplane. These calculations are in the isothermal limit. To fully understand the range of possible responses, one must run adiabatic simulations that follow how energy from such shocks affects the dynamics of the disk.

A quick estimate of the instantaneous energy deposited by these shocks (in the cold disk limit) suggests that these sources may be responsible for producing bright emission following the merger on a timescale of days (assuming a central mass of $M_{\rm BH} \approx 10^6 M_\odot$). Hotter, thicker disks ($h/r > 0.1$), however, show strong density rarefactions, which suggests that

they might *dim* after merger, due to the overall radial expansion of the disk. While previous work has assumed that the radiation produced from these shocks is significantly reprocessed through the disk, we have shown that this assumption may not be valid for thin disks.

Overall, we believe that the emission from such a system will consist of both non-thermal and thermalized emission, to a degree that depends on the disk thickness. For example, while hotter disks do not experience strong shocks in response to the merger, their inherently lower densities may allow for emission from even weak shocks to produce non-thermal emission. Conversely, thinner disks may produce stronger shocks, but a large portion of shocks are within an inherently denser disk, so the resultant emission signature may be reprocessed through a blanket of denser gas. A plan for follow-up work is to calculate in more detail the fraction of energy dissipated above the disk photosphere for various disk temperatures. To predict a realistic emission signature from this disks will require a more sophisticated radiation transfer calculation, which we leave to future work.

The variety of hydrodynamical responses to the central black hole merger suggests a wide range of possible observational signatures, prompting us to revisit the range of EM counterparts for merging MBHBs, as well as how we search for them. One hope is that, provided we understand this range of responses, detecting a post-merger counterpart will serve as a prove of the disk in which the source resides - ultimately teaching us about AGN environments.

Chapter 5

Conclusion

A common thread among each chapter in this Dissertation is the aim to predict characteristic signatures produced by accretion disks around coalescing massive black hole systems. As the field of low-frequency GW astronomy emerges, we expect to detect signals from merging MBH systems in the near future. Many of these systems may be embedded in gas disks which can alter their evolution. The purpose of this work is to understand how a gas disk responds to a merging MBH binary, with the underlying goal that we can use this understanding to interpret and compliment future GW detections. Below we summarize our key findings and discuss ongoing and future work.

Through the use of hydrodynamical simulations, in Chapters 2 and 3 we study the perturbations induced in a gas disk with an embedded intermediate mass ratio inspiral. We confirm analytical estimates of the detectability of gas torques in a GW waveform (Derdzinski et al. 2019), but we show that these torques may also arise as an *outspiral* rather than an inspiral, and that this regime of migration torque is sensitive to the gas dynamics close to the migrating BH. This work was the first to measure torques directly throughout a GW-driven inspiral in this mass ratio regime. Building upon this work, we explore the sensitivity of

this result to change in the secondary BH mass, disk parameters, and accretion efficiency. We find that the strength, direction, and variability of torques exerted on the BH change dramatically with small changes in BH mass, viscosity, and Mach number. These torques can evolve uniquely throughout the binary lifetime, and the detectability of the deviation in the waveform produced by gas will depend on combinations of these parameters.

All of this work utilizes simple numerical models that neglect certain realistic physical processes. For example, in the case that torques are sensitive to the accretion rate of the BH, they will also certainly be affected by accretion feedback. While simple models are key for highlighting the underlying physics at play, making *realistic* predictions for what LISA will detect will require more sophisticated modeling, such as the inclusion of radiation pressure, or resolving the 3-dimensional flow around the embedded BH. This work comprises the foundation of future models that incorporate more sophisticated physics.

Moreover, these predictions focus on the intermediate mass ratio regime, but this is only a subset of the possible parameter space. Not all binaries will demonstrate significant gas imprint in their waveform as it arises in the LISA data. Future work should investigate for what range of parameters the gas imprint will be relevant (i.e. detectable) and interesting (i.e. uniquely traceable to disk properties).

In Chapter 4 we explore an entirely different way to probe accretion disks: through electromagnetic emission after the binary merger. We explore the case of mass loss due to the final stage of GW emission from a merging binary and its affect on a circumbinary disk. Our critical finding is that when resolving the gas structure above the disk midplane, we find that shocks can be produced in effectively all vertical regions of the disk. We confirm that this effect is dependent on disk temperature, with a particularly interesting implication: while hotter disks may not experience the strongest shocks, they may be able to release non-thermal emission due to their intrinsically lower densities. There are several follow-up

extensions to this work that are currently underway. The first is to connect the findings of shock production above the disk midplane to predict a characteristic light-curve, and to analyze what fraction of the emission is produced above the disk photosphere. The second is to explore the limit that the disk is not isothermal, but instead reacts to internal shocks adiabatically or with a more realistic equation of state. The goal is to bracket the range of possible responses that may occur, to fully appreciate the range of possible EM counterparts.

Making predictions for signatures of accretion disks around coalescing black hole binaries is an endeavor that requires modeling gas dynamics around accreting binary systems, which entails a range of complex physical processes. The hope is that, by building a foundation of possible gas-induced effects, we can be prepared to detect and interpret evidence of these interactions as they arise (either in GW deviations, or in interpreting AGN flares). A tantalizing prospect of the variety of manifestations, both in EM emission from a circumbinary disk and in the sensitivity of migration torques on embedded IMRIs, is that perhaps one can use uniqueness to trace back detections to underlying disk properties.

Bibliography

2007, Numerical Methods in Astrophysics: An Introduction

Abbott, B. P., Abbott, R., Abbott, T. D., Abernathy, M. R., Acernese, F., Ackley, K., Adams, C., Adams, T., Addesso, P., Adhikari, R. X., & et al. 2016, Physical Review Letters, 116, 061102

Abramowicz, M. A., Czerny, B., Lasota, J. P., & Szuszkiewicz, E. 1988, ApJ, 332, 646

Amaro-Seoane, P. 2018, ArXiv e-prints

Amaro-Seoane, P., Audley, H., Babak, S., Baker, J., Barausse, E., Bender, P., Berti, E., Binetruy, P., Born, M., Bortoluzzi, D., Camp, J., Caprini, C., Cardoso, V., Colpi, M., Conklin, J., Cornish, N., Cutler, C., Danzmann, K., Dolesi, R., Ferraioli, L., Ferroni, V., Fitzsimons, E., Gair, J., Gesa Bote, L., Giardini, D., Gibert, F., Grimani, C., Halloin, H., Heinzel, G., Hertog, T., Hewitson, M., Holley-Bockelmann, K., Hollington, D., Hueller, M., Inchauspe, H., Jetzer, P., Karnesis, N., Killow, C., Klein, A., Klipstein, B., Korsakova, N., Larson, S. L., Livas, J., Lloro, I., Man, N., Mance, D., Martino, J., Mateos, I., McKenzie, K., McWilliams, S. T., Miller, C., Mueller, G., Nardini, G., Nelemans, G., Nofrarias, M., Petiteau, A., Pivato, P., Plagnol, E., Porter, E., Reiche, J., Robertson, D., Robertson, N., Rossi, E., Russano, G., Schutz, B., Sesana, A., Shoemaker, D., Slutsky, J., Sopuerta, C. F., Sumner, T., Tamanini, N., Thorpe, I., Troebs, M., Vallisneri, M., Vecchio, A., Vetrugno, D., Vitale, S., Volonteri, M., Wanner, G., Ward, H., Wass, P., Weber, W., Ziemer, J., & Zweifel, P. 2017, ArXiv e-prints

Amaro-Seoane, P., Gair, J. R., Freitag, M., Miller, M. C., Mandel, I., Cutler, C. J., & Babak, S. 2007, Classical and Quantum Gravity, 24, R113

Armano, M., Audley, H., Auger, G., Baird, J. T., Binetruy, P., Born, M., Bortoluzzi, D., Brandt, N., Bursi, A., Caleno, M., Cavalleri, A., Cesarini, A., Cruise, M., Danzmann, K., de Deus Silva, M., Diepholz, I., Dolesi, R., Dunbar, N., Ferraioli, L., Ferroni, V., Fitzsimons, E. D., Flatscher, R., Freschi, M., Gallegos, J., García Marirrodriga, C., Gerndt, R., Gesa, L., Gibert, F., Giardini, D., Giusteri, R., Grimani, C., Grzymisch, J., Harrison, I., Heinzel, G., Hewitson, M., Hollington, D., Hueller, M., Huesler, J., Inchauspé, H., Jennrich, O., Jetzer, P., Johlander, B., Karnesis, N., Kaune, B., Killow, C. J., Korsakova,

N., Lloro, I., Liu, L., Maarschalkerweerd, R., Madden, S., Mance, D., Martín, V., Martin-Polo, L., Martino, J., Martin-Porqueras, F., Mateos, I., McNamara, P. W., Mendes, J., Mendes, L., Moroni, A., Nofrarias, M., Paczkowski, S., Perreur-Lloyd, M., Petiteau, A., Pivato, P., Plagnol, E., Prat, P., Ragnit, U., Ramos-Castro, J., Reiche, J., Romera Perez, J. A., Robertson, D. I., Rozemeijer, H., Rivas, F., Russano, G., Sarra, P., Schleicher, A., Slutsky, J., Sopuerta, C., Sumner, T. J., Texier, D., Thorpe, J. I., Trenkel, C., Vetrugno, D., Vitale, S., Wanner, G., Ward, H., Wass, P. J., Wealthy, D., Weber, W. J., Wittchen, A., Zanoni, C., Ziegler, T., & Zweifel, P. 2017, ArXiv e-prints

Arzoumanian, Z., Baker, P. T., Brazier, A., Burke-Spolaor, S., Chamberlin, S. J., Chatterjee, S., Christy, B., Cordes, J. M., Cornish, N. J., Crawford, F., Thankful Cromartie, H., Crowter, K., DeCesar, M., Demorest, P. B., Dolch, T., Ellis, J. A., Ferdman, R. D., Ferrara, E., Folkner, W. M., Fonseca, E., Garver-Daniels, N., Gentile, P. A., Haas, R., Hazboun, J. S., Huerta, E. A., Islo, K., Jones, G., Jones, M. L., Kaplan, D. L., Kaspi, V. M., Lam, M. T., Lazio, T. J. W., Levin, L., Lommen, A. N., Lorimer, D. R., Luo, J., Lynch, R. S., Madison, D. R., McLaughlin, M. A., McWilliams, S. T., Mingarelli, C. M. F., Ng, C., Nice, D. J., Park, R. S., Pennucci, T. T., Pol, N. S., Ransom, S. M., Ray, P. S., Rasskazov, A., Siemens, X., Simon, J., Spiewak, R., Stairs, I. H., Stinebring, D. R., Stovall, K., Swiggum, J., Taylor, S. R., Vallisneri, M., van Haasteren, R., Vigeland , S., Zhu, W. W., & NANOGrav Collaboration. 2018, ApJ, 859, 47

Babak, S., Gair, J., Sesana, A., Barausse, E., Sopuerta, C. F., Berry, C. P. L., Berti, E., Amaro-Seoane, P., Petiteau, A., & Klein, A. 2017, Phys. Rev. D, 95, 103012

Babak, S., Petiteau, A., Sesana, A., Brem, P., Rosado, P. A., Taylor, S. R., Lassus, A., Hessels, J. W. T., Bassa, C. G., Burgay, M., Caballero, R. N., Champion, D. J., Cognard, I., Desvignes, G., Gair, J. R., Guillemot, L., Janssen, G. H., Karuppusamy, R., Kramer, M., Lazarus, P., Lee, K. J., Lentati, L., Liu, K., Mingarelli, C. M. F., Osłowski, S., Perrodin, D., Possenti, A., Purver, M. B., Sanidas, S., Smits, R., Stappers, B., Theureau, G., Tiburzi, C., van Haasteren, R., Vecchio, A., & Verbiest, J. P. W. 2016, MNRAS, 455, 1665

Baker, J., Haiman, Z., Rossi, E. M., Berger, E., Brandt, N., Breedt, E., Breivik, K., Charisi, M., Derdzinski, A., D'Orazio, D. J., Ford, S., Greene, J. E., Hill, J. C., Holley-Bockelmann, K., Key, J. S., Kocsis, B., Kupfer, T., Madau, P., Marsh, T., McKernan, B., McWilliams, S. T., Natarajan, P., Nissanke, S., Noble, S., Phinney, E. S., Ramsay, G., Schnittman, J., Sesana, A., Shoemaker, D., Stone, N., Toonen, S., Trakhtenbrot, B., Vikhlinin, A., & Volonteri, M. 2019, BAAS, 51, 123

Balbus, S. A. & Hawley, J. F. 1991, ApJ, 376, 214

Barausse, E., Bellovary, J., Berti, E., Holley-Bockelmann, K., Farris, B., Sathyaprakash, B., & Sesana, A. 2015a, in Journal of Physics Conference Series, Vol. 610, Journal of Physics

Conference Series, 012001

Barausse, E., Bellovary, J., Berti, E., Holley-Bockelmann, K., Farris, B., Sathyaprakash, B., & Sesana, A. 2015b, Journal of Physics Conference Series, 610, 012001

Barausse, E., Cardoso, V., & Pani, P. 2014, Phys. Rev. D, 89, 104059

Barausse, E., Cardoso, V., & Pani, P. 2015c, in Journal of Physics Conference Series, Vol. 610, Journal of Physics Conference Series, 012044

Barnes, J. E. & Hernquist, L. 1992, ARA&A, 30, 705

—. 1996, ApJ, 471, 115

Bartos, I., Kocsis, B., Haiman, Z., & Márka, S. 2017, ApJ, 835, 165

Baruteau, C., Crida, A., Paardekooper, S. J., Masset, F., Guilet, J., Bitsch, B., Nelson, R., Kley, W., & Papaloizou, J. 2014a, in Protostars and Planets VI, ed. H. Beuther, R. S. Klessen, C. P. Dullemond, & T. Henning, 667

Baruteau, C., Crida, A., Paardekooper, S.-J., Masset, F., Guilet, J., Bitsch, B., Nelson, R., Kley, W., & Papaloizou, J. 2014b, Protostars and Planets VI, 667

Baruteau, C. & Masset, F. Recent Developments in Planet Migration Theory, ed. J. Souchay, S. Mathis, & T. Tokieda, Vol. 861, 201

Baruteau, C., Ramirez-Ruiz, E., & Masset, F. 2012, MNRAS, 423, L65

Begelman, M. C. 1979, MNRAS, 187, 237

Begelman, M. C., Blandford, R. D., & Rees, M. J. 1980, Nature, 287, 307

Bellovary, J. M., Mac Low, M.-M., McKernan, B., & Ford, K. E. S. 2016, ApJ, 819, L17

Berti, E., Cardoso, V., Gonzalez, J. A., Sperhake, U., Hannam, M., Husa, S., & Brügmann, B. 2007, Phys. Rev. D, 76, 064034

Bitsch, B., Crida, A., Libert, A.-S., & Lega, E. 2013, A&A, 555, A124

Blaes, O., Krolik, J. H., Hirose, S., & Shabaltas, N. 2011, ApJ, 733, 110

Bode, J., Phinney, E., California Institute of Technology. Division of Physics, M., & Astronomy. 2011, Black Hole Mergers and Their Electromagnetic Counterparts, CIT theses (California Institute of Technology)

Bogdanović, T., Reynolds, C. S., & Miller, M. C. 2007, ApJ, 661, L147

Bonetti, M., Sesana, A., Haardt, F., Barausse, E., & Colpi, M. 2018, arXiv e-prints

Burke-Spolaor, S., Taylor, S. R., Charisi, M., Dolch, T., Hazboun, J. S., Holgado, A. M., Kelley, L. Z., Lazio, T. J. W., Madison, D. R., McMann, N., Mingarelli, C. M. F., Rasskazov, A., Siemens, X., Simon, J. J., & Smith, T. L. 2019, A&A Rev., 27, 5

Cerioli, A., Lodato, G., & Price, D. J. 2016, MNRAS, 457, 939

Chakrabarti, S. K. 1996, Phys. Rev. D, 53, 2901

Chang, P., Strubbe, L. E., Menou, K., & Quataert, E. 2010, MNRAS, 407, 2007

Charisi, M., Bartos, I., Haiman, Z., Price-Whelan, A. M., Graham, M. J., Bellm, E. C., Laher, R. R., & Márka, S. 2016, MNRAS, 463, 2145

Charisi, M., Haiman, Z., Schiminovich, D., & D'Orazio, D. J. 2018, MNRAS, 476, 4617

Colpi, M. & Sesana, A. Gravitational Wave Sources in the Era of Multi-Band Gravitational Wave Astronomy, 43–140

Corrales, L. R., Haiman, Z., & MacFadyen, A. 2010, MNRAS, 404, 947

Coughlin, E. R., Quataert, E., Fernández, R., & Kasen, D. 2018, MNRAS, 477, 1225

Crida, A., Baruteau, C., Kley, W., & Masset, F. 2009, A&A, 502, 679

Crida, A. & Morbidelli, A. 2007, MNRAS, 377, 1324

Cutler, C. & Flanagan, É. E. 1994, Phys. Rev. D, 49, 2658

Cutler, C. & Vallisneri, M. 2007, Phys. Rev. D, 76, 104018

D'Angelo, G., Bate, M. R., & Lubow, S. H. 2005, MNRAS, 358, 316

de Val-Borro, M., Edgar, R. G., Artymowicz, P., Ciecielag, P., Cresswell, P., D'Angelo, G., Delgado-Donate, E. J., Dirksen, G., Fromang, S., Gawryszczak, A., Klahr, H., Kley, W., Lyra, W., Masset, F., Mellema, G., Nelson, R. P., Paardekooper, S.-J., Peplinski, A., Pierens, A., Plewa, T., Rice, K., Schäfer, C., & Speith, R. 2006, MNRAS, 370, 529

Dempsey, A. M., Lee, W.-K., & Lithwick, Y. 2019, arXiv e-prints, arXiv:1908.02326

Derdzinski, A. M., D'Orazio, D., Duffell, P., Haiman, Z., & MacFadyen, A. 2019, MNRAS, 486, 2754

Dittmann, A. J. & Miller, M. C. 2019, arXiv e-prints, arXiv:1911.08685

D'Orazio, D. J., Haiman, Z., Duffell, P., MacFadyen, A., & Farris, B. 2016, MNRAS, 459,

2379

D'Orazio, D. J., Haiman, Z., & MacFadyen, A. 2013, MNRAS, 436, 2997

D'Orazio, D. J., Haiman, Z., & Schiminovich, D. 2015, Nature, 525, 351

D'Orazio, D. J. & Loeb, A. 2018a, ApJ, 863, 185

—. 2018b, Phys. Rev. D, 97, 083008

Dotti, M., Colpi, M., Haardt, F., & Mayer, L. 2007, MNRAS, 379, 956

Dotti, M., Sesana, A., & Decarli, R. 2012, Advances in Astronomy, 2012, 940568

Duffell, P. C. 2015a, ApJ, 807, L11

—. 2015b, ApJ, 806, 182

—. 2016, ApJS, 226, 2

Duffell, P. C., D'Orazio, D., Derdzinski, A., Haiman, Z., MacFadyen, A., Rosen, A. L., & Zrake, J. 2019a, arXiv e-prints, arXiv:1911.05506

—. 2019b, arXiv e-prints, arXiv:1911.05506

Duffell, P. C., Haiman, Z., MacFadyen, A. I., D'Orazio, D. J., & Farris, B. D. 2014, ApJ, 792, L10

Dunhill, A. C., Alexander, R. D., & Armitage, P. J. 2013, MNRAS, 428, 3072

Dürmann, C. & Kley, W. 2017, A&A, 598, A80

Edgar, R. 2004, New A Rev., 48, 843

Edgar, R. G. 2007, ApJ, 663, 1325

Event Horizon Telescope Collaboration, Akiyama, K., Alberdi, A., Alef, W., Asada, K., Azulay, R., Baczko, A.-K., Ball, D., Baloković, M., Barrett, J., Bintley, D., Blackburn, L., Boland, W., Bouman, K. L., Bower, G. C., Bremer, M., Brinkerink, C. D., Brissenden, R., Britzen, S., Broderick, A. E., Broguiere, D., Bronzwaer, T., Byun, D.-Y., Carlstrom, J. E., Chael, A., Chan, C.-k., Chatterjee, S., Chatterjee, K., Chen, M.-T., Chen, Y., Cho, I., Christian, P., Conway, J. E., Cordes, J. M., Crew, G. B., Cui, Y., Davelaar, J., De Laurentis, M., Deane, R., Dempsey, J., Desvignes, G., Dexter, J., Doeleman, S. S., Eatough, R. P., Falcke, H., Fish, V. L., Fomalont, E., Fraga-Encinas, R., Freeman, W. T., Friberg, P., Fromm, C. M., Gómez, J. L., Galison, P., Gammie, C. F., García, R., Gentaz, O., Georgiev, B., Goddi, C., Gold, R., Gu, M., Gurwell, M., Hada, K., Hecht,

M. H., Hesper, R., Ho, L. C., Ho, P., Honma, M., Huang, C.-W. L., Huang, L., Hughes, D. H., Ikeda, S., Inoue, M., Issaoun, S., James, D. J., Jannuzi, B. T., Janssen, M., Jeter, B., Jiang, W., Johnson, M. D., Jorstad, S., Jung, T., Karami, M., Karuppusamy, R., Kawashima, T., Keating, G. K., Kettenis, M., Kim, J.-Y., Kim, J., Kim, J., Kino, M., Koay, J. Y., Koch, P. M., Koyama, S., Kramer, M., Kramer, C., Krichbaum, T. P., Kuo, C.-Y., Lauer, T. R., Lee, S.-S., Li, Y.-R., Li, Z., Lindqvist, M., Liu, K., Liuzzo, E., Lo, W.-P., Lobanov, A. P., Loinard, L., Lonsdale, C., Lu, R.-S., MacDonald, N. R., Mao, J., Markoff, S., Marrone, D. P., Marscher, A. P., Martí-Vidal, I., Matsushita, S., Matthews, L. D., Medeiros, L., Menten, K. M., Mizuno, Y., Mizuno, I., Moran, J. M., Moriyama, K., Moscibrodzka, M., Müller, C., Nagai, H., Nagar, N. M., Nakamura, M., Narayan, R., Narayanan, G., Natarajan, I., Neri, R., Ni, C., Noutsos, A., Okino, H., Olivares, H., Ortiz-León, G. N., Oyama, T., Özel, F., Palumbo, D. C. M., Patel, N., Pen, U.-L., Pesce, D. W., Piétu, V., Plambeck, R., PopStefanija, A., Porth, O., Prather, B., Preciado-López, J. A., Psaltis, D., Pu, H.-Y., Ramakrishnan, V., Rao, R., Rawlings, M. G., Raymond, A. W., Rezzolla, L., Ripperda, B., Roelofs, F., Rogers, A., Ros, E., Rose, M., Roshanineshat, A., Rottmann, H., Roy, A. L., Ruszczyk, C., Ryan, B. R., Rygl, K. L. J., Sánchez, S., Sánchez-Arguelles, D., Sasada, M., Savolainen, T., Schloerb, F. P., Schuster, K.-F., Shao, L., Shen, Z., Small, D., Sohn, B. W., SooHoo, J., Tazaki, F., Tiede, P., Tilanus, R. P. J., Titus, M., Toma, K., Torne, P., Trent, T., Trippe, S., Tsuda, S., van Bemmel, I., van Langevelde, H. J., van Rossum, D. R., Wagner, J., Wardle, J., Weintroub, J., Wex, N., Wharton, R., Wielgus, M., Wong, G. N., Wu, Q., Young, K., Young, A., Younsi, Z., Yuan, F., Yuan, Y.-F., Zensus, J. A., Zhao, G., Zhao, S.-S., Zhu, Z., Algaba, J.-C., Allardi, A., Amestica, R., Anczarski, J., Bach, U., Baganoff, F. K., Beaudoin, C., Benson, B. A., Berthold, R., Blanchard, J. M., Blundell, R., Bustamente, S., Cappallo, R., Castillo-Domínguez, E., Chang, C.-C., Chang, S.-H., Chang, S.-C., Chen, C.-C., Chilson, R., Chuter, T. C., Córdova Rosado, R., Coulson, I. M., Crawford, T. M., Crowley, J., David, J., Derome, M., Dexter, M., Dornbusch, S., Dudevoir, K. A., Dzib, S. A., Eckart, A., Eckert, C., Erickson, N. R., Everett, W. B., Faber, A., Farah, J. R., Fath, V., Folkers, T. W., Forbes, D. C., Freund, R., Gómez-Ruiz, A. I., Gale, D. M., Gao, F., Geertsema, G., Graham, D. A., Greer, C. H., Grosslein, R., Gueth, F., Haggard, D., Halverson, N. W., Han, C.-C., Han, K.-C., Hao, J., Hasegawa, Y., Henning, J. W., Hernández-Gómez, A., Herrero-Illana, R., Heyminck, S., Hirota, A., Hoge, J., Huang, Y.-D., Impellizzeri, C. M. V., Jiang, H., Kamble, A., Keisler, R., Kimura, K., Kono, Y., Kubo, D., Kuroda, J., Lacasse, R., Laing, R. A., Leitch, E. M., Li, C.-T., Lin, L. C. C., Liu, C.-T., Liu, K.-Y., Lu, L.-M., Marson, R. G., Martin-Cocher, P. L., Massingill, K. D., Matulonis, C., McColl, M. P., McWhirter, S. R., Messias, H., Meyer-Zhao, Z., Michalik, D., Montaña, A., Montgomerie, W., Mora-Klein, M., Muders, D., Nadolski, A., Navarro, S., Neilsen, J., Nguyen, C. H., Nishioka, H., Norton, T., Nowak, M. A., Nystrom, G., Ogawa, H., Oshiro, P., Oyama, T., Parsons, H., Paine, S. N., Peñalver, J., Phillips, N. M., Poirier, M., Pradel, N., Primiani, R. A., Raffin, P. A., Rahlin, A. S., Reiland, G., Risacher, C., Ruiz, I., Sáez-Madaín, A. F., Sassella, R., Schellart, P., Shaw, P., Silva, K. M., Shiokawa, H., Smith, D. R., Snow, W., Souccar, K.,

Sousa, D., Sridharan, T. K., Srinivasan, R., Stahm, W., Stark, A. A., Story, K., Timmer, S. T., Vertatschitsch, L., Walther, C., Wei, T.-S., Whitehorn, N., Whitney, A. R., Woody, D. P., Wouterloot, J. G. A., Wright, M., Yamaguchi, P., Yu, C.-Y., Zeballos, M., Zhang, S., & Ziurys, L. 2019, ApJ, 875, L1

Fabian, A. C. 2012, ARA&A, 50, 455

Farris, B. D., Duffell, P., MacFadyen, A. I., & Haiman, Z. 2014, ApJ, 783, 134

—. 2015a, MNRAS, 447, L80

—. 2015b, MNRAS, 446, L36

Ferrarese, L. & Ford, H. 2005, Space Sci. Rev., 116, 523

Fontecilla, C., Chen, X., & Cuadra, J. 2017, MNRAS, 468, L50

Frank, J., King, A., & Raine, D. J. 2002, Accretion Power in Astrophysics: Third Edition

Fryxell, B., Olson, K., Ricker, P., Timmes, F. X., Zingale, M., Lamb, D. Q., MacNeice, P., Rosner, R., Truran, J. W., & Tufo, H. 2000, ApJS, 131, 273

Fu, H., Wrobel, J. M., Myers, A. D., Djorgovski, S. G., & Yan, L. 2015, ApJ, 815, L6

Genzel, R., Eisenhauer, F., & Gillessen, S. 2010, Reviews of Modern Physics, 82, 3121

Ghez, A. M., Klein, B. L., Morris, M., & Becklin, E. E. 1998, ApJ, 509, 678

Giustini, M. & Proga, D. 2019, A&A, 630, A94

Goicovic, F. G., Cuadra, J., Sesana, A., Stasyszyn, F., Amaro-Seoane, P., & Tanaka, T. L. 2015, ArXiv e-prints

Goldreich, P. & Tremaine, S. 1980, ApJ, 241, 425

González, J. A., Hannam, M., Sperhake, U., Brügmann, B., & Husa, S. 2007, Physical Review Letters, 98, 231101

Goodman, J. & Tan, J. C. 2004, ApJ, 608, 108

Goulding, A. D., Greene, J. E., Bezanson, R., Greco, J., Johnson, S., Leauthaud, A., Matsuoka, Y., Medezinski, E., & Price-Whelan, A. M. 2018, PASJ, 70, S37

Graham, M. J., Djorgovski, S. G., Stern, D., Drake, A. J., Mahabal, A. A., Donalek, C., Glikman, E., Larsen, S., & Christensen, E. 2015, ArXiv e-prints

Greene, J. E., Strader, J., & Ho, L. C. 2019, arXiv e-prints, arXiv:1911.09678

Gruzinov, A., Levin, Y., & Matzner, C. D. 2020, MNRAS, 492, 2755

Gültekin, K. & Miller, J. M. 2012, ApJ, 761, 90

Haiman, Z. 2017, Phys. Rev. D, 96, 023004

Haiman, Z., Kocsis, B., & Menou, K. 2009, ApJ, 700, 1952

Hayasaki, K., Mineshige, S., & Sudou, H. Astronomical Society of the Pacific Conference Series, Vol. 373, SPH Simulations of Accretion Flows onto Supermassive Binary Black Holes from Circumbinary Disks, ed. L. C. Ho & J. W. Wang, 59

Hazboun, J. S., Simon, J., Taylor, S. R., Lam, M. T., Vigeland, S. J., Islo, K., Key, J. S., Arzoumanian, Z., Baker, P. T., Brazier, A., Brook, P. R., Burke-Spolaor, S., Chatterjee, S., Cordes, J. M., Cornish, N. J., Crawford, F., Crowter, K., Cromartie, H. T., DeCesar, M., Demorest, P. B., Dolch, T., Ellis, J. A., Ferdman, R. D., Ferrara, E., Fonseca, E., Garver-Daniels, N., Gentile, P., Good, D., Holgado, A. M., Huerta, E. A., Jennings, R., Jones, G., Jones, M. L., Kaiser, A. R., Kaplan, D. L., Kelley, L. Z., Lazio, T. J. W., Levin, L., Lommen, A. N., Lorimer, D. R., Luo, J., Lynch, R. S., Madison, D. R., McLaughlin, M. A., McWilliams, S. T., Mingarelli, C. M. F., Ng, C., Nice, D. J., Pennucci, T. T., Pol, N. S., Ransom, S. M., Ray, P. S., Siemens, X., Spiewak, R., Stairs, I. H., Stinebring, D. R., Stovall, K., Swiggum, J., Turner, J. E., Vallisneri, M., van Haasteren, R., Witt, C. A., & Zhu, W. W. 2019, arXiv e-prints, arXiv:1909.08644

Hellings, R. W. & Downs, G. S. 1983, ApJ, 265, L39

Hernquist, L. 1989, Nature, 340, 687

Herrmann, F., Hinder, I., Shoemaker, D. M., Laguna, P., & Matzner, R. A. 2007, Phys. Rev. D, 76, 084032

Hopkins, P. F., Hernquist, L., Cox, T. J., & Kereš, D. 2008, ApJS, 175, 356

Hu, B. X., D'Orazio, D. J., Haiman, Z., Smith, K. L., Snios, B., Charisi, M., & Di Stefano, R. 2019, arXiv e-prints, arXiv:1910.05348

Inayoshi, K., Haiman, Z., & Ostriker, J. P. 2016, MNRAS, 459, 3738

Inayoshi, K., Visbal, E., & Haiman, Z. 2019, arXiv e-prints, arXiv:1911.05791

Ivanov, P. B., Papaloizou, J. C. B., & Polnarev, A. G. 1999, MNRAS, 307, 79

Janiuk, A., Bejger, M., Charzyński, S., & Sukova, P. 2017, New A, 51, 7

Jiang, Y.-F., Blaes, O., Stone, J. M., & Davis, S. W. 2019, ApJ, 885, 144

Jiang, Y.-F., Stone, J. M., & Davis, S. W. 2013, ApJ, 778, 65

—. 2014, ApJ, 796, 106

Kanagawa, K. D., Tanaka, H., & Szuszkiewicz, E. 2018, ApJ, 861, 140

Kauffmann, G. & Haehnelt, M. 2000, MNRAS, 311, 576

Kazantzidis, S., Mayer, L., Colpi, M., Madau, P., Debattista, V. P., Wadsley, J., Stadel, J., Quinn, T., & Moore, B. 2005, ApJ, 623, L67

Kelley, L. Z., Blecha, L., Hernquist, L., & Sesana, A. 2017, ArXiv e-prints

Kelley, L. Z., Blecha, L., Hernquist, L., Sesana, A., & Taylor, S. R. 2018, MNRAS, 477, 964

Kelley, L. Z., Haiman, Z., Sesana, A., & Hernquist, L. 2019, MNRAS, 485, 1579

Kennedy, G. F., Meiron, Y., Shukirgaliyev, B., Panamarev, T., Berczik, P., Just, A., & Spurzem, R. 2016, MNRAS, 460, 240

King, A. R., Pringle, J. E., & Livio, M. 2007, MNRAS, 376, 1740

Klein, A., Barausse, E., Sesana, A., Petiteau, A., Berti, E., Babak, S., Gair, J., Aoudia, S., Hinder, I., Ohme, F., & Wardell, B. 2016, Phys. Rev. D, 93, 024003

Kocsis, B., Haiman, Z., Menou, K., & Frei, Z. 2007, Phys. Rev. D, 76, 022003

Kocsis, B. & Sesana, A. 2011, MNRAS, 411, 1467

Kocsis, B., Yunes, N., & Loeb, A. 2011, Phys. Rev. D, 84, 024032

Komossa, S. 2003, in American Institute of Physics Conference Series, Vol. 686, The Astrophysics of Gravitational Wave Sources, ed. J. M. Centrella, 161–174

Koratkar, A. & Blaes, O. 1999, PASP, 111, 1

Kormendy, J. & Ho, L. C. 2013, ARA&A, 51, 511

Kormendy, J. & Richstone, D. 1995, ARA&A, 33, 581

Krolik, J. H. 2010, ApJ, 709, 774

Lang, R. N. & Hughes, S. A. 2008, ApJ, 677, 1184

Lau, M. Y. M., Mandel, I., Vigna-Gómez, A., Neijssel, C. J., Stevenson, S., & Sesana, A. 2019, arXiv e-prints, arXiv:1910.12422

Lee, D. 2013, Journal of Computational Physics, 243, 269

Levin, Y. 2007, MNRAS, 374, 515

Lin, D. N. C. & Pringle, J. E. 1987, MNRAS, 225, 607

Lippai, Z., Frei, Z., & Haiman, Z. 2008, ApJ, 676, L5

Liu, T., Gezari, S., Ayers, M., Burgett, W., Chambers, K., Hodapp, K., Huber, M. E., Kudritzki, R. P., Metcalfe, N., Tonry, J., Wainscoat, R., & Waters, C. 2019, ApJ, 884, 36

Liu, X., Shen, Y., & Strauss, M. A. 2012, ApJ, 745, 94

Lubow, S. H., Seibert, M., & Artymowicz, P. 1999, ApJ, 526, 1001

Lynden-Bell, D. 1969, Nature, 223, 690

—. 1978, Phys. Scr, 17, 185

MacFadyen, A. I. & Milosavljević, M. 2008, ApJ, 672, 83

Malkan, M. A. 1983, ApJ, 268, 582

Mandel, I. & Gair, J. R. 2009a, Classical and Quantum Gravity, 26, 094036

—. 2009b, Classical and Quantum Gravity, 26, 094036

Masset, F. S. 2002, A&A, 387, 605

Mayer, L. 2013, Classical and Quantum Gravity, 30, 244008

—. 2017, ArXiv e-prints

Mayer, L., Kazantzidis, S., Madau, P., Colpi, M., Quinn, T., & Wadsley, J. 2007, in Relativistic Astrophysics Legacy and Cosmology - Einstein's Legacy, ed. B. Aschenbach, V. Burwitz, G. Hasinger, & B. Leibundgut, 152

McKernan, B., Ford, K. E. S., Bellovary, J., Leigh, N. W. C., Haiman, Z., Kocsis, B., Lyra, W., MacLow, M.-M., Metzger, B., O'Dowd, M., Endlich, S., & Rosen, D. J. 2017, ArXiv e-prints

McKernan, B., Ford, K. E. S., Kocsis, B., Lyra, W., & Winter, L. M. 2014, MNRAS, 441, 900

McKernan, B., Ford, K. E. S., Lyra, W., & Perets, H. B. 2012, MNRAS, 425, 460

Megevand, M., Anderson, M., Frank, J., Hirschmann, E. W., Lehner, L., Liebling, S. L., Motl, P. M., & Neilsen, D. 2009, Phys. Rev. D, 80, 024012

Miller, M. C. 2009, Classical and Quantum Gravity, 26, 094031

Mingarelli, C. M. F. 2019, Nature Astronomy, 3, 8

Mingarelli, C. M. F., Lazio, T. J. W., Sesana, A., Greene, J. E., Ellis, J. A., Ma, C.-P., Croft, S., Burke-Spolaor, S., & Taylor, S. R. 2017, Nature Astronomy, 1, 886

Mo, H., van den Bosch, F. C., & White, S. 2010, Galaxy Formation and Evolution

Moody, M. S. L., Shi, J.-M., & Stone, J. M. 2019, ApJ, 875, 66

Muñoz, D. J., Miranda, R., & Lai, D. 2018, arXiv e-prints

Müller, T. W. A., Kley, W., & Meru, F. 2012, A&A, 541, A123

Murray, C. D. & Dermott, S. F. 2000, Solar System Dynamics

Narayan, R. 2000, ApJ, 536, 663

Narayan, R. & Yi, I. 1994, ApJ, 428, L13

Nelemans, G., Yungelson, L. R., & Portegies Zwart, S. F. 2001, A&A, 375, 890

Novikov, I. D. & Thorne, K. S. 1973, in Black Holes (Les Astres Occlus), 343–450

O'Neill, S. M., Miller, M. C., Bogdanović, T., Reynolds, C. S., & Schnittman, J. D. 2009, ApJ, 700, 859

Paardekooper, S.-J. & Mellema, G. 2006, A&A, 459, L17

Papaloizou, J. C. B., Nelson, R. P., & Masset, F. 2001, A&A, 366, 263

Penoyre, Z. & Haiman, Z. 2018, MNRAS, 473, 498

Perna, R., Lazzati, D., & Giacomazzo, B. 2016, ApJ, 821, L18

Peters, P. C. 1964, Phys. Rev., 136, B1224

Ragusa, E., Rosotti, G., Teyssandier, J., Booth, R., Clarke, C. J., & Lodato, G. 2018, MNRAS, 474, 4460

Rees, M. J. 1984, in X-ray and UV Emission from Active Galactic Nuclei, ed. W. Brinkmann & J. Truemper, 138–151

Robert, C. M. T., Crida, A., Lega, E., Méheut, H., & Morbidelli, A. 2018, ArXiv e-prints

Robson, T., Cornish, N. J., & Liu, C. 2019, Classical and Quantum Gravity, 36, 105011

Rodriguez, C., Taylor, G. B., Zavala, R. T., Peck, A. B., Pollack, L. K., & Romani, R. W. 2006, ApJ, 646, 49

Rosado, P. A., Sesana, A., & Gair, J. 2015, MNRAS, 451, 2417

Rosotti, G. P., Lodato, G., & Price, D. J. 2012, MNRAS, 425, 1958

Rossi, E. M., Lodato, G., Armitage, P. J., Pringle, J. E., & King, A. R. 2010, MNRAS, 401, 2021

Ryu, T., Perna, R., Haiman, Z., Ostriker, J. P., & Stone, N. C. 2018, MNRAS, 473, 3410

Salpeter, E. E. 1964, ApJ, 140, 796

Sampson, L., Cornish, N. J., & McWilliams, S. T. 2015, Phys. Rev. D, 91, 084055

Schmidt, M. 1963, Nature, 197, 1040

Schnittman, J. D. & Krolik, J. H. 2008, ApJ, 684, 835

Sesana, A., Haardt, F., Madau, P., & Volonteri, M. 2005, ApJ, 623, 23

Sesana, A., Haiman, Z., Kocsis, B., & Kelley, L. Z. 2017, ArXiv e-prints

Sesana, A., Roedig, C., Reynolds, M. T., & Dotti, M. 2012, MNRAS, 420, 860

Shakura, N. I. & Sunyaev, R. A. 1973, A&A, 24, 337

—. 1976, MNRAS, 175, 613

Shang, Z., Brotherton, M. S., Green, R. F., Kriss, G. A., Scott, J., Quijano, J. K., Blaes, O., Hubeny, I., Hutchings, J., Kaiser, M. E., Koratkar, A., Oegerle, W., & Zheng, W. 2005, ApJ, 619, 41

Shannon, R. M., Ravi, V., Lentati, L. T., Lasky, P. D., Hobbs, G., Kerr, M., Manchester, R. N., Coles, W. A., Levin, Y., Bailes, M., Bhat, N. D. R., Burke-Spolaor, S., Dai, S., Keith, M. J., Osłowski, S., Reardon, D. J., van Straten, W., Toomey, L., Wang, J.-B., Wen, L., Wyithe, J. S. B., & Zhu, X.-J. 2015, ArXiv e-prints

Shi, J.-M., Krolik, J. H., Lubow, S. H., & Hawley, J. F. 2012, ApJ, 749, 118

Shu, F. H. 1992, Physics of Astrophysics, Vol. II

Slone, O. & Netzer, H. 2012, MNRAS, 426, 656

Slutsky, J. & LISA Pathfinder Collaboration. 2018, in American Astronomical Society Meeting Abstracts, Vol. 231, American Astronomical Society Meeting Abstracts #231, 355.23

Soltan, A. 1982, MNRAS, 200, 115

Springel, V. 2010, ARA&A, 48, 391

Stern, D., McKernan, B., Graham, M. J., Ford, K. E. S., Ross, N. P., Meisner, A. M., Assef, R. J., Baloković, M., Brightman, M., Dey, A., Drake, A., Djorgovski, S. G., Eisenhardt, P., & Jun, H. D. 2018, ApJ, 864, 27

Stone, N. C., Metzger, B. D., & Haiman, Z. 2017, MNRAS, 464, 946

Syer, D. & Clarke, C. J. 1995, MNRAS, 277, 758

Tamanini, N. 2016, ArXiv e-prints

Tanaka, H., Takeuchi, T., & Ward, W. R. 2002, ApJ, 565, 1257

Tanaka, T., Menou, K., & Haiman, Z. 2012, MNRAS, 420, 705

Tang, Y., Haiman, Z., & MacFadyen, A. 2018, MNRAS, 476, 2249

Tang, Y., MacFadyen, A., & Haiman, Z. 2017, MNRAS, 469, 4258

Taniguchi, Y. & Wada, K. 1996, ApJ, 469, 581

Taylor, S. R., Huerta, E. A., Gair, J. R., & McWilliams, S. T. 2016, ApJ, 817, 70

Tazzari, M. & Lodato, G. 2015, MNRAS, 449, 1118

Teyssandier, J. & Ogilvie, G. I. 2017, MNRAS, 467, 4577

Vasiliev, E., Antonini, F., & Merritt, D. 2015, ApJ, 810, 49

Verbiest, J. P. W., Lentati, L., Hobbs, G., van Haasteren, R., Demorest, P. B., Janssen, G. H., Wang, J. B., Desvignes, G., Caballero, R. N., Keith, M. J., Champion, D. J., Arzoumanian, Z., Babak, S., Bassa, C. G., Bhat, N. D. R., Brazier, A., Brem, P., Burgay, M., Burke-Spolaor, S., Chamberlin, S. J., Chatterjee, S., Christy, B., Cognard, I., Cordes, J. M., Dai, S., Dolch, T., Ellis, J. A., Ferdman, R. D., Fonseca, E., Gair, J. R., Garver-Daniels, N. E., Gentile, P., Gonzalez, M. E., Graikou, E., Guillemot, L., Hessels, J. W. T., Jones, G., Karuppusamy, R., Kerr, M., Kramer, M., Lam, M. T., Lasky, P. D., Lassus, A., Lazarus, P., Lazio, T. J. W., Lee, K. J., Levin, L., Liu, K., Lynch, R. S., Lyne, A. G., Mckee, J., McLaughlin, M. A., McWilliams, S. T., Madison, D. R., Manchester, R. N., Mingarelli, C. M. F., Nice, D. J., Osłowski, S., Palliyaguru, N. T., Pennucci, T. T., Perera, B. B. P., Perrodin, D., Possenti, A., Petiteau, A., Ransom, S. M., Reardon, D., Rosado, P. A., Sanidas, S. A., Sesana, A., Shaifullah, G., Shannon, R. M., Siemens, X., Simon, J., Smits, R., Spiewak, R., Stairs, I. H., Stappers, B. W., Stinebring, D. R., Stovall, K., Swiggum, J. K., Taylor, S. R., Theureau, G., Tiburzi, C., Toomey, L., Vallisneri, M., van

Straten, W., Vecchio, A., Wang, Y., Wen, L., You, X. P., Zhu, W. W., & Zhu, X. J. 2016, MNRAS, 458, 1267

Volonteri, M., Haardt, F., & Madau, P. 2003, ApJ, 582, 559

Ward, W. R. 1997, Icarus, 126, 261

Will, C. M. & Yunes, N. 2004, Classical and Quantum Gravity, 21, 4367

Yi, S.-X., Cheng, K. S., & Taam, R. E. 2018, The Astrophysical Journal Letters, 859, L25

Yu, Q. & Tremaine, S. 2002, MNRAS, 335, 965

Yunes, N. 2009, GW Notes, 2, 3

Yunes, N., Kocsis, B., Loeb, A., & Haiman, Z. 2011, Physical Review Letters, 107, 171103

Zanotti, O., Rezzolla, L., Del Zanna, L., & Palenzuela, C. 2010, A&A, 523, A8

Zwick, L., Capelo, P. R., Bortolas, E., Mayer, L., & Amaro-Seoane, P. 2019, arXiv e-prints, arXiv:1911.06024